

**Characterising the non-ideal behaviour of a Carbopol gel  
flowing in thin conduits**

by

Masoud Daneshi

M.Sc. Isfahan University of Technology, 2011

A THESIS SUBMITTED IN PARTIAL FULFILLMENT  
OF THE REQUIREMENTS FOR THE DEGREE OF

**Doctor of Philosophy**

in

THE FACULTY OF GRADUATE AND POSTDOCTORAL  
STUDIES

(Chemical and Biological Engineering)

The University of British Columbia  
(Vancouver)

February 2020

© Masoud Daneshi, 2020

The following individuals certify that they have read, and recommend to the Faculty of Graduate and Postdoctoral Studies for acceptance, the dissertation entitled:

Characterising the non-ideal behaviour of a Carbopol gel flowing in thin conduits.

submitted by Masoud Daneshi in partial fulfillment of the requirements

for the degree of Doctor of Philosophy

in Chemical and Biological Engineering

**Examining Committee:**

D. Mark Martinez, Chemical and Biological Engineering  
Supervisor

Neil J. Balmforth, Mathematics  
Supervisory Committee Member

John Grace, Chemical and Biological Engineering  
University Examiner

Gregory A. Lawrence, Civil Engineering  
University Examiner

**Additional Supervisory Committee Members:**

Robert J. Poole, Engineering, University of Liverpool  
External Examiner

Savvas Hatzikiriakos, Chemical and Biological Engineering  
Supervisory Committee Member

Boris Stoeber, Mechanical Engineering & Electrical and Computer Engineering  
Supervisory Committee Member

# Abstract

This thesis examines three problems related to the slow flow of a viscoplastic fluid in a thin conduit in order to characterise unique effects of its complex rheology. The methodology is experimental and we use Carbopol exclusively as a model yield stress fluid. The first part of this thesis is dedicated to exploring the flow behaviour near obstructions in a thin slot. We find that the fore-aft symmetry which is expected theoretically to be broken. The asymmetry is robust, as demonstrated by varying the shape and number of the obstacles, the surfaces of the cell walls, and the steadiness of the flow rate. The results suggest that a rheological hysteresis near the yield point may be the cause of the asymmetry. The second part of this thesis demonstrates wall-slip behaviour in a fully developed Poiseuille flow. The simultaneous velocity and in-situ viscometry measurements are exploited to determine the kinematics and dynamics of the flow in a glass capillary. The slip velocity is related to the wall-shear stress, using a power-law scaling, with an exponent independent of the microstructure of the fluid and viscosity of the solvent. The third part of this thesis is dedicated to investigating the multi-layered flow of miscible liquids in a thin, horizontal channel with chemical reaction at the interface. The fluid layers are vertically stratified in the thickness direction and chemical reaction leads to gelation at the interface. A systematic study is performed to examine the hydrodynamic stability of the flow as well as the growth rate of the gel. Our observations suggest that the stability of flow configuration is sensitive to the slight inclination angle in case of fully-reacted flow, and confirm that the gel layer grows diffusively along the length of the cell.

# Lay Summary

A large number of fluids in industrial and geophysical settings, such as cement, crude oil, mud, lava, behave like a viscoplastic fluid. The archetypal characteristic of this material is its yield stress: the material flows only if a stress greater than the yield stress is applied, otherwise, it behaves like a solid. Besides, the practical yield stress fluids exhibit time-dependent behaviour and slip on the smooth surfaces. These features of viscoplastic fluids complicate their flows in confined geometries. This type of flows is ubiquitous in many natural phenomena and industrial processes, ranging from landslides to flow of proppant slurries in rock fractures. In this thesis, we consider three idealized problems concerning the flow of viscoplastic fluids in a thin duct/capillary in order to provide more insight to understanding the flow characters and the effect of complex behaviour of the fluids on them.



# Preface

The five chapters describing the research in this thesis are the results of the research of the author, Masoud Daneshi, during the course of his PhD studies at UBC, under the supervision of Professor D. Mark Martinez. The following papers have been published and/or are being prepared for journal publication:

- **M. Daneshi**, J. MacKenzie, N. J. Balmforth, D. M. Martinez, D. R. Hewitt, “Obstructed viscoplastic flow in a Hele-Shaw cell.” Accepted for publication in *Phys. Rev. Fluid*, 2019.

The author of this thesis was the principal contributor, who designed and performed the experiments, wrote the image processing codes, and analysed the data. The numerical simulation of the problem was carried out by D. R. Hewitt. D. M. Martinez and N. J. Balmforth supervised the research and were involved in the concept formation, analysis and editing of the paper. A version of this paper is found in Chapter 3.

- **M. Daneshi**, A. Pourzahedi, D. M. Martinez, D. Grecov, “Characterising wall-slip behaviour of Carbopol gels in a fully-developed Poiseuille flow.” *J. Non-Newtonian Fluid Mech.*, 269:65-72, 2019.

The author of this thesis designed the experiments, analysed the data and wrote the manuscript. A. Pourzahedi assisted in development and calibration of the experimental setup and in performing the experiments. D. M. Martinez and D. Grecov supervised the research and were involved in the concept formation, analysis and editing of the paper. A version of this paper is found in Chapter 4.

- T. Treskatis, J. MacKenzie, **M. Daneshi**, A. Wachs, D. M. Martinez, “Creating strong medical-grade hydrogel tubing through large scale 3D extrusion printing.” In preparation, 2019.

This paper is the outcome of a research project about designing the 3D extrusion bio-printers working at different flow ranges and different geometries, namely a core-annular geometry and a Hele-Shaw cell. T. Treskatis carried out the numerical simulations of the problem. J. MacKenzie focused on the experimental study of the flow in core-annular geometry and at relatively high Reynolds number. All the experimental and theoretical results for the Hele-Shaw geometry, low inertia flow, included in this paper are part of the work done by the author of this thesis. The study of the problem from fluid mechanics perspective was supervised by A. Wachs, and D. M. Martinez. The authors of this unpublished paper permitted their research findings to be used in Chapter 5.

- D. R. Hewitt, **M. Daneshi**, N. J. Balmforth, D. M. Martinez, “Obstructed and channelized viscoplastic flow in a Hele-Shaw cell.” *J. Fluid Mech.*, 790:173-204, 2016.

The theoretical modelling and numerical simulation of the problem were carried out by D. R. Hewitt. D. M. Martinez and N. J. Balmforth supervised the research and were involved in the concept formation, analysis and editing of the paper. The research published in this paper is reproduced in Chapter 2 (see Sec. 2.3).

# Table of Contents

<b>Abstract</b> . . . . .	<b>iii</b>
<b>Lay Summary</b> . . . . .	<b>iv</b>
<b>Preface</b> . . . . .	<b>v</b>
<b>Table of Contents</b> . . . . .	<b>vii</b>
<b>List of Tables</b> . . . . .	<b>x</b>
<b>List of Figures</b> . . . . .	<b>xii</b>
<b>Acknowledgments</b> . . . . .	<b>xxvi</b>
<b>Dedication</b> . . . . .	<b>.xxviii</b>
<b>1 Introduction</b> . . . . .	<b>1</b>
<b>2 Background</b> . . . . .	<b>5</b>
2.1 Industrial motivations . . . . .	5
2.2 Yield stress fluids . . . . .	8
2.2.1 Idealized rheological models for viscoplastic fluids . . . . .	8
2.2.2 Rheological characterization of Carbopol gels . . . . .	9
2.2.3 Wall-slip behaviour of Carbopol gels . . . . .	16
2.3 Hele-Shaw flow . . . . .	21
2.4 Summary . . . . .	26

<b>3</b>	<b>Experiments on obstructed viscoplastic flow in a Hele-Shaw cell . .</b>	<b>30</b>
3.1	Introduction . . . . .	30
3.2	Fluids characterisation . . . . .	35
3.3	Experimental method . . . . .	39
3.4	Results . . . . .	43
3.4.1	Plug phenomenology . . . . .	43
3.4.2	Plug lengths . . . . .	48
3.4.3	Constraining the origin of asymmetry . . . . .	53
3.5	Conclusion . . . . .	56
<b>4</b>	<b>Characterising wall-slip behaviour of Carbopol gels in a fully-developed Poiseuille flow . . . . .</b>	<b>60</b>
4.1	Introduction . . . . .	60
4.2	Materials and rheometry . . . . .	64
4.3	Experimental setup . . . . .	65
4.4	Experimental measurements and uncertainties . . . . .	67
4.4.1	Validation of experimental measurements . . . . .	69
4.4.2	Estimation of the slip velocity . . . . .	71
4.5	Results and discussion . . . . .	73
4.5.1	Sliding yield stress . . . . .	73
4.5.2	Wall slip . . . . .	75
4.6	Conclusion . . . . .	79
<b>5</b>	<b>Observation of reacting multi-layer flows in a Hele-Shaw cell . . . .</b>	<b>82</b>
5.1	Introduction . . . . .	82
5.2	Theory . . . . .	87
5.3	Fluid characterisation . . . . .	90
5.4	Experimental details . . . . .	92
5.4.1	Experimental setup . . . . .	92
5.4.2	Experimental conditions . . . . .	93
5.4.3	Measuring the flow interfaces . . . . .	95
5.5	Results . . . . .	96
5.5.1	Flow configuration . . . . .	96

5.5.2	Characterising the reacting front . . . . .	98
5.6	Conclusion . . . . .	102
<b>6</b>	<b>Summary and conclusions . . . . .</b>	<b>104</b>
6.1	Results and contributions . . . . .	105
6.2	Thesis limitations and recommendations for future work . . . . .	107
	<b>Bibliography . . . . .</b>	<b>111</b>
<b>A</b>	<b>Appendix to Chapter 3 . . . . .</b>	<b>122</b>
A.1	Verification of velocity field along the channel . . . . .	122
A.2	Shape of the rigid zones developing around the obstacles . . . . .	124
A.3	Effect of surface properties of the obstacle . . . . .	125
A.4	Obstacles normal to the flow direction . . . . .	127
A.5	Flow of a thixotropic fluid (Laponite) along an obstructed Hele-Shaw cell . . . . .	129
<b>B</b>	<b>Appendix to chapter 4 . . . . .</b>	<b>137</b>
<b>C</b>	<b>Appendix to Chapter 5 . . . . .</b>	<b>140</b>
C.1	Theoretical approach . . . . .	140
C.2	Analytical modelling . . . . .	145
C.3	Methodology to determine the position of reacting front . . . . .	148

# List of Tables

Table 3.1	Herschel-Bulkley fits of the non-Newtonian fluids used in our experiments including Carbopol solutions, and a PEO solution, with ( $R^2 > 0.99$ ). Also listed are shear storage and loss moduli ( $G'$ and $G''$ ) for gently mixed Carbopol solutions. The dynamic measurements taken from small amplitude oscillatory rheometry at a frequency of 1 Hz and a strain amplitude of $\gamma = 1\%$ (below which we confirmed that the two moduli where independent of $\gamma$ ). . . . .	39
Table 4.1	List of Carbopol gels including different parameters used to prepare them and their rheological properties. The HB parameters were obtained from the best Herschel-Bulkley fit of the Carbopol solutions with R-squared better than 0.99. . . . .	66
Table 5.1	Herschel-Bulkley (HB) coefficients for dilute mixtures of alginate or Carbopol ( $c_1$ ) with a reacting agent ( $c_2$ ). Note that the HB parameters were obtained from the best Herschel-Bulkley fit of the Carbopol solutions with R-squared better than 0.95. . . . .	91
Table 5.2	Inlet conditions for the experimental work. The brackets ( $\cdot$ ) represent a range of experiments within the two bounds and all other conditions are fixed values. The stream concentrations ( $c_{1 \rightarrow 4}$ ) are all in $(w/w)\%$ where the stream notations can be found in Fig. 5.1(a). . . . .	94

Table 5.3	Ranges of dimensionless groups in unreactive and fully-reacted experiments. Note that the negligible difference between the density of middle layer (2) and upper layer (1), as well as that between the viscosity of the lower layer (3) and upper layer (1), imply $At_2 \sim 0$ , $\chi_2 \sim 0$ , and $m_3 \sim 1$ . . . . .	94
Table C.1	Summary of the non-dimensional numbers. . . . .	144

# List of Figures

Figure 2.1	Flows of yield stress fluids along thin conduits occur in many geophysical and industrial settings. Two examples, which are related to the oil and gas industry, are presented here: (a) flow of crude oil or hydraulic fracturing fluids along the fractures in the rock formation (during the oil recovery process), and (b) flow of cement or mud along a thin annulus between casing and rock formation (during the cementing process). The images in panel (a) and panel (b) were taken from [27] and [28], respectively. . . . .	6
Figure 2.2	(a) Flow curves for a simple yield stress fluid, a Carbopol solution, measured by a stress controlled ramp-up and ramp-down test with a ramp-rate of 0.05 Pa/s. The red symbols represent the data obtained from tests with rough plates where slip of the gel on the surface is minimized. The red dots and squares denote the data for ramp-up and ramp-down tests, respectively. The light blue line gives the Herschel-Bulkley fit with $\tau_Y = 30$ Pa, $n = 0.34$ , and $K = 19$ Pa $s^n$ . The blue symbols represent the flow-curve obtained from experiments with smooth plates, where the gel slips on the plates. Here, the blue cross and plus symbols show the data measured from ramp-up and ramp-down experiments, respectively. The figure in panel (a) was taken from [29]. (b) Flow curve for a thixotropic yield stress fluid, a bentonite suspension. The data for increasing and decreasing stress ramps are presented by red squares and blue line, respectively. This	



flow curve shows discernible hysteresis above the yielding point, that is absent in the flow-curves shown in panel (a) for a simple yield stress fluid. The figure in panel (b) was taken from [34]. . . . . 11

Figure 2.3 (a) Shear rate versus time measured during creep tests with a Couette geometry. A schematic representation of the creep experiments is shown in the inset of this figure. The tests have been performed for a Carbopol solution and for a number of different shear stresses ranging from  $0.48\tau_Y$  to  $2.5\tau_Y$ . As shown in this figure, for stresses below the yielding point, the shear rate decreases with time by  $t^{-1}$  (see gray dashed line). Near the yielding point, in particular for  $\tau = 1.02\tau_Y$ , a transient solid-like creep behaviour was observed which is followed by an eventual steady flow. Figure in panel (a) is reproduced from [29]. (b) Steady-state flow curve obtained by measuring the steady shear rate from data presented in panel (a) for different shear stresses. Figures in panel (b) was taken from [32]. . . . . 13

Figure 2.4 Dynamic rheological behaviour of a Carbopol solution: (a) Elastic modulus,  $G'$ , and viscous modulus,  $G''$ , versus strain measured during a strain sweep oscillatory test at  $\omega = 1$  rad/s. (b) Variation of elastic and viscous moduli with the frequency in the linear regime. The results were obtained from a frequency sweep test at  $\gamma = 1\%$ . In panel (a) and (b), the circles and triangles represent the elastic modulus and viscous modulus, respectively. (c) A schematic representation of the Kelvin-Voigt model which is associated with the behaviour of the material in the linear regime. Figures in panel (a) and (b) were taken from [40]. . . . . 14

Figure 2.5 Schematic images representing (a) the jammed structure of a suspension of soft particles near the wall, (b) a detailed view of a soft particle sliding on the wall; the particle with the radius of  $R_p$  is squeezed against the wall which leads to the compression distance of  $h_0$  and a creation of contacting facet with radius of

	$r_0$ . The particle slips against the wall with the speed of $U_s$ . This is attributed to the formation of a lubricating layer of solvent with the thickness of $\delta(x,y)$ between the particle and the wall. Reproduced from [16, 48]. . . . .	18
Figure 2.6	Variation of the scaled pressure developing in the lubrication layer, $P = p/p_0$ , and scaled thickness of this layer along the center of the particle, $H = \delta/h_0$ , with the dimensionless horizontal distance from the center of particle, $X = x/r_0$ . Here, $P_0$ represents the characteristic hydrodynamic pressure in the lubricating film, which is obtained from the balance of the viscous and pressure terms in Eq. (2.5), $p_0 = 6\eta_s U_s R_p^{1/2}/h_0^{3/2}$ . Panel (a) presents the results for an elastohydrodynamically lubricated particle squeezed against a weakly attractive surface, and panel (b) shows the hydrodynamically lubricated particle pressed against a repulsive surface. Reproduced from [19]. . .	20
Figure 2.7	A schematic image of the geometry for a yield stress fluid in a Hele-Shaw cell. . . . .	22
Figure 2.8	Streamlines with a contour map of $q$ for the flow of a Bingham fluid around a disk embedded in a Hele-Shaw cell with the depth of $h = 1$ , and for (a) $B = 1.92$ , (b) $B = 60$ , (c) $B = 9600$ . Plug regions are shaded [8]. . . . .	27
Figure 2.9	Flow past periodic arrays of circular contractions (with contraction ratio of 0.1). (a) Streamlines and a contour map of $q$ for contractions arranged perpendicular to the flow and (b) aligned with the flow. For top row, $B = 4.8$ and for lower row, $B = 1228.8$ . Plug regions are shaded [8]. . . . .	28
Figure 3.1	Viscoplastic flow through a Hele-Shaw cell containing an obstacle. The plane of the cell is shown in (a), where the grid represents the mosaic pattern used to create the composite images in Fig. 3.5. A velocity profile for flow down a uniform, unobstructed cell, with a central rigid plug, is shown in (b), while the corresponding profile through the centerline of the	

	obstructed cell ( $y = 0$ ) is shown in (c), with a shaded pseudo-plug that widens to fill the cell and become truly rigid near the obstacle. . . . .	33
Figure 3.2	(a) Rheological curves for the three different Carbopol suspensions used in this work (0.075% (black), 0.06% (blue) and 0.055% (red)), from a shear-stress ramp up and then down in a roughened parallel-plate rheometer. There is no discernible thixotropic behaviour over most of the range of strain rate, and it is only at stresses very close to the yield stress that any rheological hysteresis is visible. (b) Rheological curves for an alternative Carbopol suspension (0.1%, very highly sheared during mixing) from a shear-rate ramp up and then down in a roughened parallel-plate rheometer, showing a very clear thixotropic signature over multiple decades of shear rate. . . . .	38
Figure 3.3	Overview of the experimental setup: (a) Sketch of the experimental setup including a swept-field confocal microscope, a flow cell, and a syringe pump. The path of excitation laser light (green) and that of emitted light from the fluorescent particles (red) are illustrated in this image. (b) Image of the flow cell mounted on the microscope stage. (c) Image of obstacles embedded in the channel. . . . .	41
Figure 3.4	(a) Transverse velocity profiles obtained at the upstream of a Hele-Shaw cell containing an obstacle. The velocity profiles were experimentally measured along $y$ -axis and at $x = -45$ mm (blue) and $x = -35$ mm (red), for 0.06% Carbopol and $B = 3.1$ . Note that the entry of the flow cell is at $x = -52.5$ mm. (b) Experimentally measured velocity profiles for 0.06% Carbopol in a uniform cell with chemically treated plates at the three Bingham numbers (flow rates) indicated (red). The solid black lines show corresponding theoretical predictions given the fluxes and the rheological parameters in Table 3.1. A profile from a cell with untreated plates for $B = 1.2$ (green) is also shown. . . . .	44

- Figure 3.5 PIV images showing speed, normalised by the incident speed  $U_c = Q/WH$ , and streamlines (all flowing left to right) along the mid-plane of the slot around various obstacles. (a) The flow around a disk for a glycerol-water solution (31 wt/wt%) at  $Q = 0.05$  mL/min; dashed lines show the corresponding potential-flow solution. (b) Flow field for a viscoelastic PEO solution (0.75 wt/wt%) with  $Q = 0.16$  mL/min. (c)–(k) Flow fields for a Carbopol solution (0.06 wt/wt%), untreated walls) with  $B = 3.1$  (c,g,h) and  $B = 2.7$  (d,e,f,i,j,k). The upper limit of the colorbar was set at  $X = 2.8$  for (a,b),  $X = 2$  for (j,k), and  $X = 1.6$  for (c–i). (l) An average image near the plug at the front of a disk (0.075% Carbopol solution,  $B = 2.3$ , treated walls). The solid lines indicate the edge of the plug according to edge-detection (green) or a velocity threshold (red); the dashed line shows the estimated plug length  $\ell_p$ . White lines in (c–k) show the yield surfaces detected using a velocity threshold of  $0.0005$  mm/s. . 46
- Figure 3.6 Speed (shading; scaled by the incident speed  $U_c$ ) and representative streamlines (solid black lines) along the midplane of the slot for computations of Herschel-Bulkley fluid around the grey-shaded obstacles, for  $n = \frac{1}{2}$  and  $B = 4$ . The range of the colorbar matches that used in Fig. 3.5(c)–(k). The white lines show yield surfaces, given by the threshold  $U/U_c = 1 \times 10^{-3}$ . 48
- Figure 3.7 (a) Scaled theoretical (top) and experimental (bottom) speeds,  $U/U_c$ , for flow around a disk with  $n = 0.57$  and  $B = 2.3$ , corresponding to panel (l) in Fig. 3.5 (and using the same scheme for the colormap as that figure). In (b), the theoretical (solid lines) and PIV (dots) speeds are plotted along the sections indicated by the vertical dotted lines in (a). . . . . 49
- Figure 3.8 (a) Dimensional plug lengths  $\ell_p$  of the configurations shown in Fig 3.5, with the conventions indicated by the legend. The walls of the cell are treated to remove slip for the isolated disks, but for the squares, stadia and multiple disks, the walls are untreated in view of the potentially destructive method of insertion or rearrangement. (b) Scaled plug lengths  $\ell_p/\ell_c$ , where  $\ell_c$  is chosen as indicated in the

main text for the three groupings of obstacles. The lines show theoretical results for isolated disks, calculated using the numerical method of [8] for the Herschel-Bulkley model with  $n = 0.5$  (black solid) and  $n = 1$  (red dashed). (c) A comparison of the plug size for flow of 0.06% Carbopol around disks with treated and untreated acrylic sheets. In all three panels, we plot  $\ell_p$  as positive for the plugs at the front, and  $\ell_p < 0$  for those at the back. The error bars indicate the standard deviation from three repetitions of each experiment. . . . 50

Figure 3.9 Theoretical predictions of the plug lengths from numerical simulations for the obstacle arrangements indicated by the legends, and following the experimental results in figure 3.8, showing (a)  $\ell_p/R$  and (b)  $\ell_p/\ell_c$ . These computations have  $n = \frac{1}{2}$ ; in (c) data are shown for isolated disks and the three values of  $n$  for the experimental fluids, as well as results for  $n = \frac{1}{2}$  and for a Bingham fluid ( $n = 1$ ) [8], for reference. . . . . 51

Figure 3.10 Plug lengths for two disks aligned with the flow as a function of the centre-to-centre separation  $L$ , for experiments with untreated sheets and numerical computations;  $B = 2.7$  and  $n = 0.57$  (0.06% Carbopol). The images (i)–(iv) below correspond to the separations identified in the main panel, with the symbols corresponding to the plug locations indicated, and show scaled speed maps (with colorbars as in Fig. 3.5, where  $X = 1.6$ ) and streamlines. Given the lack of any apparent trend with  $L$ , the scatter in the experimental data for the leading plug length (filled red circles), with a standard deviation of about 15%, gives a sense of the overall uncertainty in the measurements. . . . . 54

Figure 3.11 Time dependency of the plug size on the front and back of an isolated disk subject to a flowrate  $Q(t)$ . The tests were performed with 0.06% carbopol solution and treated sheets. The solid and dashed horizontal lines represent the average and standard deviation of steady state value reported in Fig 3.8(b). 56

Figure 3.12 Distribution of normalized plug length measured during two

steady tests (blue) and two unsteady tests (red). The inset indicates the diagram of flow rate by time during steady and unsteady tests. The results are reported for the length of plug region developing in the front of an isolated disk subjected to the flow of 0.06% Carbopol solution. The tests were conducted with treated sheets. The black dots and solid horizontal lines represent the average and standard deviation of steady state value for the plug lengths from Fig 3.8(b). Comparison between the results obtained from steady and unsteady tests does not show any signature of shear history dependence of the plug length. . . . . 57

Figure 3.13 Time series of the plug length after a step change in flow rate behind a circular obstruction in the Hele-Shaw cell using the highly-sheared 0.1%-Carbopol (with flow rate  $Q = 0.05$  ml/min after the step change). Thixotropic flow curve of the material is reported in 3.2(b). . . . . 58

Figure 4.1 (a) Schematic diagram of the experimental setup, (b) an image of tracing particles in x-z plane acquired by the OCT. The white lines in this image indicates the wall positions. Note that the position of the particles along z-direction were corrected by considering the effect of refraction on the capillary wall. Considering the linearity of Snell's law, we mapped the measured positions of particles and walls to their true positions, by applying a linear scaling. The scale factor is obtained from the ratio of the measured diameter of capillary tube in the OCT-images and its actual size. (c) The number of velocity vectors,  $N$ , that contribute to each bin across the capillary tube. Here, the z-axis represents the distance from the centerline of the cell, normalized by the diameter of the capillary tube. Note that the velocity data were obtained from applying the PTV to 1000 paired images. Then the PTV data were averaged using a spatial binning size of  $5\mu m$ . . . . . 68

- Figure 4.2 Benchmarking the (a) velocimetric measurements and (b) viscometric measurements with a Newtonian fluid, 31% *wt/wt* glycerol solution. Panel (a) presents the normalized velocity profiles of the solution corresponding to three different average velocities, 0.16 mm/s, 0.8 mm/s, and 1.7 mm/s (blue dots). The red curve represents the theoretical velocity profile. Panel (b) presents the flow curves of the solution obtained from the capillary viscometer (empty symbols), and a rotational rheometer with parallel plates geometry (filled symbols). . . . . 71
- Figure 4.3 Intrinsic response of the gel: capillary flow curve of 0.075% *wt/wt* Carbopol solution (fluid C1) measured during a varied flowrate by time test (see inset). Data obtained for ramp-up and ramp-down tests are presented by black squares, and red squares, respectively. . . . . 72
- Figure 4.4 (a) Normalized velocity profiles for (a) a 31% *wt/wt* glycerol solution, and (b) a Carbopol solution (fluid C7), at  $B = 1.5$  (blue), and  $B = 0.7$  (black); the dashed line represents the fitted line on velocity data corresponding to the region  $50\ \mu\text{m}$  of the wall position. The gray box, and the dashdotted line show the bounds of the wall position and its center, respectively. The complete velocity profiles across the pipe are replotted in the insets of the panels. The red symbols represent the analytical curve calculated by using the rheological parameters of the gel (see Table 4.1). . . . . 74
- Figure 4.5 (a) Wall shear stress versus flow rate for capillary flow of Carbopol gels with concentrations of 0.75% (\*), 0.1% (○), 0.15% (◇), 0.2% (△), 0.25% (◁), 0.3% (□); The data corresponding to the highly sheared 0.1% *wt/wt* Carbopol gel and glycerol solution-based 0.1% *wt/wt* Carbopol gel are indicated by ●, and ●, respectively. In addition, the friction factor versus Reynolds number is illustrated in the inset of panel (a); the solid line in this figure represents the analytical results obtained based on Herschel-Bulkley model and no-slip condition

on the wall. For all the cases except for the highly sheared 0.1% wt/wt Carbopol gel, the linear regime before yielding and non-linear shear thinning regime after yielding is observable. The enlarged linear region for Carbopol solutions are shown in panel (b). (b) Wall shear stress normalized by the yields stress versus the flow rate; the dashed lines represent the fitted lines on the data in the linear region ( $\tau_w < \tau_Y$ ). The inset of panel (b) presents the sliding yield stress normalized by the yield stress with respect to the concentration of the Carbopol gels. To emphasize the effect of viscosity of the solvent, we prepared 0.1% wt/wt Carbopol gel and 0.15% wt/wt Carbopol gel with a different concentration of glycerol, 11% wt/wt, and calculated the sliding yield stress. The corresponding values are shown in the inset of panel (b) with blue symbols. Note that in panel (b), the values of wall shear stress and sliding yield stress obtained for glycerol solution-based Carbopol gels were scaled by the viscosity ratio of the glycerol solution to water, i.e.  $(\tau_w^*, \tau_{SY}^*) = \frac{(\tau_w, \tau_{SY})}{\eta_s/\eta_w}$ . . . . . 76

Figure 4.6 Variation of (a) the slip velocity with the excess shear stress, (b) the thickness of the slip layer with the excess shear stress normalized by the yield stress, (c) the slip velocity normalized by the maximum velocity with the excess shear stress normalized by the yield stress. Note that, in panel (a), the values of slip velocity obtained for glycerol-solution based Carbopol gel (fluid C7) was scaled by the viscosity ratio of water to solvent,  $U_s^* = \frac{U_s}{\eta_w/\eta_s}$ . The values of slip velocity corresponding to fluid C2 and fluid C8 are compared in the inset of the panel (a). The symbols used in this figure are similar to those defined in the caption of Fig. 4.5. The dashed lines in panel (a) and (c) represent the values of slip velocity calculated from Eq. 4.2 for fluid C2 and fluid C3. . . . . 78

Figure 5.1 Overview of the experimental Hele-Shaw cell and variables.



	(a) Schematic of the Hele-Shaw cell at an inclination angle $\theta$ where $Q_1$ , $Q_2$ and $Q_3$ are the flowrates of each fluid stream. Each fluid stream is considered as a dilute solution of four species in water, where $c_i$ represents the concentration of $i$ -species. The third component, $c_3$ , is the product of chemical reaction between the first two components, $c_1$ and $c_2$ . The forth component, $c_4$ , is non-reactive and affects the density of the solution. The thickness of the channel $H = 3$ mm, entrance length $l_f = 20$ mm, entrance height $h_f = 0.75$ mm, reactor length $L = 200$ mm and width $W = 57$ mm. The position of the gel layer is defined as $h_r(x)$ . (b) Experimental measurements of the velocity field for a Newtonian fluid at an average velocity $U_c = 100 \mu\text{m/s}$ with no layering and no reaction, i.e. $c_{1-4} = 0$ . . . . .	84
Figure 5.2	Numerical simulations of the concentration profiles in a layered flow [92]. The concentration profile for the inner layer (1) and outer layer (2) are denoted by black, and grey, respectively. The layers are assumed to be miscible and the fluids are Newtonian with no reaction and no diffusion, and $Re = 3$ , $Pe = \infty$ , and $Q_1/Q_2 = 1$ . The simulations were conducted for various viscosity ratios (a) $\eta_1/\eta_2 = 0.01$ , (b) $\eta_1/\eta_2 = 0.1$ , (c) $\eta_1/\eta_2 = 1$ , (d) $\eta_1/\eta_2 = 10$ , (e) $\eta_1/\eta_2 = 100$ . . . . .	86
Figure 5.3	Flow curves for the alginate and Carbopol solutions listed in Table 5.1. The dashed lines give the Herschel-Bulkley fits in Table 5.1. . . . .	92
Figure 5.4	Representative spatio-temporal diagrams of (a) an unreactive flow ( $Q_2/Q_1 = 1$ , $\chi_3 = 3000$ ), and (b) a reactive flow ( $Q_2/Q_1 = 0.25$ , $c_1 = 0.1\%$ wt/wt $c_2 = 0.25\%$ wt/wt, $\chi_3 = 0$ ). The images highlight the time evolution of the middle layer which was seeded by the tracing beads. Measurements were performed at a fixed position, as a function of time where $t_{max}$ is 15 s in (a) and 45 s in (b). Note that the materials used for the unreactive and reactive cases were explained in Table. 5.2. . . . .	98

Figure 5.5 Representative diagrams of hydrodynamic stability of a fully reacted flow in a Hele-Shaw. (a) A representative stability diagram with complex behaviour. The data were collected with water in the upper layer (1), fully-reacted Carbopol in the middle layer (2), and a water/sugar mixture in the lower layer (3) (see Table 5.2, and Fig. 5.1). Note that  $Q_1 = Q_3$  for all of the cases shown here. Regions *I*, *II* and *III* represent the three possible flow regimes that depend on the inclination angle and the hatched areas denote unstable flow regimes. For cases (i), (ii) and (iii) we display the time evolution of the second layer, measured at a fixed position, as a function of time where  $t_{max}$  is 130 s, 15 s and 25 s, respectively. (b) Representative fully developed velocity profiles for regions *I–III* in (a). Note that the three flow regimes (*I–III*) and corresponding velocity profiles were obtained from a 1-D theoretical prediction, while the unstable regions were found by experimental observations. . . . 99

Figure 5.6 Growth of the gel layer  $h_r(x)$  with reaction in a Hele-Shaw cell: (a) Theoretical values obtained for the ratio of the thickness of the reacted layer over that of initial alginate layer before reaction,  $H_0$ . The results were obtained for  $Da = 1000$ , and  $Pe = 50, 100, 250, 500, 750, 1000$ . (b) Experimental results for the averaged thickness of reacted layer normalized by the thickness of the channel versus the square root of the advective time scale over diffusive time scale. The data reported in panel (b) correspond to  $Re = 0.31$  ( $Q = 0.9$  mL/min), 0.25% wt/wt-alginate, and 0.1% wt/wt-salt solution. Here, the thickness of the separation plate in the cell is presented by  $\star$ . The error in the estimate is coming from the uncertainties involved with the image processing method and was found by varying the correlation coefficient cut-off, defined in Sec. C.3, by 5%. . . . 101

Figure A.1 Transverse velocity profiles measured along the width of the channel at (a)  $x = -45$  mm (7.5 mm from inlet), (b)  $x = -35$

mm, (c) $x = -25$  mm, (d) $x = -15$  mm, (e) $x = -5$  mm, (f) $x = 5$  mm, (g) $x = 15$  mm, (h) $x = 25$  mm, (i) $x = 35$  mm, (j) $x = 45$  mm (7.5 mm from outlet). Note that the velocity measurements were performed in the central horizontal plane of the cell ( $z = 0$ ). 123

- Figure A.2 The normalized square root of the area of the stagnant regions,  $\sqrt{A_p}/R$ , versus the normalized orthogonal plug length,  $\ell_p/R$ . The symbols used in this figure are similar to those defined in the legend of Fig. 3.8. The dashed line represents the equality line. . . . . 125
- Figure A.3 The speed contours of the flow in the upstream of a square shaped obstacle are shown for (a)  $B = 1.07$ , (b)  $B = 6.10$ , (c)  $B = 10.41$ . The results were obtained for the flow of 0.06% Carbopol in a channel with untreated sheets. The obstacle is indicated by a gray box in the images. The scale-bar on the images represent  $0.2R$ . . . . . 126
- Figure A.4 A comparison of the scaled plug length for the flow of 0.06% Carbopol around a disk with a smooth surface (black symbols) and a disk with a rough surface (red symbols). The circles and triangles represent the length of the front plug and the rear plug, respectively. . . . . 128
- Figure A.5 Contours of the velocity magnitude for the flow of 0.06% Carbopol around two disks arranged normal to the flow direction, and positioned at different separation distances : (a)  $L = 2R$ , and (b)  $L = 2.5R$ . The Bingham number is fixed at  $B = 2.7$ . . . 129
- Figure A.6 Ratio of average velocity between obstacles,  $U_m$ , over the average velocity at the upstream of the cell, for different Bingham numbers. The results were obtained for the flow of 0.06% Carbopol around two disks oriented normal to the flow direction and separated by  $L = 2.1R$ . . . . . 130
- Figure A.7 Time dependency of the plug size on the front of an isolated disk subject to the flow of 1.25% Laponite at the constant flow of  $Q = 1$  mL/min followed by a period of 8 min pre-shearing at a high flow rate ( $Q = 10$  mL/min) and a 10 min rest pe-

riod. The varied flow-rate by time test is described in panel (a). The evolution of the plug length by time is shown in panel (b). Here,  $t_{cr1}$  and  $t_{cr2}$  represent the time-span during which the pre-sheared fluid in the channel and the connecting tube are replaced by the fresh fluid, respectively. The average images of the flow in the front of the disk are shown here for three cases (i)–(iii). . . . . 133

Figure A.8 An average image of flow of tracing particles in 1.25% Laponite near the (a) front, and (b) back of a disk. The images were obtained after running the test at a constant flow rate of  $Q = 1$  mL/min for around 35 min. Here the blue line indicates circumference of the obstacle. . . . . 134

Figure A.9 The steady state velocity profiles along a series of lines crossing the static yielding surfaces perpendicularly (see green axis in the inset). The blue symbols and red symbols correspond to a flow of 1.25% Laponite, and a flow of 0.075% Carbopol, respectively. For both cases the flow rate was fixed at  $Q = 1$  mL/min. . . . . 135

Figure A.10 Images of streaklines of the flow of 1.25% Laponite around two obstacles aligned with the flow direction. The images show the flow of tracing particles near (i) the leading edge and, (ii) tailing edge of the upstream obstacle, as well as (iii) the leading edge and (iv) tailing edge of the downstream obstacle. The images were obtained after running the test at  $Q = 1.2$  mL/min for 5 min followed by preshearing at  $Q = 4$  mL/min for 4 min. . . . . 136

Figure B.1 Channelization of the flow of 0.075% Carbopol in an unobstructed Hele-Shaw cell caused by non-uniform treatment of the surface. Panel (a) represents a schematic image of the cell which was made of two acrylic plates separated by a thin gap (1 mm). The gray box represents the area on the plates which was left untreated, and the dashed box represents the observation window. Panel (b) illustrates the con-

tour of velocity magnitude obtained for inlet flow rate of $Q = 0.16$ mL/min. . . . .	139
--	-----

# Acknowledgments

First and foremost, I would like to express my gratitude to my supervisor, Prof. Mark Martinez, for all his help, support and expertise. His kindness, modesty, as well as his valuable scientific skills make working with him an outstanding experience. I would also like to thank Prof. Neil Balmforth for his helpful guidance, valuable support and immense knowledge. Also I am thankful to my previous professors and supervisor at the Isfahan University of Technology, Isfahan, Iran. Besides many technical skills, they taught me valuable skills such as power of critical thinking and how to design a research project. I feel very privileged to have worked with all of them.

I would like to specifically thank Prof. Dana Grecov and Ali Pourzahedi for their help on the second phase of my research. During my PhD, I had a chance to work closely with post-doctoral researchers. In particular, I am grateful to Dr. Duncan Hewitt and Dr. Timm Treskatis for their help and guidance.

During the past few years, I have worked with several undergraduate and visiting interns, Yufang Soong, Patrick Warren, Jamie Olson, and Dr. Jakob Redlinger-Pohn. I would like to express my sincere gratitude to all of them for their help and contribution to the laboratory experiments. Accomplishing this project was not possible without the disciplined work and great assistance of Yufang Soong. I wish to express my thanks to the staff and students at Pulp and Paper Centre (PPC) for their support throughout this process. Specifically, I would like to thank George Soong, Safety and Operations Officer of PPC, for his unfailing support and loyalty to me and other students. I also want to extend my gratitude to my friends and lab-

mates, in particular Nicholas McIntosh, and Mohammad Shanbghazani, for their cheerful company during my PhD.

Last but not the least, I want to express my special thanks to my family and my wife, Marjan, who supported me at every step of this endeavour.

# Dedication

To my family



# Chapter 1

## Introduction

Slow flow of viscoplastic fluids along slender conduits are found in a large number of industrial and geophysical settings, ranging from oil recovery to the flow of mud volcanos. The rheological behaviour of viscoplastic fluids along with their interaction with the solid surfaces complicate their flow in thin conduits. The key feature of a viscoplastic fluid is its yield stress: the material flows only if the imposed stress exceeds the yield stress. From both a physical and mathematical perspective, the yielding threshold significantly influences the flow in the conduits. Furthermore, practical yield stress fluids exhibit time-dependent behaviour such as viscoelasticity, elasticity, and thixotropy. The shear history dependent rheological behaviour of a viscoplastic fluid combined with its yielding behaviour adds another level of complexity to understanding its flow in different geometries. Wall-slip behaviour of yield stress fluids is another parameter that significantly affects their flow in confined geometries. In this context, the macroscopic motion of a viscoplastic fluid in a slender conduit is not only a function of its bulk rheology but also dependent on its interaction with the confining solid boundaries.

These complex effects are significant in the internal flow of yield stress fluids and are expected to manifest themselves in surprising flow scenarios including flow blockages and channelization in case of any geometric irregularities or non-uniformities. Furthermore, one might expect the flow irreversibility or asymmetry in case of flows in symmetric geometries, which is instigated by the shear history

dependent behaviour of the fluid. From this perspective, there has been interest on both the theoretical and experimental fronts to examine the flow of viscoplastic fluids in slender conduits [e.g. 1–7]. In this thesis, we aim to shed more light on this topic by experimentally studying three representative examples of viscoplastic fluid flows in confined geometries. In particular, the flow is examined either in parallel plate geometries, namely around an obstruction or in layered configurations, or in a capillary geometry. These three problems are listed as follows,

- Studying the flow patterns and yielding surfaces developing in the flow of a viscoplastic fluid along an obstructed Hele-Shaw cell.
- Characterising wall-slip behaviour of a prototype simple yield stress fluid in a pressure driven flow.
- Studying reactive multi-layered flow of viscoplastic fluids in a horizontal Hele-Shaw cell.

In the majority of the work, Carbopol is used as a model yield stress fluid, and direct visualization of the flow is exploited to assess the complex features of the flow. Broadly speaking, these flows all involve a yield stress fluid through a thin duct/channel. However, each flow problem is motivated by a separate application and designed to answer a particular research question.

In the following, an outline of the thesis, including a brief description of these three representative problems, and their intended research questions, objectives, and experimental approach are explained. First, an introduction to the industrial motivations, as well as a review of the background literature underlying rheology of our working yield stress fluid, and characteristics of the flow in a thin slot are given in Chapter 2. Then, three flow problems, listed above, are explained in three separate chapters. Note that each individual chapter introduction includes a detailed review of the literature relevant to the corresponding flow problem.

In the first phase of this research we consider the flow of Carbopol in an obstructed Hele-Shaw cell. This work is part of a series of articles focussing on the dynamics of viscoplastic flow through non-uniform slots. It follows on from a

theoretical discussion of obstructed and channelized flow in a Hele-Shaw cell [8]. The main motivations stem from drilling and fracture problems in the oil and gas industries. In these applications, a viscoplastic fluid is driven down fractures or other slender conduits and a main concern is the appearance of stagnant or plugged regions which can limit cementing and oil recovery [3, 7, 9–15]. In this context, flow around obstacles placed in a Hele-Shaw cell provides the simplest possible idealization of how a spatial non-uniformity in a slender conduit can create such blockages. This classical problem for viscous fluids, which provided laboratory realization of potential flow, was extended theoretically to Bingham fluids in [8]. The main focus of the first phase of this thesis is to reconsider the problem from the experimental perspective. Our objective is to first investigate the validity of theoretical findings and second examine the effect of non-ideal rheology of the fluid on flow configuration and plugged regions developing in the slot. This study is presented in detail in Chapter 3.

In the second phase of this research we study the wall-slip behaviour of Carbopol gels in a fully-developed Poiseuille flow. Apparent slip of viscoplastic fluids on the solid surfaces has been reported recently in many experimental studies [e.g. 16–18]. For a yield stress fluid, it not only changes the boundary condition at the solid surfaces, but also changes the flow threshold in the confined geometries [19]. In this context, the wall-slip behaviour of viscoplastic fluids significantly influences the flow kinematics and dynamics in slender conduits. In particular, the wall-slip behaviour of yield stress fluids plays an important role in many industrial applications in complex fluid transport such as oil-pipe transport systems [20, 21]. Hence, we are motivated to study the wall-slip behaviour of yield stress fluids in slender conduits. We focus on the fully developed flow of Carbopol gel which is known as a simple yield stress fluid in a glass capillary. A review of the relevant literature reveals a discrepancy between relationships reported for characterising the slip velocity as a function of wall-shear stress for Carbopol gels with different concentrations and for flow in different geometries [18, 19, 22–26]. In this study, we aim to revisit the problem in a Poiseuille flow and examine if there is a general relationship that describes the wall-slip behaviour of Carbopol gels. A description of experimental approach, and results are detailed in Chapter 4.

The third phase of this thesis is dedicated to the theoretical and experimental study of vertically stratified and reactive 3-layer flows in a Hele-Shaw cell. The fluid layers are miscible. The chemical reaction at the interface leads to the gelation and consequently local modification of the fluid rheology. An interesting application is in the production of large aspect ratio biocompatible hydrogels such as skin scaffolds. Considering the application of this work, what seems necessary is first to maintain a stable flow configuration and second to control the production rate, i.e. growth rate of gel layer. In this study, we examine the flow in a nearly horizontal configuration to understand the effect of buoyancy and extent of reaction on the stability of the flow. Beside, we investigate the growth of gel layer under stable flow conditions. Further detail on the industrial motivation, and the objectives as well as the results are presented in Chapter 5.

Finally, the main findings and contributions corresponding to each case study are summarized in Chapter 6. Furthermore, suggestions for the future direction of this research and its limitations and implications are discussed.

## Chapter 2

# Background

The present chapter serves as an introduction to the industrial motivation for this research, as well as to the scientific background concerning the complex behaviour of yield stress fluids, and characteristics of their flows in thin slots. The viscoplastic fluid flows along thin conduits occur in many geophysical and industrial settings. In Sec. 2.1, we explain a number of relevant applications in oil and gas industry, which provide the main motivations for much of this study. A detailed description of the viscoplastic fluid used in this study, i.e. Carbopol, and its behaviour is given in Sec. 2.2. In this section, we first explain the idealized constitutive laws for viscoplastic fluids, i.e. Bingham and Herschel-Bulkley models. Next, details of the rheology of Carbopol gels are given that highlight the discrepancies between the idealized models and complex behaviour of these fluids. At last, wall-slip behaviour of the Carbopol gels and its mechanism are explained. In Sec. 2.3, we outline the mathematical formulation of viscoplastic Hele-Shaw flow, which clarifies how the thin gap approximation simplifies the flow in this geometry. A summary of the information given in this chapter and an overview of general objective of this study are explained in Sec. 2.4.

### 2.1 Industrial motivations

A substantive number of working fluids in the oil industry, including waxy crude

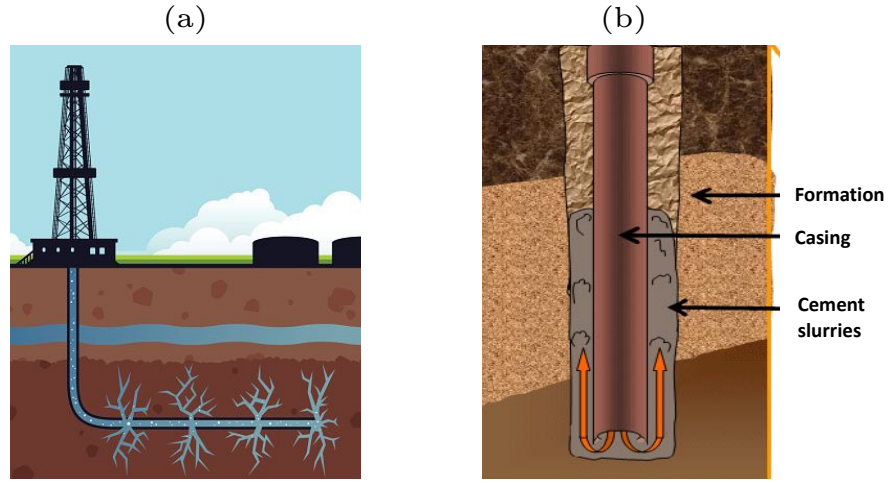


**Figure 2.1:** Flows of yield stress fluids along thin conduits occur in many geophysical and industrial settings. Two examples, which are related to the oil and gas industry, are presented here: (a) flow of crude oil or hydraulic fracturing fluids along the fractures in the rock formation (during the oil recovery process), and (b) flow of cement or mud along a thin annulus between casing and rock formation (during the cementing process). The images in panel (a) and panel (b) were taken from [27] and [28], respectively.

oil, drilling mud, cement, and proppant<sup>1</sup> laden slurries, behave like yield stress fluids and require a minimum pressure gradient to flow [9, 10]. The original motivation for much of this work stems from a number of relevant problems in the petroleum industries where blockage is a key consideration, including the transport of proppant laden slurries and crude oil in hydraulic fractures, as well as the flow of cement and drilling mud in the eccentric annulus between casing and rock formation [e.g. 3, 7, 14] (see Fig. 2.1).

Hydraulic fracturing is a technique for the stimulation of oil, gas, and geothermal reservoirs to maximize the extraction. The reservoir rocks are cracked by pressurized slurries, a mixture of hydraulic fluid and proppant, in order to make the paths through which the gas or oil flows to the wellbore. The proppant is used to keep

---

<sup>1</sup>Sand grains.

the fractures open after depressurizing the well. In order to enhance the proppant transport, the rheological properties of the fracture-fluid are changed to that of a viscoplastic fluid, by dissolving some material in it. At the end of hydraulic fracturing, the flowback phase attempts to clean the gelled fluids from the proppant-laden fracture. The rigid zones developing around the proppant or in slender part of the fractures, lead to the decrease in the recovery of fracture-fluid and oil extraction efficiency [11–13]. Another problem that we can address here is the problem of the flow of crude oil with viscoplastic rheological properties in porous reservoirs and hydraulic fractures, with application in oil extraction and recovery processes. Stagnant zones and dead areas of motionless oil developing in the slots, result in the localization of flow and consequently a considerable decrease of oil extraction [14, 15].

Another example that is relevant to the viscoplastic flows in slender conduits is the problem of mud removal and cement placement in a long narrow eccentric annulus between the casing and the rock formation. After drilling the wellbore and inserting the casing, cement is pumped down inside the casing, then it exits from the bottom of the well and displaces drilling mud along the annulus, and towards the surface of the well. The role of the cement is to support the wellbore and isolate the different fluid-bearing zones of the rock formation from one another and from the surface. In practice, the mud is not fully removed from the annulus, remaining on the narrower side of the annulus and around the obstructions. As the cement sets, the remaining mud in the annulus is de-watered and transforms to a porous medium along which formation fluid can migrate towards the other fluid-bearing zones [3].

All the aforementioned applications include the flow of a viscoplastic fluid in a thin slot. In the above examples, the yield stress of the fluid along with the heterogeneous structure of the slot and obstructions can be considered as the candidates for the creation of fouling layers and dead zones, which limit the efficiency of the industrial operations. Furthermore, wall-slip behaviour and time-dependent rheology of practical viscoplastic fluids are other parameters that might significantly affect their flows in confined geometries.

Overall, the non-trivial rheological behaviour of viscoplastic fluids along with their interaction with the solid surfaces complicate their flow in thin conduits. It implies the necessity of the comprehensive study of flow of these fluids in confined geometries.

## 2.2 Yield stress fluids

A substantive number of materials we deal with in our daily life such as butter, jam, toothpaste, cosmetic creams, etc. behave like viscoplastic fluids. Furthermore, viscoplastic fluids are ubiquitous in many industrial and natural processes; i.e. pulp suspensions in paper making, concrete in manufacturing, crude oil, cement, mud, and slurries in oil recovery and cementing processes, as well as landslides, mud and lava flows, and avalanches in natural processes [1, 29].

The common characteristic of these fluids is their yield stress which indicates their dual responses to the applied stresses; i.e. below the yield stress the material behaves like a solid, while above this threshold it deforms and flows like a liquid.

### 2.2.1 Idealized rheological models for viscoplastic fluids

The simplest model that describes the rheology of these fluids is known as Bingham constitutive law, which was obtained by adding the yield stress to the Newtonian viscosity. The tensorial form of the Bingham model is as follows,

$$\begin{aligned} \dot{\gamma}_{ij} &= 0 \quad \tau \leq \tau_Y \\ \tau_{ij} &= \left( \mu + \frac{\tau_Y}{\dot{\gamma}} \right) \dot{\gamma}_{ij} \quad \tau > \tau_Y \end{aligned} \quad (2.1)$$

where  $\mu$  is the plastic viscosity,  $\tau_{ij}$  is the deviatoric stress,  $\dot{\gamma}_{ij}$  is the deviatoric strain rate tensor, and  $\tau$ , and  $\dot{\gamma}$  represent the second invariants,

$$\tau = \sqrt{\frac{1}{2} \tau_{ij} \tau_{ji}} \quad (2.2)$$

$$\dot{\gamma} = \sqrt{\frac{1}{2} \dot{\gamma}_{ij} \dot{\gamma}_{ji}} \quad (2.3)$$



According to the Bingham constitutive law, the yielding occurs when the second invariant of the stress tensor overcomes the yielding threshold. This assumption is premised on the Von–Mises criterion of plasticity theory (Prager & Hodge 1951). Although the simplicity of the Bingham model permits efficient implementation in theoretical studies of viscoplastic fluids, in practice it cannot describe the rheology of real viscoplastic fluids. A popular generalization for the Bingham model is the Herschel–Bulkley law which takes the rate-dependence of the viscosity into account in the form of a power law,

$$\begin{aligned} \dot{\gamma}_{ij} &= 0 & \tau &\leq \tau_Y \\ \tau_{ij} &= \left( K \dot{\gamma}^{n-1} + \frac{\tau_Y}{\dot{\gamma}} \right) \dot{\gamma}_{ij} & \tau &> \tau_Y \end{aligned} \quad (2.4)$$

where  $K$  is the consistency and  $n$  is the power-law index of the material. For ( $n < 1$ ), the shear viscosity decreases with the shear rate which indicates the shear thinning behaviour of the material. Note that for practical yield stress fluids, the power-law index was found to lie in the range of 0.2–0.8 [30, 31]. Hence, the Herschel–Bulkley model considers the breakage of the structure of the material not only at the yielding point but also above the yielding point. From this perspective, the Herschel–Bulkley law provides a more realistic model for the rheology of viscoplastic fluids which usually show both yield stress and shear thinning.

### 2.2.2 Rheological characterization of Carbopol gels

The viscoplastic fluid used primarily in this experimental study is Carbopol gel. The optical transparency of this material along with its negligible thixotropy or aging behaviour makes it a good candidate to be used as a simple yield stress fluid in many experimental studies [1]. In this section, we present a detailed characterization of the rheological behaviour of Carbopol solutions.

The flow curve, i.e. stress-strain rate relation, for a Carbopol solution is shown in Fig. 2.2(a), the data were obtained from a shear stress controlled ramp-up test which is followed by a ramp-down test. As illustrated in Fig. 2.2(a), the rheological behaviour of the fluid in the ramp-down test is explained well by the Herschel–

Bulkley model. Furthermore, the flow curve does not show any discernible sign of hysteresis and shear-history dependence above the yielding point, which is the hallmark of the simple yield stress fluids. A comparison between the flow curve of Carbopol (Fig. 2.2(a)), and that obtained for a thixotropic yield stress fluid (Fig. 2.2(b)) clarifies this point more.

However, there are discrepancies between the results obtained during the ramp-up and ramp-down tests at low shear rates, which cannot be explained by an idealized constitutive law such as Herschel-Bulkley model. This can be attributed to the elastic behaviour of the material below the yielding point [32]. The dominant elastic behaviour of the Carbopol gel below the yielding point manifests itself in the finite deformation of the material at the start of the ramp-up curve and its elastic recoil at the end of the ramp-down curve [32]. The elastic recoil of the fluid leads to the negative strain rate below the yielding point that are absent from the logarithmic plot of flow curves in Fig. 2.2(a). The ramp-up test starts with the deformation of the material, which was initially at rest and in the solid regime. With the assumption that the material behaves like a pure elastic solid in this regime,  $\tau = G\gamma$ , where  $G$  and  $\gamma$  are the elastic modulus and deformation, respectively. Hence, in a linear ramp-up test with a constant rate of  $\alpha$ , i.e.  $\tau = \alpha t$ , and below the yielding point, the material is elastically deformed at a constant rate of  $\dot{\gamma} = \alpha/G$ . Accordingly, during the ramp-down test and when  $\tau < \tau_Y$ , the material progressively restores its elastic energy which leads to the negative shear rate. In the view of this and considering the non-thixotropic behaviour of simple yield stress fluids, one might expect that only the part of the flow curve corresponds to the solid regime is dependent on the ramp rate. Putz *et al.* [33] quantified the discrepancy between the ramp-up and ramp-down flow curve for a Carbopol solution and showed that it decreases by running the test at lower ramp rate, while the flow curve above the yielding point is insensitive to the ramp rate.

The creep test provides more information about the transient and steady-state behaviour of the fluid below and above the yielding point. The creep test includes measuring the deformation of the material during a series of constant shear stress tests after a preshear at a high rate (See Fig. 2.3(a)). The representative results for

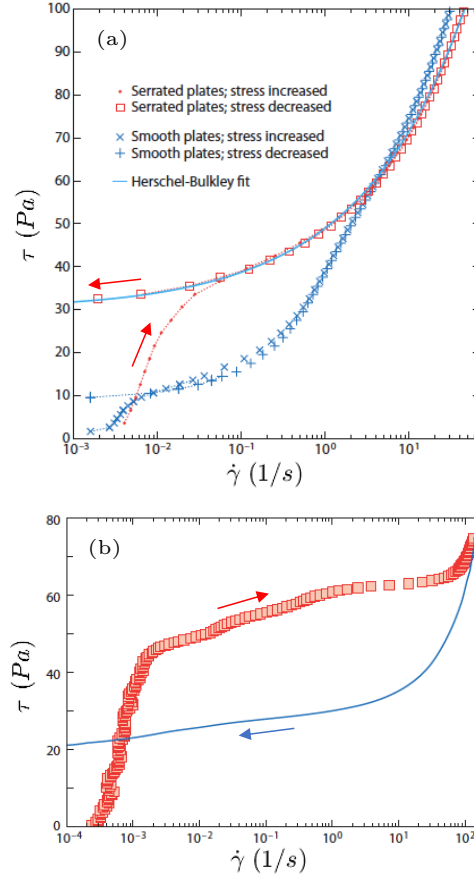


**Figure 2.2:** (a) Flow curves for a simple yield stress fluid, a Carbopol solution, measured by a stress controlled ramp-up and ramp-down test with a ramp-rate of 0.05 Pa/s. The red symbols represent the data obtained from tests with rough plates where slip of the gel on the surface is minimized. The red dots and squares denote the data for ramp-up and ramp-down tests, respectively. The light blue line gives the Herschel-Bulkley fit with  $\tau_Y = 30$  Pa,  $n = 0.34$ , and  $K = 19 \text{ Pa s}^n$ . The blue symbols represent the flow-curve obtained from experiments with smooth plates, where the gel slips on the plates. Here, the blue cross and plus symbols show the data measured from ramp-up and ramp-down experiments, respectively. The figure in panel (a) was taken from [29]. (b) Flow curve for a thixotropic yield stress fluid, a bentonite suspension. The data for increasing and decreasing stress ramps are presented by red squares and blue line, respectively. This flow curve shows discernible hysteresis above the yielding point, that is absent in the flow-curves shown in panel (a) for a simple yield stress fluid. The figure in panel (b) was taken from [34].

the evolution of shear rate at different shear stresses are shown in Fig. 2.3(b). For shear stresses greater than the yield stress, the shear rate reaches a steady value after a time which is a function of applied stresses. This time scale is undetectably short at large shear stresses, while a discernible unsteady regime is obtained for shear stresses near the yielding point. Below the yield stress, the unsteady flow is obtained during which the shear rate tends to zero, i.e.  $\dot{\gamma} \rightarrow 0$  as  $t \rightarrow \infty$ . For simple yield stress fluids such as Carbopol, over this regime, the shear rate decreases with time through  $\dot{\gamma} \propto t^{-m}$ , where  $m$  varies in the range of 0.6 to 1 [29]. From this view, the creep of the gel in this regime is similar to the primary creep observed in solids [35, 36]. As illustrated in Fig. 2.3(c), the flow curve of the material can be obtained by extracting steady state shear rate data from creep test, which is reminiscent of the one obtained from stress controlled ramp-down test (Fig. 2.2(a)).

Studying the dynamic response of the gel in an oscillatory test sheds more light on its behaviour in the solid regime. At sufficiently low strain the material behaves like an elastic solid, however the response to the strain is not instantaneous, which indicates the role of slight viscosity. A strain oscillatory test can be used to characterise the elastic and viscous effects of the material separately. The representative results obtained from an amplitude strain sweep test for a Carbopol solution is shown in Fig. 2.4(a). As clear from this figure there is a critical strain below which the elastic modulus ( $G'$ ), and viscous modulus ( $G''$ ) remain constant and the material exhibits linear behaviour. Over this linear region, the elastic modulus is much larger than the viscous modulus. However, as the strain increases gradually, the viscous modulus increases and finally surpass the elastic one at sufficiently large strains. It in turn indicates the yielding behaviour of the material.

As illustrated in Fig. 2.4(b), a frequency sweep test at the linear region confirms that the elastic modulus of the material is roughly independent of the frequency in this regime. Hence, a simple model of viscoelastic solid, i.e. Kelvin–Voigt, can be used to interpret the response of the material over this region. As indicated in Fig. 2.4(c), this model is symbolized by a spring and damper in parallel. According to this model, the elastic and viscous moduli of the material are obtained as  $G'(\gamma_0, \omega) = E$ , and  $G''(\gamma_0, \omega) = \eta\omega$ , where  $E$  and  $\eta$  are the elastic and viscous

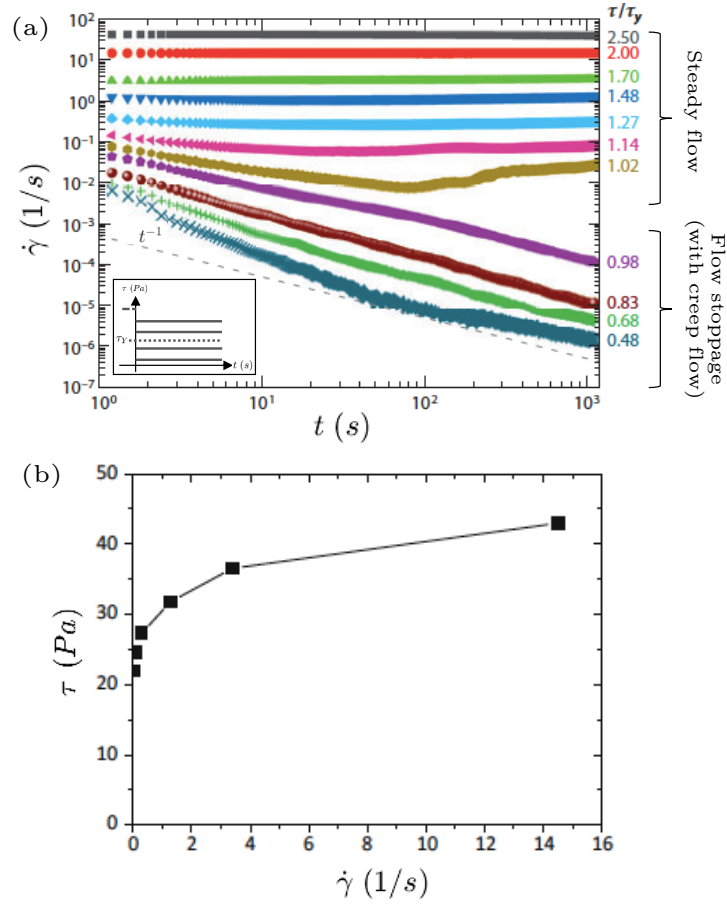


**Figure 2.3:** (a) Shear rate versus time measured during creep tests with a Couette geometry. A schematic representation of the creep experiments is shown in the inset of this figure. The tests have been performed for a Carbopol solution and for a number of different shear stresses ranging from  $0.48\tau_y$  to  $2.5\tau_y$ . As shown in this figure, for stresses below the yielding point, the shear rate decreases with time by  $t^{-1}$  (see gray dashed line). Near the yielding point, in particular for  $\tau = 1.02\tau_y$ , a transient solid-like creep behaviour was observed which is followed by an eventual steady flow. Figure in panel (a) is reproduced from [29]. (b) Steady-state flow curve obtained by measuring the steady shear rate from data presented in panel (a) for different shear stresses. Figures in panel (b) was taken from [32].

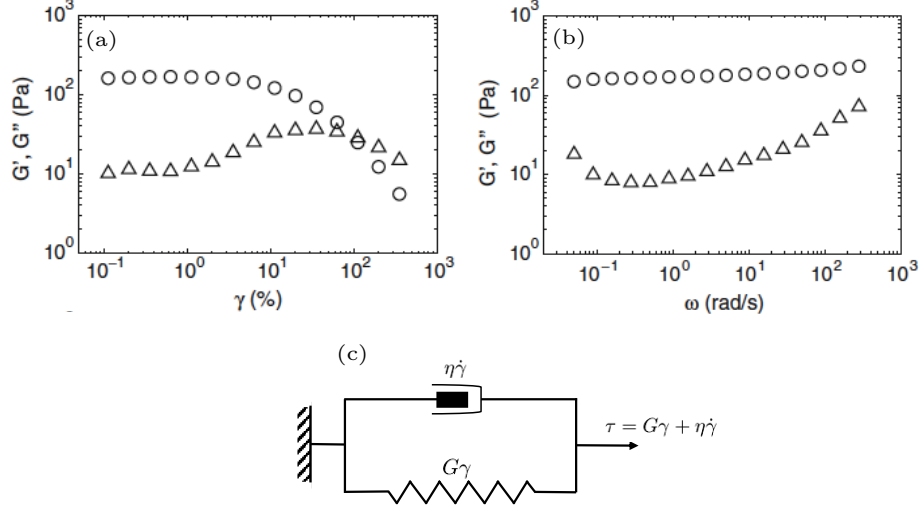


**Figure 2.4:** Dynamic rheological behaviour of a Carbopol solution: (a) Elastic modulus,  $G'$ , and viscous modulus,  $G''$ , versus strain measured during a strain sweep oscillatory test at  $\omega = 1$  rad/s. (b) Variation of elastic and viscous moduli with the frequency in the linear regime. The results were obtained from a frequency sweep test at  $\gamma = 1\%$ . In panel (a) and (b), the circles and triangles represent the elastic modulus and viscous modulus, respectively. (c) A schematic representation of the Kelvin-Voigt model which is associated with the behaviour of the material in the linear regime. Figures in panel (a) and (b) were taken from [40].

terms defined in Fig. 2.4.(c). Accordingly, the relaxation time of the material in the linear viscoelastic regime is given by  $\eta/E$ , or  $G''/\omega G'$ .

Furthermore, previous studies on the dynamic response of the Carbopol gel in the linear regime indicates that the elastic modulus of the material is not affected by the preshearing of the material before the test [32, 37]. In addition, no discernible sign of restructuration of the gel was observed in a single frequency oscillatory experiment in the linear regime following a preshear at a high rate [32, 37]. This is in contrast with the results obtained for the thixotropic yield stress fluids which present the evolution of the elastic modulus of the material by time in a similar test [34, 38, 39].

Overall, the experimental results reported above demonstrate that the Carbopol solutions do not exhibit any signature of aging or classical thixotropy which was identified for thixotropic yield stress fluids such as Laponite or Bentonite [32]. However, the fluid behaviour near the yielding point, i.e. solid-fluid coexistence regime, is more complex. The hysteric rheological behaviour of the fluid in this regime has been studied before in the literature [25, 41]. Poumaere *et al.* [25] studied the rheological behaviour of a similar Carbopol gel we used in our experiment (Carbopol 940 with weight concentration of 0.08%). They suggested that the transition from a solid behaviour to a viscous one (fully yielded) is not direct but mediated by an intermediate solid-fluid coexistence regime. They observed flow irreversibility in this intermediate regime in either steady torsional flow or capillary flow [25]. Despite these observations, the physical picture of irreversible solid-fluid transition and hysteric behaviour of the fluid near the yielding point have not been clear yet.

Recent experimental studies, which exploited both macroscopic rheological measurement and flow visualization, revealed that the yield stress fluids might exhibit flow inhomogeneities or localizations in terms of shear-banding or wall-slip [e.g. 25, 31, 42, 43]. The signature of these complexities can be observed in the measured-flow curves as the discrepancies between apparent shear rate and true shear rate of the material.

A number of the relevant studies reported long-lived, transient shear-banded flows near the yielding point for a particular type of Carbopol solution, i.e. ETD2050-Carbopol [31, 43, 44]. The signature of this phenomenon in the flow-curve of the material is the hysteresis near the yielding point so that the ramp-up curve lies above the ramp-down curve. This behaviour was attributed to the transient, localized fluidization of the gel which occurs in the solid-fluid transition regime [31, 43]. It should be underlined that such complexities have not been reported before for the Carbopol solution used in our experiments, i.e Carbopol 940 [25, 32, 33], and were not observed in our rheological measurements as well (see Sec. 3.2).

### 2.2.3 Wall-slip behaviour of Carbopol gels

Apparent slip over the smooth surfaces is ubiquitous in the flow of yield stress fluids and affects the flow dynamics and kinematics appreciably [1, 16, 31]. Figure 2.2(a) shows a comparison between the flow curves of Carbopol gels measured using rough surfaces and smooth surfaces where slip is possible. As clear from this figure, the slip behaviour of Carbopol on the smooth surfaces leads to the overestimation of the shear rate and accordingly underestimation of the apparent viscosity, particularly at low shear rates. For the case with slip, the flow curve obtained from the ramp-down test exhibits a kink at stresses lower than bulk yield stress and the apparent flow continues to be observed over this region. Below the bulk yield stress of the material, the flow curve sometimes displays an apparent yield stress below which the flow stops. This threshold which is known as slip-yield stress is strongly dependent on the surface chemistry and solid-fluid interactions and cannot be considered as a fluid characteristic.

The wall-slip behaviour of yield stress fluids including microgels, pastes, and suspensions of rigid or soft particles, is associated with the particle depletion near the shearing surfaces. The migration of the dispersed phase away from the bounding surfaces might arise from different origins, ranging from shear-induced particle migration to the electrostatic forces [17, 45]. This migration leads to the formation of a generally thin layer of base fluid, adjacent to the wall which is called apparent slip layer or Vand layer [46]. The viscosity of the apparent slip layer which is free of dispersed phase and consists only of the solvent is much lower than that of the bulk fluid. It in turn results in a sudden increase in the velocity gradient at the edge of the apparent slip layer, which facilitates the flow movement.

Although Carbopol has a roughly ill-defined structure, it can be considered as a suspension of micro-gel particles which are cross-linked [47]. Generally for suspensions of soft particles, the gel-particles can be modelled as elastic spheres with mean radius of  $R$  and Young modulus of  $E$  which are closely packed in a jammed configuration [16, 22] (see Fig. 2.5(a)). The jammed particles are pressed against each other and the wall and can flow past each other only if a stress greater than the



yield stress is applied. Therefore, one might expect that below the yielding point, the bulk-arrangement of the particles remained unchanged and they can move only by sliding at the wall. At rest, the particles are pushed toward the wall due to the bulk osmotic pressure of the suspension and hence they are elastically deformed against the wall in Hertzian contacts. During the slip, the particles slide on a thin layer of lubricant which is maintained by the hydrodynamic forces caused by the relative motion of the particles with respect to the wall and/or the repulsive forces between the particles and wall. Predictions provided by previous studies indicate that the slip layer thickness is in the order of tens of nano meters [e.g. 18, 24]. At such close proximity, the role of the short-range surface forces including attractive van der Waals forces, steric hindrance, electrostatic contributions, and hydrophobic–hydrophilic forces, becomes important [19]. Seth *et. al* [19] developed an idealized model for the wall-slip behaviour of suspensions of soft particles, which is based on elastohydrodynamic lubrication of particles against the wall with the presence of surface forces (see Fig. 2.5(b)). According to this model, the governing equations associated with the elastohydrodynamics in the thin lubricating film between a soft particle and the wall can be written as follows [19],

$$\nabla \cdot (\delta^3 \partial p) = -6\eta_s V_s \frac{\partial \delta}{\partial x} \quad (2.5)$$

$$\delta(x, y) = -h_0 + \frac{x^2 + y^2}{2R} + w(x, y) \quad (2.6)$$

$$w(x, y) = \frac{1}{G_p} \int_{-\infty}^{\infty} \int_{-\infty}^{\infty} \frac{p + p_d(\delta)}{\sqrt{(x - \varepsilon)^2 + (y - \theta)^2}} \quad (2.7)$$

where  $V_s$  is the slip velocity,  $\eta_s$  is the viscosity of solvent layer,  $(x, y)$  and  $(\varepsilon, \theta)$  are the Cartesian coordinates which their origin is located on the wall,  $\delta(x, y)$  is the thickness of layer developing between the particle and shearing surface,  $h_0$  is the initial deformation of the particle at rest,  $w(x, y)$  is the total elastic deformation of the particle,  $p(x, y)$  represents the hydrodynamic pressure in the lubricating layer, and  $p_d$  indicates the pressure caused by the attractive and repulsive forces. The elastic modulus of the particle is denoted by  $G_p = \pi E / (1 - \nu^2)$ , where  $\nu$  is the Poisson's ratio of the particle. Seth *et al.* [19] used a scaling analysis as well as a numerical simulation to solve the above equations and characterise the sliding

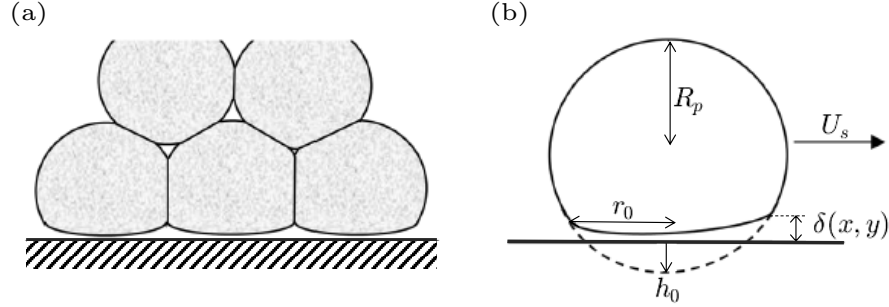


**Figure 2.5:** Schematic images representing (a) the jammed structure of a suspension of soft particles near the wall, (b) a detailed view of a soft particle sliding on the wall; the particle with the radius of  $R_p$  is squeezed against the wall which leads to the compression distance of  $h_0$  and a creation of contacting facet with radius of  $r_0$ . The particle slips against the wall with the speed of  $U_s$ . This is attributed to the formation of a lubricating layer of solvent with the thickness of  $\delta(x, y)$  between the particle and the wall. Reproduced from [16, 48].

velocity of the particle. They predicted two different regimes of slip depending on the chemistry of the shearing surface and its interaction with the particle.

For weakly adhering surfaces, the lubrication force dominates and the slip mechanism can be explained well by the *elastohydrodynamic-lubrication* theory [18, 19]. Due to the presence of short-range attractive forces, the particles attach to the wall when they are at rest. The sliding threshold is linked to the nature of the attractive forces. It was shown that for van der Waals forces,  $\tau_{sy} \sim G_0/R_p^{3/4}A^{1/4}$ , where  $A$  is the effective Hamaker constant between the particle and the shearing surface separated by a water layer [19]. As the applied stress exceeds the sliding threshold, the solid surface and adjacent particle interact by non-contact elastohydrodynamic forces caused by the relative motion of squeezed soft particle and the shearing surface. At rest, the surface of a soft particle, next to the shearing surface, is compressed and changed to the flat facet. Relative motion between the solvent and the squeezed particle deforms the flat facet, asymmetrically (see Fig. 2.6(a)). The resultant pressure distribution in the converging layer between deformed particle

and solid surface maintain the lubricant layer and pushes the particle away from the wall. The balance between the bulk osmotic-pressure of the suspension and the lift force, resulting from elastohydrodynamic lubrication, dictates the thickness of apparent slip layer. Considering the dominant effect of lubrication forces, a scaling analysis of the governing equations shows that the slip layer thickens by increasing the slip velocity through  $\delta = (\frac{\eta_s U_s R_p}{G_p})^{1/2}$ . Accordingly, it can be easily shown that the slip velocity changes with the wall-shear stress by a quadratic scaling law  $U_s \sim \tau_w^2$ , when the sliding threshold is negligible in comparison with the wall-shear stress [18, 19].

In the case where repulsive forces between the particles and shearing surface dominate, the slip mechanism is associated with the *hydrodynamic lubrication* of the particles over a layer of solvent; the thickness of this layer is independent of the slip velocity and determined by an interplay between the repulsive forces and bulk osmotic pressure of the suspension [19]. It can explain the mechanism of apparent slip in weak flows over the hydrophilic surfaces where they are preferentially wetted by the solvent and sliding yield stress is negligible. The viscous forces are weak relative to the short-range repulsive forces, hence the particle-wall interaction leads to the symmetric deformation of the particle and the particle facet is roughly flat. The net lift force caused by the average pressure beneath the particle is negligible (see Fig. 2.6(b)). It implies that in this regime, the slip velocity changes linearly with the wall-shear stress. However, for stronger flows the lubrication forces contribute to elastic deformation of the particles and the linear dependence of the slip velocity on the wall-shear stress is violated. The transition from the linear to non-linear regime is dependent on the range of repulsive forces [19].

The advancement of the flow visualization techniques during the last decades allows for direct visualization of the flow and quantitative measurement of velocity field near the solid boundaries. Recently, a number of experimental studies have been performed to analyse the slip-behaviour of suspensions of soft particles by exploiting the direct measurements of local velocity field either in a steady torsional flow or in a capillary flow [e.g. 22, 24, 25]. However, as explained more in detail in Sec. 4.1, an inspection of the relevant literature reveals discrepancy between mod-

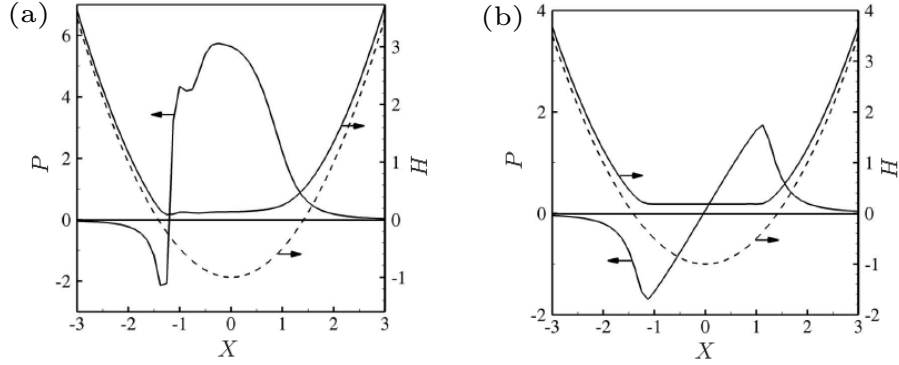


**Figure 2.6:** Variation of the scaled pressure developing in the lubrication layer,  $P = p/p_0$ , and scaled thickness of this layer along the center of the particle,  $H = \delta/h_0$ , with the dimensionless horizontal distance from the center of particle,  $X = x/r_0$ . Here,  $P_0$  represents the characteristic hydrodynamic pressure in the lubricating film, which is obtained from the balance of the viscous and pressure terms in Eq. (2.5),  $p_0 = 6\eta_s U_s R_p^{1/2}/h_0^{3/2}$ . Panel (a) presents the results for an elastohydrodynamically lubricated particle squeezed against a weakly attractive surface, and panel (b) shows the hydrodynamically lubricated particle pressed against a repulsive surface. Reproduced from [19].

els reported for characterising the slip velocity as a function of wall-shear stress for Carbopol gels with different concentrations and for flow in different geometries [18, 19, 22–26]. Overall, despite the idealized slip model described above, the wall-slip behaviour of Carbopol gel on smooth surfaces is non-trivial and has not been fully understood. In particular, the dependence of the slip velocity on the wall-shear stress, rheology of solvent, and the microstructure of the material has not been clear yet.

In addition to the studies done on characterising the slip behaviour of suspensions of soft particles, a series of works focused on providing methods to avoid the wall slip [16, 49–53]. Modifying the surface roughness by sticking on sandpaper to or by sandblasting the surfaces has been recognized to be the simplest way to suppress the wall slip [49, 50, 52]. However, these techniques change the optical properties of the surfaces. Another technique to inhibit the wall slip which has been intro-

duced recently, consists of chemical modification of the surfaces by incorporating attractive interactions [51, 53]. For example, Christel *et al.* [51] proposes a simple method to chemically treat the polymethyl methacrylate (PMMA) substrates in order to inhibit the slip of carbopol solutions on them. According to this technique, the PMMA substrates are treated by polyethylenimine PEI, which is formed of linear chains  $H(NHCH_2CH_2)_nNH_2^+$ . Due to the interaction of secondary amino groups with PMMA ester groups, PEI absorbs on the surface of substrates. In case of the flow of Carbopol on the treated substrate, microgels attach to the surface due to the formation of complexes between amino groups of PEI and  $COOH^-$  pending groups of Carbopol. Therefore, a stick layer of Carbopol microgels, with the thickness of a few microns, forms on the surface of the sheets which inhibits the wall slip.

### 2.3 Hele-Shaw flow

The Hele-Shaw cell provides a simple experimental and theoretical model geometry in which to study flow along slender conduits. Narrow gap approximation simplifies the flow of viscoplastic fluids in this geometry. To clarify this point more, the theoretical modelling of the flow of an idealized Bingham or Herschel-Bulkley fluid in a Hele-Shaw cell that contains obstructions is explained in this section.<sup>2</sup>

To help define this flow field, we consider the steady flow of an incompressible fluid down a narrow slot of spatially varying width. We assume that the slot is symmetrical about its midplane and use a Cartesian coordinate system to describe the geometry (see Fig. 2.7). We align the slot's midplane with  $z = 0$ , and locate the side walls at  $z = \pm h(x, y)/2$ . The fluid has velocity  $u(x, t)$ , pressure  $p(x, t)$  and a stress tensor  $\tau_{jk} - p\delta_{jk}$ . We assume that there is no penetration and no slip on the walls of the slot, such that  $u = 0$  on  $z = \pm h(x, y)/2$ .

For slow flow down a relatively narrow slot, standard analysis based on the thinness of the gap indicates that the shear stresses  $(\tau_{xz}, \tau_{yz})$  dominate the force balance

---

<sup>2</sup>A version of this section was published in *Journal of Fluid Mechanics* [8].

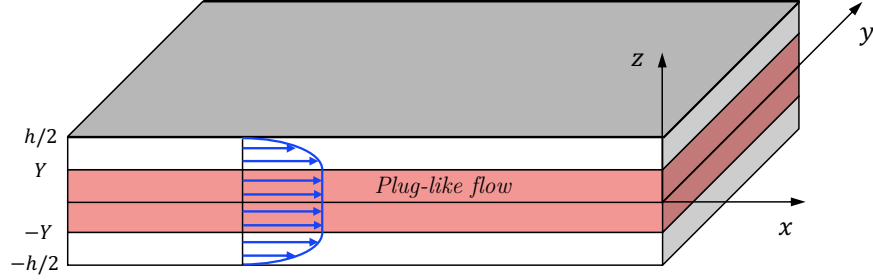


**Figure 2.7:** A schematic image of the geometry for a yield stress fluid in a Hele-Shaw cell.

and the governing Stokes equation of the flow reduce to,

$$\frac{\partial p}{\partial x} = \frac{\partial \tau_{xz}}{\partial z}, \quad \frac{\partial p}{\partial y} = \frac{\partial \tau_{yz}}{\partial z}, \quad \frac{\partial p}{\partial z} = 0. \quad (2.8a, b, c)$$

Hence, given the symmetry about the midplane of the slot ( $z = 0$ ),

$$p = p(x, y), \quad (\tau_{xz}, \tau_{yz}) = z \left( \frac{\partial p}{\partial x}, \frac{\partial p}{\partial y} \right). \quad (2.9a, b)$$

For a Newtonian fluid, it can be shown that the governing equation of Hele-Shaw flow simplifies to the Laplace equation of pressure or stream function which leads to the potential flow that provides the foundation for Henry Selby Hele-Shaw's classical visualizations of potential flow around obstacles (e.g. [54]). For viscoplastic fluids, the Hele-Shaw flow becomes more complex. In case of a yield stress fluid, the theoretical analysis of general governing equations for the Hele-Shaw flow, results in a non-linear filtration problem [55].

Consider the Bingham model as an idealized viscoplastic constitutive law for the working fluid. In this geometry, one also expects the shear across the slot to dominate the deformation rate tensor, and so

$$\begin{pmatrix} \tau_{xz} \\ \tau_{yz} \end{pmatrix} \approx \left( \mu + \frac{\tau_Y}{\dot{\gamma}} \right) \begin{pmatrix} \partial u / \partial z \\ \partial v / \partial z \end{pmatrix} \quad \text{if} \quad \tau \approx \sqrt{\tau_{xz}^2 + \tau_{yz}^2} > \tau_Y, \quad (2.10)$$

where  $\dot{\gamma} \approx \sqrt{(\partial u / \partial z)^2 + (\partial v / \partial z)^2}$ , and  $\mu$  is the viscosity and  $\tau_Y$  is the yield stress.

However, given (2.9),  $\sqrt{\tau_{xz}^2 + \tau_{yz}^2}$  inevitably falls below the yield stress near  $z = 0$ , which suggests that the flow is plug-like over the central section of the cell, with  $\partial u / \partial z \approx \partial v / \partial z \approx 0$ .

After integrating Eq. (2.9b) with Eq. (2.10), we find

$$\begin{pmatrix} u \\ v \end{pmatrix} = -\frac{1}{2\mu} \left[ \max(h/2 - Y, 0)^2 - \max(|z| - Y, 0)^2 \right] \begin{pmatrix} p_x \\ p_y \end{pmatrix}, \quad (2.11)$$

where the “yield surface” is

$$Y = \frac{\tau_Y}{(p_x^2 + p_y^2)^{1/2}}. \quad (2.12)$$

Here, and in subsequent expressions, the  $x$  and  $y$  subscripts indicate partial derivatives. Equation (2.11) demonstrates the plug-like character of the flow in  $|z| < Y$  for  $h/2 > Y$ . Despite this, and as described more in Sec. 3.1, the plug flow is nevertheless able to deform along the  $x - y$  plane. The fluid within  $|z| < Y < h/2$  cannot therefore be truly rigid, but is a “pseudo-plug” [56, 57], where the shear stresses no longer dominate the stress state. Instead the fluid is held just above the yield stress by a combination of shear and extensional stresses. On the other hand, if  $Y \rightarrow h/2$ , the channel becomes fully plugged up, flow halts and the fluid is genuinely unyielded.

We now place the equations into dimensionless form. Let  $U_c$  denote the mean flow speed down the slot, and  $H$  denote the typical width. The characteristic lengthscale  $\ell_c \gg H$  along the slot is set by the natural dimension of the obstacles. We then remove dimensions by defining the scaled variables,

$$(\hat{x}, \hat{y}) = \frac{(x, y)}{\ell_c}, \quad (\hat{z}, \hat{h}, \hat{Y}) = \frac{(z, h, Y)}{H}, \quad (\hat{u}, \hat{v}) = \frac{(u, v)}{U_c}, \quad \hat{p} = \frac{H^2 p}{\mu U_c \ell_c}. \quad (2.13)$$

We also define a dimensionless streamfunction  $\hat{\psi}$  for the flux,

$$\begin{pmatrix} -\hat{\psi}_{\hat{y}} \\ \hat{\psi}_{\hat{x}} \end{pmatrix} = 2 \int_0^{\hat{h}/2} \begin{pmatrix} \hat{u} \\ \hat{v} \end{pmatrix} d\hat{z}, \quad (2.14)$$

in order to satisfy the slot-integrated continuity equation.

From Eq. (2.11) and Eq. (2.14), and after dropping the hat decoration, we find

$$\begin{pmatrix} \psi_y \\ -\psi_x \end{pmatrix} = \frac{q}{S} \begin{pmatrix} p_x \\ p_y \end{pmatrix}, \quad (2.15)$$

where the magnitudes of the flux  $q \equiv \sqrt{\psi_x^2 + \psi_y^2}$  and pressure gradient  $S \equiv \sqrt{p_x^2 + p_y^2}$  are related by

$$q = \frac{1}{3} [\max(h/2 - Y, 0)]^2 (h + Y) S, \quad (2.16)$$

and the dimensionless  $Y$  and Bingham number  $B$  are

$$Y = \frac{B}{S}, \quad B = \frac{H\tau_Y}{\mu U_c}. \quad (2.17a, b)$$

Equation (2.16) explicitly contains the yield condition for the full slot:  $q > 0$  for  $h/2 > Y$  or  $B/(h/2) < S$ . Formally we may invert Eq. (2.16) to give, for some function  $S(q; B, h)$ ,

$$\begin{pmatrix} p_x \\ p_y \end{pmatrix} = \frac{S(q; B, h)}{q} \begin{pmatrix} \psi_y \\ -\psi_x \end{pmatrix}. \quad (2.18)$$

The pressure gradient function  $S(q; B, h)$  is a critical ingredient in our model for the viscoplastic Hele-Shaw flow. The function has the limiting forms

$$S(q; B, h) \sim 2\frac{B}{h} + \frac{4}{h^2} \sqrt{Bq} \quad \text{for } q \rightarrow 0, \quad (2.19)$$

and

$$S(q; B, h) \sim 12qh^{-3} \quad \text{for } q \gg 1, \quad (2.20)$$

the second of which coincides with the Newtonian function  $S(q; B=0, h) = 12qh^{-3}$ . The relation  $S = S(q; B, h)$  can also be viewed as a form of Darcy's law, which



establishes the link between flows in Hele-Shaw cells and porous media. For the Hele-Shaw cell,  $S(q; B, h)$  encodes the fluid rheology and can be adjusted to accommodate different constitutive laws. For example, if we use the Herschel-Bulkley model, rather than the Bingham law, then Eq. (2.16) is replaced by

$$q = \frac{2}{(n+1)(2+1/n)} [\max(h/2 - Y, 0)]^{1+1/n} [(n+1)h/2 + nY] S^{1/n}, \quad (2.21)$$

where  $n$  is the power-law index, and the non-dimensionalization must be reworked to replace  $\mu$  in Eq. (2.13) and Eq. (2.17b) by a characteristic viscosity  $\mu_* = K(U_c/H)^{n-1}$ , where  $K$  is the consistency of the fluid. A key point here is that both of the forms of  $S(q; B, h)$  in Eq. (2.16) and Eq. (2.21) contain a threshold below which flow ceases, which is the hallmark of a yield-stress fluid. The flow is essentially characterised by  $S(q; B, h)$  which encodes the rheology of the fluid. The key point to simulate the flow in the Hele-Shaw cell, is to determine the pressure gradient function,  $S(q; B, h)$ .

By setting equal the mixed partial derivatives of the pressure in Eq. (2.18), we arrive at the governing equation of the model, which is a nonlinear elliptic problem for the streamfunction [cf. 3, 55],

$$\nabla \cdot \left( \frac{S}{q} \nabla \psi \right) \equiv (q^{-1} S \psi_x)_x + (q^{-1} S \psi_y)_y = 0. \quad (2.22)$$

The non-linear elliptic problem discussed above can be solved numerically by applying an augmented Lagrangian scheme and a finite difference method. The details of the numerical scheme are described in [8]. For flow around complete blockages of the cell,  $H$  is set to be the uniform width of the slot outside these obstacles (so that  $h = 1/2$  there). The length scale,  $\ell_c$ , is then given by the characteristic dimension of the obstruction (its radius, in the case of a circular obstacle). The computational domain is much larger than the obstruction and the solution is required to match to a far-field uniform flow in the positive  $x$ -direction, which is unity given the scaling by the mean flow speed  $U_c$ . Hence,  $\psi \rightarrow -y$  for  $x^2 + y^2 \gg 1$ .

Hewitt et al. [8] studied the flow of a Bingham fluid in an obstructed Hele-Shaw

cell and characterised the flow patterns and plugged regions developing around the obstructions, by using the aforementioned numerical approach. Figure 2.8 shows the streamlines of the flow around an isolated disk confined in a Hele-Shaw cell, for different Bingham numbers. Considering the symmetric solutions, the flow over one quarter of the channel is shown in Fig. 2.8. As indicated in this figure, the plug regions appear at the leading and trailing edges of the obstacle where the magnitude of the pressure gradient vanishes. As the Bingham number is increased, the stagnant regions become longer, which has the unexpected effect of funnelling the fluid past the sides of the obstacle in increasingly fast-moving boundary layers. They also examined the hydrodynamic interactions between the cylindrical obstacles, oriented either with the flow direction or perpendicular to it. Figure 2.9 indicates the flow around a periodic array of circular contractions arranged perpendicular and parallel to the flow direction. For perpendicular arrangements of the contractions, the flow is guided to the gap between obstacles and it leads to an increase in maximum velocity as well as delay in plugging up of the obstacles (see Fig. 2.9(a)). However, for this orientation, hydrodynamic interactions of the obstacles have minor effects on the flow pattern and size of the plug regions. Instead, when the obstacles are aligned in the direction of flow, hydrodynamic interference of contractions may lead to the channelization of the flow and significantly change the flow patterns. In case of large Bingham numbers, the plugs of neighbouring obstacles are merged and a stagnant rigid zone forms that bridges the gaps between the objects (see Fig. 2.9(b)).

## 2.4 Summary

The most important feature of viscoplastic fluids is their yield stress which makes their flow in thin conduits complex. Previously, theoretical and numerical approaches have been exploited to examine the effect of yield stress of these fluids on their flow in different geometries. These studies have been developed based on idealized models for the rheology of the viscoplastic fluids such as Bingham or Herschel-Bulkley constitutive law. In the research community, Carbopol has been considered as a model material for experimental investigation of the flow of yield stress fluids in different geometries and verification of the corresponding the-

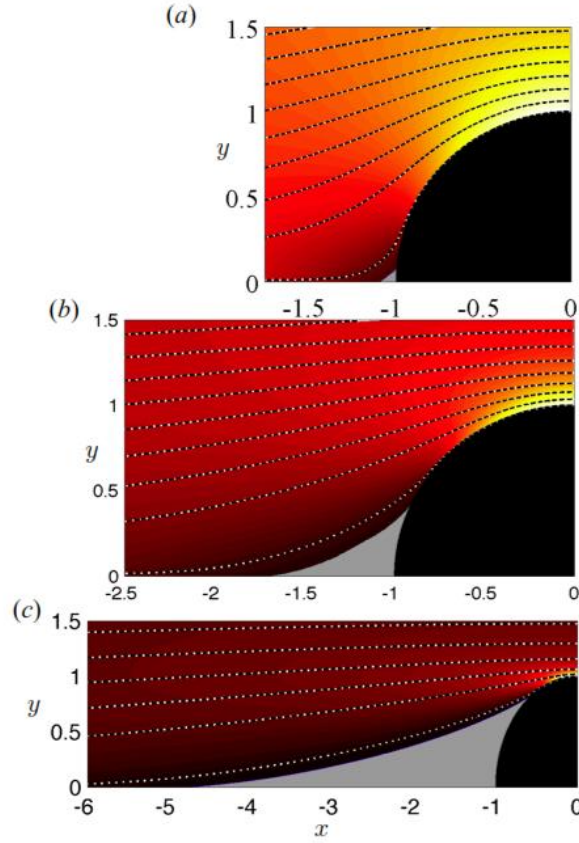


**Figure 2.8:** Streamlines with a contour map of  $q$  for the flow of a Bingham fluid around a disk embedded in a Hele-Shaw cell with the depth of  $h = 1$ , and for (a)  $B = 1.92$ , (b)  $B = 60$ , (c)  $B = 9600$ . Plug regions are shaded [8].

oretical findings. Carbopol has been traditionally known as a simple yield stress fluid with negligible thixotropy, which its steady state rheological behaviour can be explained well by the Herschel-Bulkley constitutive law. However, the detailed rheological studies of the Carbopol revealed complexities in terms of time dependent behaviour or wall-slip behaviour which violate the traditional picture.

The measured flow curves of the material show discernible hysteresis around the yielding point. Furthermore, the material exhibit elastic behaviour below the yield-

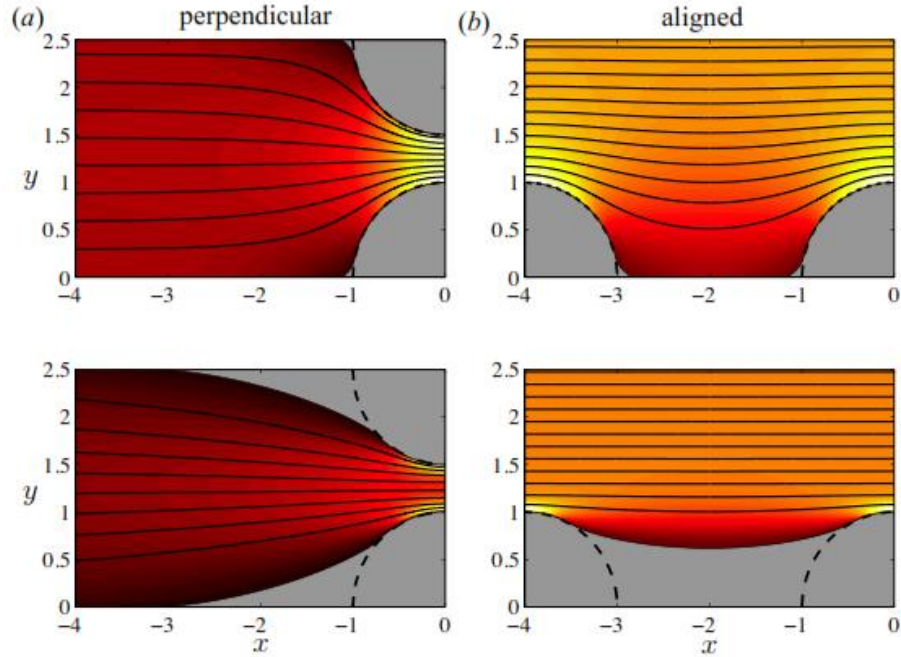


**Figure 2.9:** Flow past periodic arrays of circular contractions (with contraction ratio of 0.1). (a) Streamlines and a contour map of  $q$  for contractions arranged perpendicular to the flow and (b) aligned with the flow. For top row,  $B = 4.8$  and for lower row,  $B = 1228.8$ . Plug regions are shaded [8].

ing point which its signature was observed in the creep and dynamic tests. Besides, Carbopol, like many other complex fluids, exhibits slip on the bounding walls which significantly complicates its internal flow along thin conduits. It not only changes tangential velocity at the fluid-solid interface, but also changes the threshold above which the fluid flows.

Overall, the recent detailed rheological investigations indicated that there are some complexities involved in the practical rheological behaviour of Carbopol, which cannot be described well by an idealized model like Bingham and Herschel-Bulkley. Hence, one might expect that the flow of practical yield stress fluids in different

complex geometries cannot be explained well by the theoretical models developed based on Bingham or Herschel-Bulkley constitutive laws. In this thesis, we attempt to consider how these non-ideal rheological properties of the material manifest itself in a number of different flows in thin conduits. It provides a detailed survey of the discrepancies between theory and experiments as well as an insight into understanding the origin of these discrepancies. Note that in most of the cases, we consider the flow in a narrow geometry of a Hele-Shaw cell in which the thin gap approximation leads to the simplification of flow (as explained in Sec. 2.3).

## Chapter 3

# Experiments on obstructed viscoplastic flow in a Hele-Shaw cell <sup>1</sup>

### 3.1 Introduction

Slow viscous flow around an obstacle is a classical problem in fluid mechanics, with its analysis paving the way for the resolution of the so-called Stokes paradox and the development of matched asymptotic expansions. When placed into the confines of a narrow slot - a Hele-Shaw cell - the flow problem becomes (at leading order) equivalent to two-dimensional potential flow around an obstacle. In either case, the problem has fore-aft symmetry owing to the reversibility of the steady flow field.

Here, we are concerned with the generalization of these flow problems to the situation in which a complex fluid flows around an obstacle. In particular, following recent work on soft matter and complex fluids, we address the problem of viscoplastic flow around obstacles in a Hele-Shaw cell. The practical applications are widespread, particularly for drilling and fracture problems in the oil and gas in-

---

<sup>1</sup>A version of this chapter was published in *Physical Review Fluids* [58].

dustries where unwanted blockages are a key consideration [e.g. 3, 7, 11–15]. We study the creation of the blockages in the non-uniform slots by breaking it down to an idealized problem of flow around obstacles in a Hele–Shaw cell. Viscoplastic flows around obstacles have previously been considered in unconfined geometries, both theoretically and experimentally [e.g. 59–64]. For the flow around cylinders and spheres, the yield stress ensures that fluid motion becomes localized around the obstacle, alleviating the Stokes paradox without recourse to inertia. Moreover, theory based on the Herschel-Bulkley constitutive law again predicts fore-aft symmetry. In detail, the flow pattern consists of a ‘bubble’ of yielded material surrounding the obstacle, with triangular or conical plugs attached to its front and back. By contrast, experiments show the surprising feature that the flow and attached plugs are not fore-aft symmetrical. Ozogul et al. [64], for example, studied the flow of a yield stress fluid around a circular cylinder in a Poiseuille flow. They reported a significant difference between the size of the rigid zones developing at the front and rear of the cylinder, even for extremely low Reynolds numbers. In addition, they observed a region of negative wake behind the obstacle which was reported before in the case of flow of viscoplastic fluid around a falling sphere or cylinder [60, 61].

Viscoelastic liquids also display such asymmetry, an effect attributed to the viscoelastic relaxation of the stress [65, 66]. Harlen [65] studied the flow of a viscoelastic fluid past a sedimenting sphere numerically and delineated two competing effects for the viscoelastic problem. One is an extensional stress effect, i.e. the normally coiled polymers are stretched out in passing the sphere, and then in the wake they recoil to pull the fluid along. This “extends” the wake and weakens the flow. The other effect is due to the relaxation of the shear stress as the fluid flows around the sphere. Even though the shear rates are highest at the equator (with the flow pole-on) the build-up of the shear stresses is delayed and the maximum is reached only on the far side of the sphere. This stress then relaxes even further downstream, and is enhanced by the longer residence in the lee. Harlen [65] claims the latter generates the negative wake.

Following on for viscoplastic fluid, non-ideal rheological effects such as elastic-

ity or thixotropy have been proposed to explain the asymmetry [60, 67, 68]. In this concept, the signature of relaxation in the fluid, in terms of viscoelasticity or thixotropy, is expected to be the fore-aft asymmetry of the flow around the obstacle. The effect of thixotropy on the loss of fore-aft symmetry has been explained by the fact that the structure of the fluid is broken, and thus the viscosity is reduced as it passes the obstacle. This leads to the difference between the viscosity and yield stress of the fluid at the vicinity of the leading and trailing edges of the obstacle [69]. However, the breakage of fore-aft symmetry have been extensively reported in the literature for flow of simple yield stress fluids with negligible ageing and thixotropic behaviour [60, 61, 63, 64]. Recently, transient numerical studies of the problem indicated that the breakage of fore-aft symmetry of the flow around particles is not caused necessarily by thixotropy and suggested that the coupling of the elastic and plastic properties of the fluid and their contribution to the flow can be considered to be the cause [68, 70]. Cheddadi et al. [70] performed computations based on an elastoviscoplastic model [71] to simulate the flow of a mono-layer liquid foam around a circular obstacle in a thin slot. The study highlights the importance of the elastic contribution on the fluid dynamics around the obstacle. They found accurate predictions of corresponding experimental results obtained by Dollet et al. [72] and indicated a strong fore-aft asymmetry with an overshoot in the velocity at the downstream edge of the obstacle, even at very slow flows.

In a narrow slot (Fig. 3.1(a)) , the situation is very different in two important ways: the flow is forced to yield against the walls in order to move through the slot, and the shear across the slot dominates the strain-rate tensor of the fluid. These differences are well known, and their implications are demonstrated in the expected flow profiles illustrated in Fig. 3.1. For unidirectional flow down a uniform cell, the profile is characterised by shear-layers against the walls, together with a central rigid plug, as shown in Fig. 3.1(b). When the flow encounters an obstacle in the slot, however, the fluid must slow down and be diverted sideways, preventing the central region from remaining truly rigid. Instead, stresses in the plane of the slot become important to break the plug and hold the central region marginally above the yield stress [56, 57]. The flow profile across the slot remains plug-like, and the central region better referred to as a ‘pseudo-plug’ [8, 29]. As illustrated



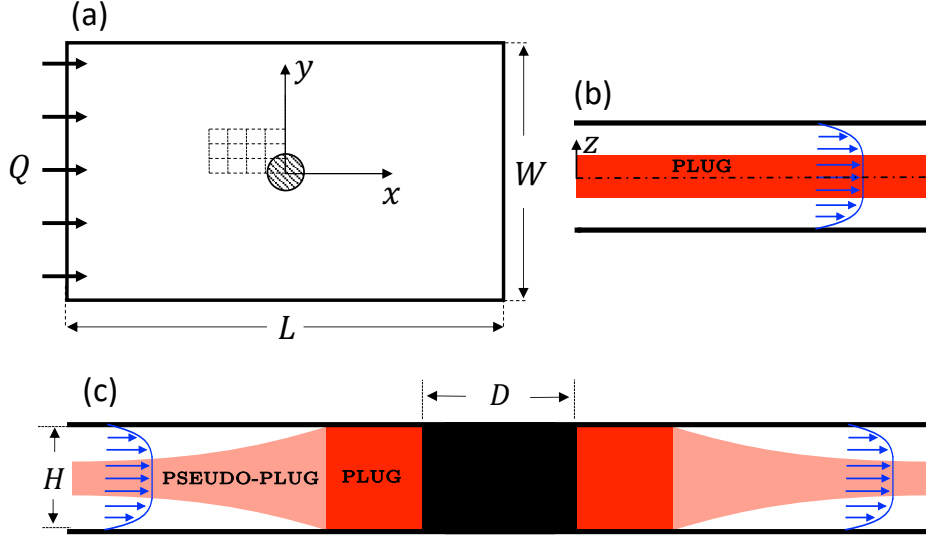


**Figure 3.1:** Viscoplastic flow through a Hele-Shaw cell containing an obstacle. The plane of the cell is shown in (a), where the grid represents the mosaic pattern used to create the composite images in Fig. 3.5. A velocity profile for flow down a uniform, unobstructed cell, with a central rigid plug, is shown in (b), while the corresponding profile through the centerline of the obstructed cell ( $y = 0$ ) is shown in (c), with a shaded pseudo-plug that widens to fill the cell and become truly rigid near the obstacle.

in Fig. 3.1(c), the thickness and speed of the plug-like flow varies along the slot, widening in the vicinity of the obstacle. Eventually, the pseudo-plug can grow to fill the cell, at which point the slot becomes spanned by a genuine rigid plug. The distinction between a rigid plug filling the cell and a central, moving pseudo-plug bounded by sheared fluid is a key detail of these flows, ensuring that there is no “lubrication paradox” of the sort that has been mistakenly proposed in the past [29].

Confined viscoplastic flow down a narrow slot is therefore rather different than the unconfined flows previously studied; the flow is directed primarily along the slot, rendering it quasi-two-dimensional, but the shear occurs mainly across the slot according to a known profile. Thus, unlike in an unconfined geometry where

all the velocity gradients must be measured, the velocity in the cell's midplane provides a direct gauge of the key strain rates. In addition, the shear stresses across the gap provide the main resistance to flow, weakening any effects of the extensional stresses, and further simplifying the expected rheological behaviour. In other words, the Hele-Shaw cell provides a transparent and definitive setting in which to assess non-ideal rheological effects in complex flows (*cf.* [73]).

The current work follows on from a theoretical study [8] of viscoplastic flow around cylindrical obstacles in Hele-Shaw cells. The theoretical work has been developed based on thin gap approximation and an idealized Bingham model for the rheology of the fluid. As for the unconfined problem, the theory again predicts that the flow field is fore-aft symmetric. Moreover, the pseudo-plugs do indeed expand to fill the cell at the front and back of the obstacle. As described before, the flow in a confined narrow slot is somewhat simpler and more constrained than the unconfined flow previously studied. Knowing this, the chief question raised here is if the flow of a practical yield stress fluid around an obstacle in a Hele-Shaw cell is asymmetrical, as it is in unconfined geometry. We attempt to answer this question here. The very different stress state indicates that this question is nontrivial and the results potentially place important and demanding constraints on the origin of the asymmetry.

The goals in this work are to explore experimentally the flow structures associated with obstructed viscoplastic flow in a Hele-Shaw cell, and to investigate the existence and possible origins of any fore-aft asymmetry. The approach is to directly visualize the flow patterns and stagnant regions developing around obstacles embedded in a slot. Specific attention is paid to determine the position and size of static yielding surfaces around the obstacles. We explore the flow of a simple yield stress fluid, Carbopol, around isolated obstacles with different shapes. In addition, we consider the effect of hydrodynamic interactions of the obstacles by examining the flow around two obstacles placed in the slot at different orientations. To provide a more detailed theoretical comparison to these experimental results, we general-

ize the theory of [8] to a Herschel-Bulkley fluid and perform further computations<sup>2</sup>.

An outline of this chapter is as follows. The preparation procedure and rheological properties of the Carbopol solutions used in experiments are described in Sec. 3.2. The experimental method is outlined in Sec. 3.3. It includes a detailed description of the experimental setup and procedure. Our main experimental results and a comparison with the theoretical predictions are presented in Sec. 3.4. The flow pattern and plug regions developing around the obstacles with different shapes and orientations as well as a quantitative analysis of the size of the static unyielded regions are reported in this section. The chapter closes with a discussion of the main findings and our understanding of the origin of complexities observed in the experiments.

## 3.2 Fluids characterisation

Aqueous suspensions of Carbopol 940 with weight concentration of 0.055%, 0.06%, and 0.075% have been used as yield stress fluids in our study. Each sample of Carbopol solution has been prepared as follows. First, Carbopol powder was dispersed in five litres of distilled water. The mixture was stirred gently with a propeller mixer until the Carbopol powder was dissolved homogenously. Adding the Carbopol powder to the water causes the release of  $H^+$  ions and decrease in the  $pH$  of the solution. Then, 5% aqueous sodium hydroxide ( $NaOH$ ) was added to the solution gently in order to bring its  $pH$  to a neutral value. Then, the solution was mixed for 48 hours at low mixing rates, i.e. 200 *rpm* for 0.055% and 0.06% Carbopol as well as 300 *rpm* for 0.075% Carbopol. Finally, the solution was kept at rest for around 12 hours and its final  $pH$ -value was measured with a commercial  $pH$ -meter.

For flow visualization, red fluorescent polystyrene beads (fluorescent microspheres, Magspheres) with the mean diameter of 2.9  $\mu m$  were used as flow tracer particles. Fluorescent beads were dispersed in the fluids with volume fraction of 0.005%. Samples were sonicated in water to disrupt aggregates and achieve uniform disper-

---

<sup>2</sup>The theoretical formulation of the problem was explained in Sec. 2.3.

sion. Prior to each test, the samples have been centrifuged at 1000 rpm for two minutes in order to remove the air bubbles entrapped into the gel during the preparation process.

The rheological parameters of the fluids have been measured using a rotational rheometer setup (MCR501, Anton Paar) with the angular resolution of  $0.01\ \mu\text{rad}$  and torque resolution of  $0.1\ \text{nNm}$ . A parallel plate geometry with the diameter of  $50\ \text{mm}$  has been used for rheological measurements. In order to minimize the effect of wall-slip on the rheological measurements of the yield-stress fluids,  $46\ \mu\text{m}$  roughness sand paper was glued on the surface of parallel-plates. The gap thickness between the parallel plates was fixed to be  $1\ \text{mm}$  and the temperature kept constant at room temperature ( $22^\circ\text{C}$ ).

A series of shear stress controlled tests for the stresses in the range of  $0.001$  to  $10\ \text{Pa}$  have been done to determine the macroscopic flow curves of the Carbopol gels. Before starting the tests, the sample was pre-sheared at the highest shear rate in the flow curve for  $10\ \text{s}$  followed by a  $90\ \text{s}$  resting period. Then, the rheological experiment has been started with an increasing shear-stress ramp and ended with a decreasing shear-stress ramp within the same stress range and steps. The increasing-decreasing ramp has been repeated without delay for two times. Both ramp-up and ramp-down tests have been performed at the ramp rate of  $0.05\ \text{Pa/s}$ .

The increasing and decreasing stress parts of the flow curves obtained for three Carbopol gels used in our experiments are shown in Fig. 3.2(a). These fluids were well described by the Herschel–Bulkley constitutive law and showed little sign of hysteresis in their measured flow curves above the yield stress. Near that threshold, the flow curves display the hysteresis commonly found when performing controlled ramps in shear stress, an effect attributable to elastic deformation [29, 32]. The flow-curve data in Fig. 3.2(a) suggest that the fluids do not display any thixotropy of the kind previously found for other Carbopol gels [43, 44]. Beside this, we expect that the possible slight thixotropic behaviour of these materials does not play any noticeable role in our actual experiments; the fluid was pre-sheared before injection into the cell, to eliminate the initial non-ideal rheological effects reported

in sedimenting sphere experiments [60].

The Herschel–Bulkley fits of the yield stress,  $\tau_y$  (Pa), consistency,  $K$ , and power-law index,  $n$ , are summarized in table 3.1. Also listed are measurements of the shear storage and loss moduli,  $G'$  and  $G''$ , from small amplitude oscillatory rheometry;  $G'$  is somewhat larger than  $G''$  for all three fluids, suggesting a linear viscoelastic relaxation time below the yield stress that is less than a second [74]. This estimate for the relaxation time was consistent with additional stress relaxation tests and with previous rheometry of Carbopol gels with similar concentration [62].

The particular Carbopol solutions described above do not appear to exhibit discernible thixotropic behaviour. However, it was shown by Dinkgreve *et al.* [44] that the vigorous stirring of the gel during its preparation might lead to the significant thixotropic behaviour. Knowing this, it is interesting to examine the effect of time dependent behaviour of the thixotropic Carbopol gel on the flow configuration in the slot. Therefore, we prepared a different viscoplastic suspension by vigorously stirring 0.1% *wt/wt* Carbopol gel with a sharp blade at 1200 rpm for around two and a half minutes, motivated by previous observations of significant thixotropic behaviour arising from a similar method of preparation [44]. Our rheological measurements show that this new suspension does, indeed, exhibit appreciable thixotropic behaviour (Fig. 3.2(b); compare with the effectively non-thixotropic curves in Fig. 3.2(a)). The flow curves depicted in 3.2(b), were obtained from a shear rate ramp-up and ramp-down test after a pre-shearing of the material and a resting period. It should be mentioned that the waiting time for each point on the curves is 20 s. The Herschel–Bulkley parameters of the fluid are reported in Table 3.1 as well.

In addition to these Carbopol suspensions, we also conducted a small number of tests with two others fluids: a 31% *wt/wt* glycerol-water mixture and a 0.75% *wt/wt* polyethylene oxide (PEO) solution. The former provides a direct comparison with a Newtonian Hele-Shaw flow; the latter with a proto-typical viscoelastic liquid characterised by a relaxation time of a few seconds [75]. The PEO solution used in our experiments was prepared by dissolving 22.5 g of PEO powder (Sigma Aldrich,

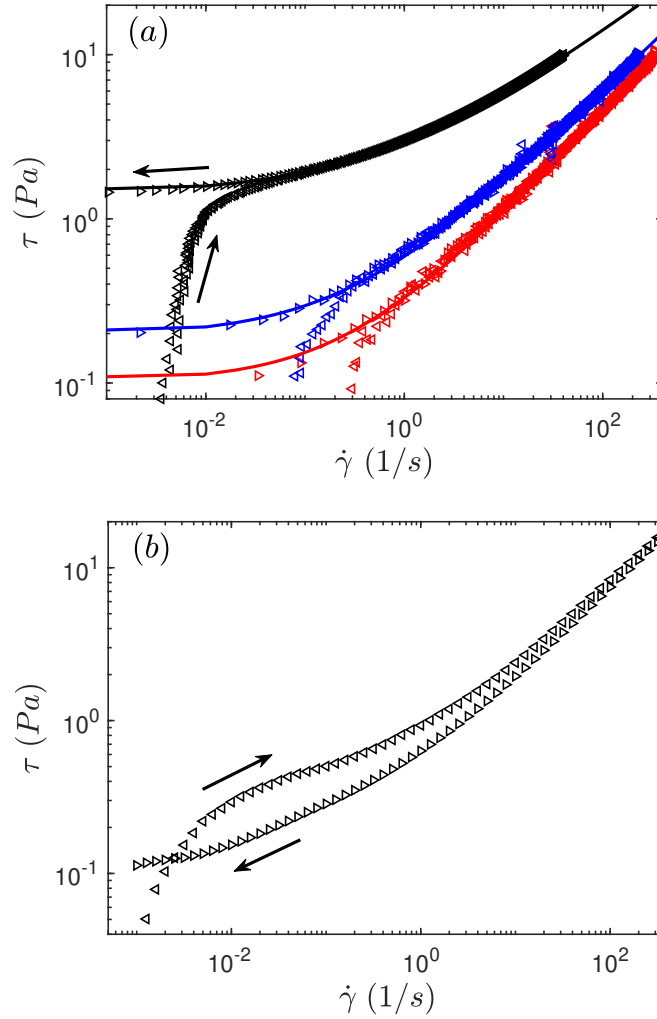


**Figure 3.2:** (a) Rheological curves for the three different Carbopol suspensions used in this work (0.075% (black), 0.06% (blue) and 0.055% (red)), from a shear-stress ramp up and then down in a roughened parallel-plate rheometer. There is no discernible thixotropic behaviour over most of the range of strain rate, and it is only at stresses very close to the yield stress that any rheological hysteresis is visible. (b) Rheological curves for an alternative Carbopol suspension (0.1%, very highly sheared during mixing) from a shear-rate ramp up and then down in a roughened parallel-plate rheometer, showing a very clear thixotropic signature over multiple decades of shear rate.

Material	Concentration (wt/wt %)	$\tau_Y$ (Pa)	K (Pa s <sup>n</sup> )	$n$	$G'$ (Pa)	$G''$ (Pa)
Carbopol	0.055	0.10	0.23	0.64	3.0	0.9
	0.060	0.20	0.39	0.57	4.2	0.7
	0.075	1.43	1.53	0.46	16	2.0
Highly-sheared Carbopol	0.10	0.10	0.44	0.61	—	—
PEO [75]	0.75	0	1.02	0.49	—	—

**Table 3.1:** Herschel-Bulkley fits of the non-Newtonian fluids used in our experiments including Carbopol solutions, and a PEO solution, with ( $R^2 > 0.99$ ). Also listed are shear storage and loss moduli ( $G'$  and  $G''$ ) for gently mixed Carbopol solutions. The dynamic measurements taken from small amplitude oscillatory rheometry at a frequency of 1 Hz and a strain amplitude of  $\gamma = 1\%$  (below which we confirmed that the two moduli were independent of  $\gamma$ ).

MW  $7 \times 10^6$ ) in 3 kg of water at room temperature. Then, the mixture was stirred by a propeller mixer for 72 hours to ensure that the homogeneous solution was obtained. The rheological parameters of the fluid is reported in Table 3.1.

### 3.3 Experimental method

The experimental setup includes an imaging unit, a horizontal channel, and a syringe pump. A schematic image of experimental setup as well as an image of the flow cell and obstacles are shown in Fig. 3.3. A swept-field laser-scanning confocal microscope which consists of a high-speed confocal scanner, four laser lines with different wavelengths, a high speed camera, as well as a high resolution motorized stage assembled with the inverted-type microscope was used for flow visualization at an imaging frequency of 30 Hz. All the components of the unit including detector, confocal and focus drive parts are synchronized through direct connections and can be controlled via software.

The confocal unit which contains scanner mirrors and aperture plane significantly improves lateral and axial resolution and decreases the depth of focus. The pinholes or slits on the aperture plane are positioned in the path of excitation and

emission beams to effectively eliminate the out of focus light. A 4X-objective lens with working distance of 16 mm and numerical aperture of 0.25 was used for imaging. A green laser beam (561 nm, 50 mW) was focalized by the objective lens on the observation plane in the cell to excite fluorescence of the tracing beads during the flow. The position of the observation plane was controlled by a motorized stage and fixed on the central horizontal plane of the cell. A 5.5 megapixel CCD-camera with the sensor size of 16.6 mm  $\times$  14 mm and maximum readout rate of 560 MHz was used to take images. Particle Image Velocimetry (PIV) is used to estimate the velocity field.

All results reported in this work were obtained in a thin rectangular channel, formed between two acrylic plates (of length  $L = 105$  mm and width  $W = 64$  mm) separated by a gap of height  $H = 1 (\pm 0.05)$  mm (see Fig. 3.1). The acrylic plates were fixed into an aluminium frame. The fluid is injected into the cell through four holes drilled on the top plate and leaves the cell through a perforation with a thickness of 4 mm and the same width of the channel that was machined in the top plate. A V-shaped vertical aluminium outlet port was screwed to the frame and connected to the outlet perforation on the upper plate, in order to smoothly drain the fluid out of the channel. The gap between the plates was formed by an aluminium spacer with thickness of 1 mm. At the injection points, the spacer was V-shaped to ensure uniform entry of fluid into the cell. The cell has been sealed by the O-rings placed in the grooves machined on the surface of the upper and lower acrylic sheets. The aluminium spacer and the O-ring have been sandwiched between the acrylic sheets by screwing the frame, spacer and sheets together.

From the theory, we know that even slight non-uniformity in the depth of the channel might significantly influence the flow pattern [8]. For this reason, the variation in the depth of channel has been measured using the confocal microscope, and we found at most a variation of 5%.

To place obstacles in the cell, we either drilled holes in the plates and inserted a cylinder, or 3D printed shapes with the thickness of the channel. The shapes, with cross-sections of a circle, square or stadium (each with a shortest cross-sectional



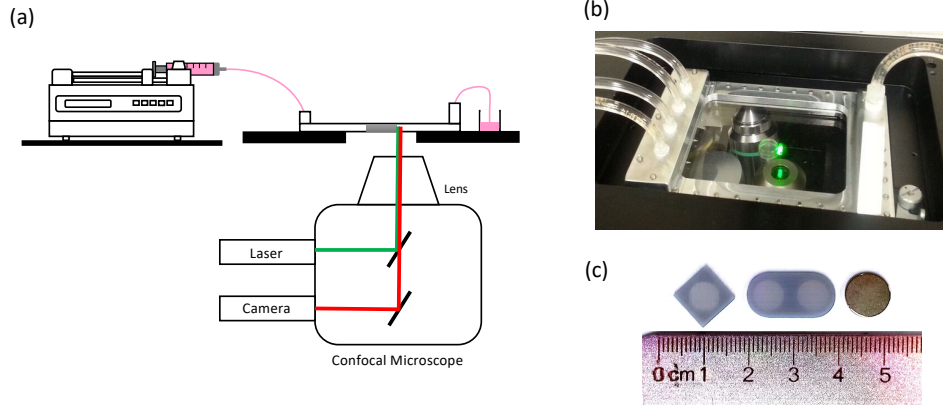


**Figure 3.3:** Overview of the experimental setup: (a) Sketch of the experimental setup including a swept-field confocal microscope, a flow cell, and a syringe pump. The path of excitation laser light (green) and that of emitted light from the fluorescent particles (red) are illustrated in this image. (b) Image of the flow cell mounted on the microscope stage. (c) Image of obstacles embedded in the channel.

length of  $D = 11 \pm 0.01$  mm), were printed with internal compartments to house a magnet, so that the obstacles could be suitably positioned and orientated inside the cell. The flow was generated by a syringe pump delivering a flow rate  $Q$  with a maximum of 3 mL/min (and providing inlet flow velocities of order  $10^{-4}$  m/s).

Each experiment was conducted by first cleaning the walls of the cell, using distilled water, followed by rinsing with methanol. In most cases with isolated disks, the walls were also chemically treated to reduce wall-slip, as described in Sec. 2.2.3. Carbopol was then pumped through the cell for approximately 20 minutes before flow-visualization commenced. Given the flow rate and rheological parameters, the Bingham number, which describes the dimensionless strength of the yield stress, is defined by

$$B = \tau_y K^{-1} (WH^2/Q)^n.$$

Because the field of view of the lens (2 mm  $\times$  2 mm) was too small to capture the whole cell, the full flow field was visualized by stitching together a series of

pictures to create a composite image (see Fig. 3.1(a)). This limitation had the drawback that we were only able to map the full flow field for a subset of the experiments, focussing on flow features at the front or back of the obstacles for the full set of tests. In order to create a composite image of full flow field, the system was programmed to precisely move the cell by a motorized stage to different positions around the obstacle. At each position, the flow of tracing particles was recorded. Then, the velocity data for each location were obtained by processing the images corresponding to it. Finally, the processed data regarding different locations were assembled together in order to prepare a large image of flow field around the obstacle. To perfectly stitch the data from different locations, a small percentage (20%) of pixels was set to overlap.

To verify the upstream flow condition, the transverse velocity profiles across the width of the channel (along  $y$ -axis, and at  $z = 0$ ) are measured at two different positions at the upstream of the channel, i.e.  $7.5\text{ mm}$ , and  $17.5\text{ mm}$  away from the inlet. The results confirm that the upstream velocity profile is effectively uniform along the lateral direction, and it is fully developed and not disturbed by the inflow in the channel and the obstacle (see Fig. 3.4(a)). Similar velocimetry measurements proved the well established and fully developed flow downstream of the cell as well (see further details in Appendix A (Sec. A.1)).

To verify the velocity profile across the cell, we undertook some separate studies of flow down a uniform slot with treated walls, combining optical coherent tomography (Thorlabs TEL1300V2-BU) with particle tracking velocimetry<sup>3</sup>. Sample profiles are presented in Fig. 3.4(b), together with theoretical predictions based on the prescribed flow rate and rheological parameters [8]. These results confirm the removal of any effective slip by the chemical treatment, and demonstrate how the theory and experiment are in quantitative agreement. By contrast, and in line with other studies [25, 76], Carbopol was observed to slip when the walls were untreated (see Fig. 3.4(b)). As illustrated Fig. 3.4(b), the slip velocity is relatively small (less than about 25% of the maximum velocity over the range of experimental parame-

---

<sup>3</sup>Details of the flow measurement technique used to characterise the velocity profile across the cell is explained in Sec. 4.4.

ters, as estimated by a linear extrapolation of the particle tracking data to the wall position) with the flow profile largely maintaining the same form as with treated plates.

A related concern was the potentially destructive impact on the wall treatment by the introduction and rearrangement of obstacles placed in the cell, which was achieved by moving magnets and involved dragging the obstacles over the tightly fitting walls. To avoid any possibility that mechanical contact might interfere with the surface treatment, when we explored flows around squares, stadia or multiple disks, we resorted to the use of cells with untreated walls, notably in reconstructing the full flow field (*cf.* Fig. 3.5). Before proceeding down this path, we did, however, verify that, for isolated cylinders inserted through drilled holes in the walls, there were no significant differences with results for flows down cells with treated walls (see Fig. 3.5(c) and the relevant discussion in Sec. 3.4.2).

## 3.4 Results

### 3.4.1 Plug phenomenology

Sample experimental results for cells with obstacles are presented in Fig. 3.5 while a selection of complementary numerical solutions are presented in Fig. 3.6. Figure 3.5(a) shows a control experiment in which a Newtonian fluid (a glycerol-water solution) was pumped around a disk. The flow pattern is fore-aft symmetric and compares well with the potential-flow solution also plotted.

The symmetry is preserved when test is repeated with the PEO solution (Fig. 3.5(b)). For the unconfined configuration, the flow pattern in such a fluid is expected to become asymmetrical owing to viscoelastic relaxation, which pushes the maximum shear stresses downstream of the top and bottom of the obstacle [65]. For the experiment shown in Fig. 3.5(b), one might expect that a similar relaxational effect arises and suppresses the plug in the wake. However, no asymmetry is observed for PEO, a result that extends to a range of flow rates and polymer concentrations. On further consideration [73], the absence of fore-aft asymmetry in this viscoelastic

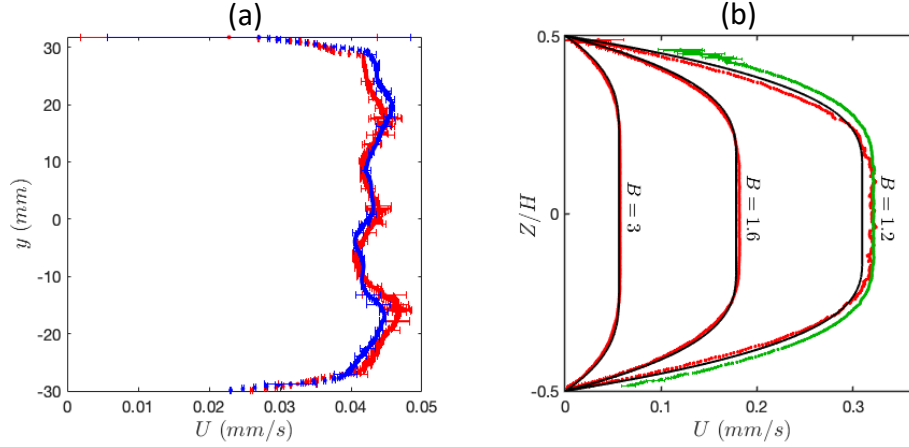


**Figure 3.4:** (a) Transverse velocity profiles obtained at the upstream of a Hele-Shaw cell containing an obstacle. The velocity profiles were experimentally measured along  $y$ -axis and at  $x = -45$  mm (blue) and  $x = -35$  mm (red), for 0.06% Carbopol and  $B = 3.1$ . Note that the entry of the flow cell is at  $x = -52.5$  mm. (b) Experimentally measured velocity profiles for 0.06% Carbopol in a uniform cell with chemically treated plates at the three Bingham numbers (flow rates) indicated (red). The solid black lines show corresponding theoretical predictions given the fluxes and the rheological parameters in Table 3.1. A profile from a cell with untreated plates for  $B = 1.2$  (green) is also shown.

flow is not surprising: for the sheared flow in the narrow geometry of our Hele-Shaw cell, the extensional stresses are suppressed and the Weissenberg number is relatively small (typical shear rates are  $0.1 \text{ s}^{-1}$ , in comparison to the  $O(1\text{s})$  relaxation time).

Fig. 3.5(c) shows the analogous experiment with Carbopol, which differs in two ways to the Newtonian and PEO tests. First, unyielded plugs spanning the cell appear at the front and rear of the disk, and this feature of the flow is mirrored in the theoretical solutions (Fig. 3.6(a)). In detail, however, the structures in the flow field, and in particular the dimensions and shapes of the experimental plugs, differ from their theoretical counterparts. Notably, the experimental plugs have a roughly right-angular form<sup>4</sup>, whereas their theoretical counterparts thin to a pro-

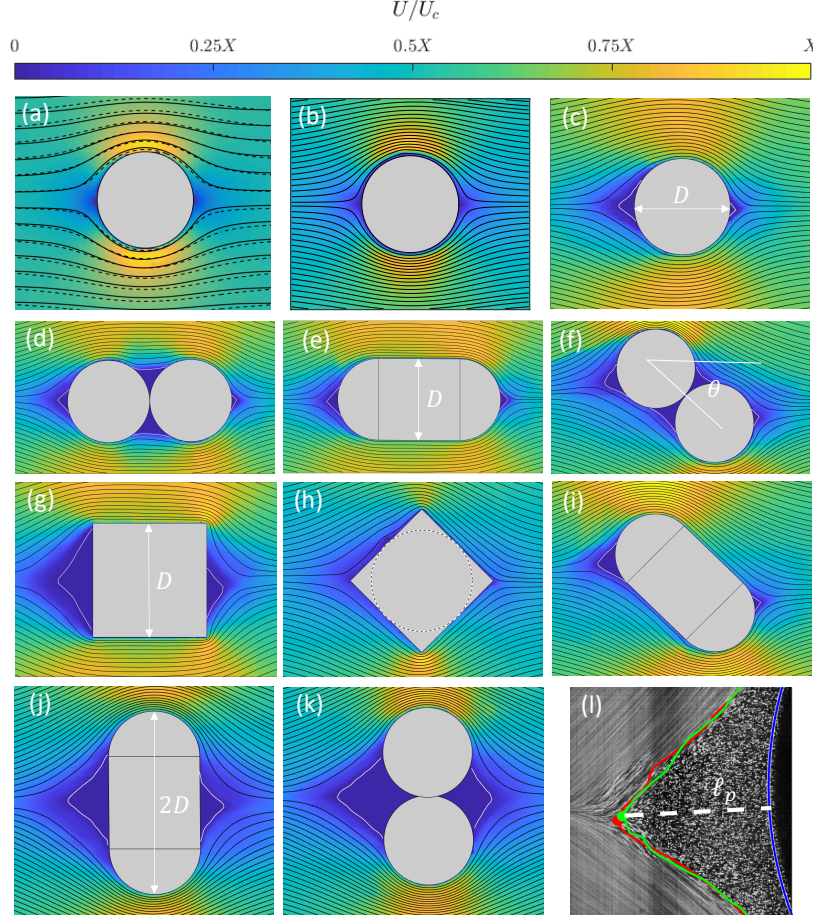
nounced cusp-like nose. This discrepancy may arise because the Hele–Shaw theory breaks down on lengthscales comparable to the height of the slot (here,  $H \sim 1$  mm, which is comparable in size to the discrepancy between theory and experiment) or by the complications in defining the edge of the plug due to undetectable velocities. Such possibilities cannot, however, rationalize the second difference between the Carbopol and earlier tests, which is that there is a marked fore-aft asymmetry in the flow pattern, with the plug at the front being larger than that at the rear, and mirrors findings for unconfined flows [60, 61].

Figure 3.5(d–k) show more experiments with different shapes or combinations of obstacles (all with the 0.06% Carbopol). Plugs again appear in almost all cases, except when the front or rear of the obstruction has the form of a relatively sharp corner (Fig. 3.5(h)). However, in every case the flow pattern displays a clear fore-aft asymmetry. Once again, there is some qualitative agreement with complementary theoretical results for different obstacles (see Fig. 3.6(b–f)). However, in every case the experimental flow patterns display a clear fore-aft asymmetry that is absent in the theoretical predictions. There are also quantitative differences with the theoretical predictions for the plugs that are again suggestive of inadequacies in the Hele–Shaw approximation (for example, there are small plugs at the front and back corners of the diamond-shaped obstacle in the computations, but not the experiments).

The limitation of the Hele–Shaw approximation is certainly responsible for the substantially faster flows that arise against the top and bottom of the obstacles in the theoretical solutions; see Fig. 3.7(a). In particular, in this approximation, fluid is permitted to slide along the boundary of the obstacle, whereas in reality any slip is either much reduced or eliminated entirely, depending on the degree of surface interaction. Consequently, to correct the theory a boundary layer of thickness  $H$  is needed that sheathes the obstacle and adjusts the surrounding velocity field to accommodate the true surface condition. The boundary layer is visible in all the

---

<sup>4</sup>It is worth mentioning that the quantitative analysis of the plugged regions developing around the obstacles confirm their quasi right triangular shape over a wide range of Bingham numbers. Details of experimental results corresponding to the plug shape is reported in Appendix A (see Sec. A.2).



**Figure 3.5:** PIV images showing speed, normalised by the incident speed  $U_c = Q/WH$ , and streamlines (all flowing left to right) along the midplane of the slot around various obstacles. (a) The flow around a disk for a glycerol-water solution (31 wt/wt%) at  $Q = 0.05$  mL/min; dashed lines show the corresponding potential-flow solution. (b) Flow field for a viscoelastic PEO solution (0.75 wt/wt%) with  $Q = 0.16$  mL/min. (c)–(k) Flow fields for a Carbopol solution (0.06 (wt/wt%), untreated walls) with  $B = 3.1$  (c,g,h) and  $B = 2.7$  (d,e,f,i,j,k). The upper limit of the colorbar was set at  $X = 2.8$  for (a,b),  $X = 2$  for (j,k), and  $X = 1.6$  for (c–i). (l) An average image near the plug at the front of a disk (0.075% Carbopol solution,  $B = 2.3$ , treated walls). The solid lines indicate the edge of the plug according to edge-detection (green) or a velocity threshold (red); the dashed line shows the estimated plug length  $\ell_p$ . White lines in (c–k) show the yield surfaces detected using a velocity threshold of  $0.0005$  mm/s.

experimental images of Fig. 3.5, as are the excessive high-speed regions in the solutions of Fig. 3.6. The maximum speeds attained in the theory are therefore too high in comparison to the experiments. In fact, as shown in Fig. 3.7, because the experimental slot is not that narrow ( $H/D \approx 0.1$ ), the high-speed regions predicted theoretically are almost completely smeared out, rendering the faster flows more distant and broader. Otherwise, the sections of speed across the slot shown in Fig. 3.7(b) compare fairly well between theory and experiment (modulo the fore-aft asymmetry in the latter).

Note that, for multiple disks and stadia, both the experiments and theoretical computations display a “cloaking” effect similar to that reported by [77]: when such obstacles are orientated broad-side on, the unyielded plugs at the front and back mask the precise differences in shape, such that the surrounding flow field becomes essentially the same (*cf* Fig.3.5(j) and (k), or Fig. 3.6(d) and (f)). Only when the yield stress (*i.e.*  $B$ ) is sufficiently small do the plugs fail to cloak the front or back surface, unveiling the true shape differences. (This feature is seen particularly clearly in the theoretical plots of Fig. 3.9(a) below). If the broad side of the obstacles is orientated either with the flow or at  $45^\circ$ , no such cloaking effect is possible as the surface of the obstacle is always exposed to unyielded fluid. Nevertheless, in the Hele-Shaw geometry, the yield surface of the plugged-up cavity for the double disks acts somewhat like the straight sides of the stadium, shielding the surrounding flows and rendering similar their patterns (compare panels (d) and (e), or (f) and (i), of Fig.3.5).

The Carbopol experiments also display weak symmetry-breaking in the direction transverse to the flow for obstacles with a symmetry plane along the midline of the cell (*i.e.* up-down symmetry in Fig. 3.5; *cf.* the magnification of the forward plug in Fig. 3.5(l) and the speed sections in Fig. 3.7). We interpret the broken symmetry to arise from imperfections in the cell geometry and inflow, which apparently become accentuated by the yield stress of the fluid (neither the Newtonian nor viscoelastic experiments were noticeably asymmetrical). These imperfections are not systematic from experiment to experiment, and separate velocimetry measurements across the slot upstream of the obstacle indicate that the incident flow is

fully developed.

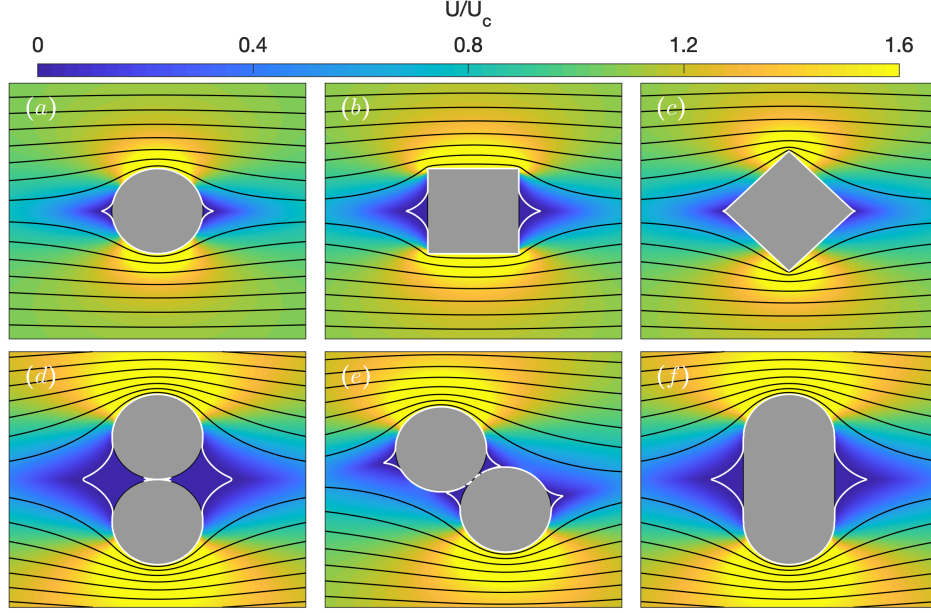


**Figure 3.6:** Speed (shading; scaled by the incident speed  $U_c$ ) and representative streamlines (solid black lines) along the midplane of the slot for computations of Herschel-Bulkley fluid around the grey-shaded obstacles, for  $n = \frac{1}{2}$  and  $B = 4$ . The range of the colorbar matches that used in Fig. 3.5(c)–(k). The white lines show yield surfaces, given by the threshold  $U/U_c = 1 \times 10^{-3}$ .

### 3.4.2 Plug lengths

To quantify the plug size for the bluff obstacles, we measure the perpendicular distance  $\ell_p$  from the apex of the triangular plug to the obstacle surface; see Fig. 3.5(l). This measure is unambiguous and convenient for all but the double disks aligned perpendicular to the flow in Fig. 3.5(k); for those, we define  $\ell_p$  as the shortest distance from the apex of the plug to the vertical line drawn between the frontmost or rearmost points of the disks. The plug itself is identified either from edge detection in the average of the images recorded (in which stationary tracer particles appear as bright points whereas moving tracers become blurred into grey streaks), or from



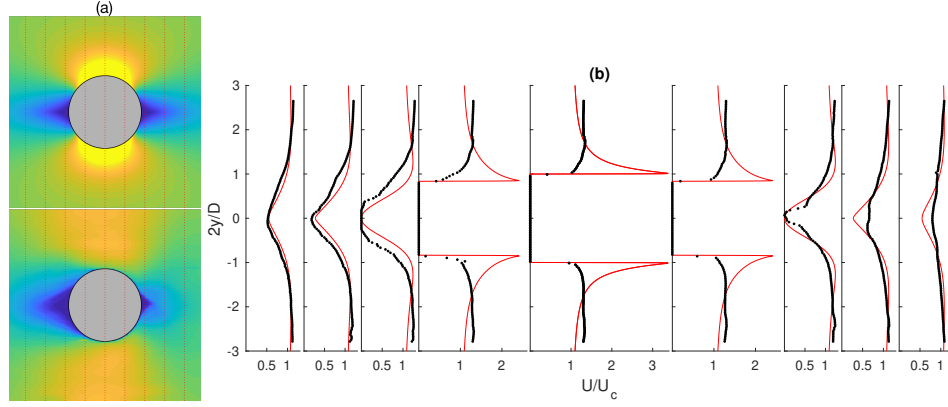


**Figure 3.7:** (a) Scaled theoretical (top) and experimental (bottom) speeds,  $U/U_c$ , for flow around a disk with  $n = 0.57$  and  $B = 2.3$ , corresponding to panel (l) in Fig. 3.5 (and using the same scheme for the colormap as that figure). In (b), the theoretical (solid lines) and PIV (dots) speeds are plotted along the sections indicated by the vertical dotted lines in (a).

a noise-based threshold in the velocimetry. The two methods give comparable results (see Fig. 3.5(l)).

A systematic survey of plug length as a function of Carbopol concentration, inlet flow rate, and blockage configuration is shown in Fig. 3.8, with analogous theoretical computations shown in Fig. 3.9. All the experimental results for disks, squares and stadia, spanning roughly two decades of Bingham number ( $0.1 \leq B \leq 10$ ), are assembled in Fig. 3.8(a). The fore-aft asymmetry is very clear in these results, with the plug lengths roughly fall into three groups. In particular, the plug lengths for single disks are similar to those of two disks or stadia that are either aligned with or at  $45^\circ$  to the flow. The plug lengths for double disks or for a stadium aligned perpendicular to the flow are somewhat different, but are similar to one another. The square is different again, with a plug length somewhere between those of the other two groups. Although there is no fore-aft asymmetry in the theory, the plug-length data do again fall into the same three groups, with the computations otherwise qualitatively capturing the trend of the experimental measurements. More quantitatively, the prediction of the plug length is somewhat low, curiously aligning more with the data for the rear plugs than those at the front (see Fig. 3.8(b)).

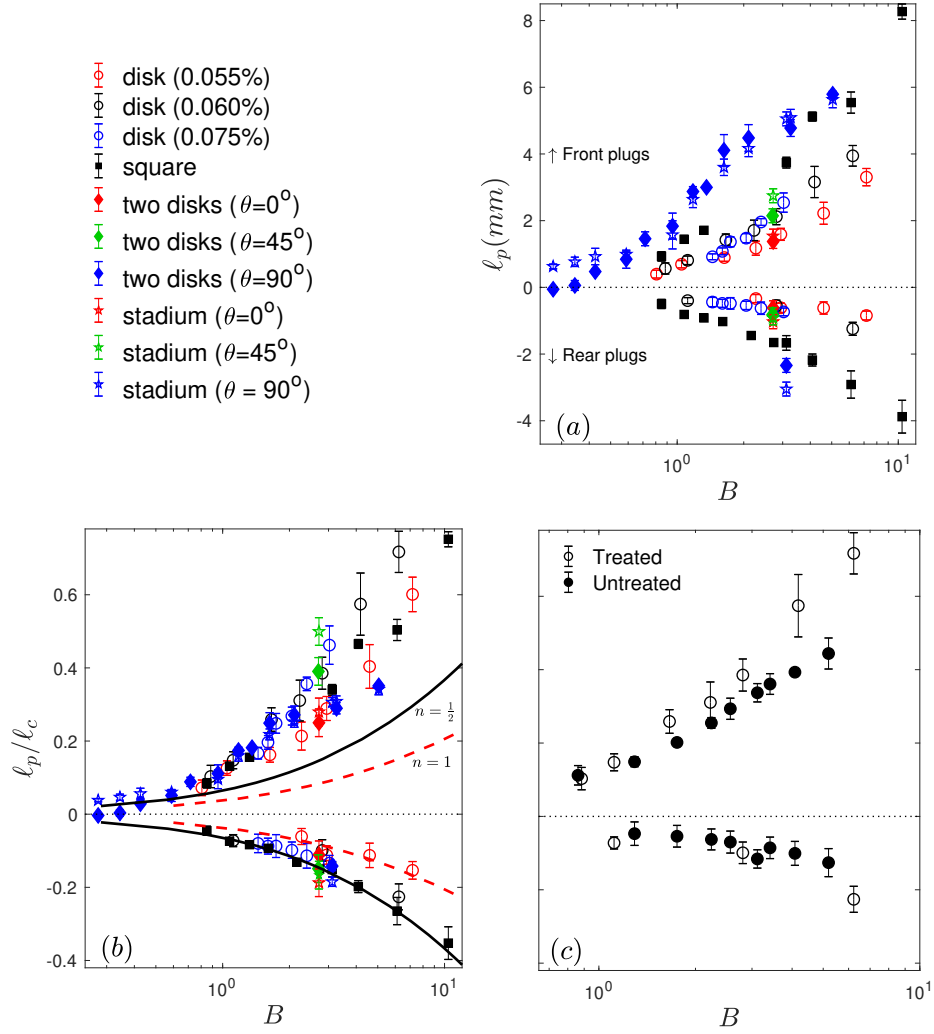


**Figure 3.8:** (a) Dimensional plug lengths  $\ell_p$  of the configurations shown in Fig 3.5, with the conventions indicated by the legend. The walls of the cell are treated to remove slip for the isolated disks, but for the squares, stadia and multiple disks, the walls are untreated in view of the potentially destructive method of insertion or rearrangement. (b) Scaled plug lengths  $\ell_p/\ell_c$ , where  $\ell_c$  is chosen as indicated in the main text for the three groupings of obstacles. The lines show theoretical results for isolated disks, calculated using the numerical method of [8] for the Herschel-Bulkley model with  $n = 0.5$  (black solid) and  $n = 1$  (red dashed). (c) A comparison of the plug size for flow of 0.06% Carbopol around disks with treated and untreated acrylic sheets. In all three panels, we plot  $\ell_p$  as positive for the plugs at the front, and  $\ell_p < 0$  for those at the back. The error bars indicate the standard deviation from three repetitions of each experiment.

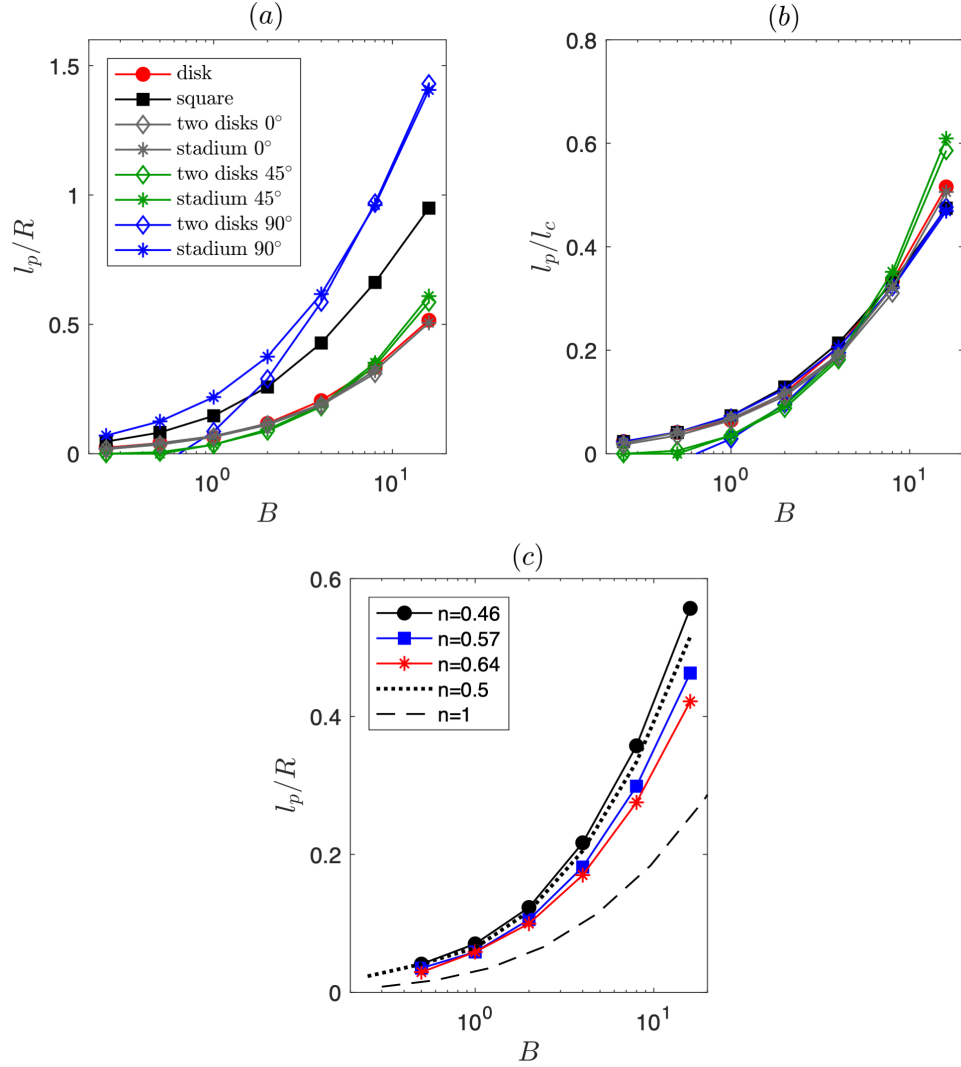


**Figure 3.9:** Theoretical predictions of the plug lengths from numerical simulations for the obstacle arrangements indicated by the legends, and following the experimental results in figure 3.8, showing (a)  $\ell_p/R$  and (b)  $\ell_p/\ell_c$ . These computations have  $n = \frac{1}{2}$ ; in (c) data are shown for isolated disks and the three values of  $n$  for the experimental fluids, as well as results for  $n = \frac{1}{2}$  and for a Bingham fluid ( $n = 1$ ) [8], for reference.

We achieve some collapse of the data by scaling the plug length according to a simple algorithm, which crudely identifies the length of the obstacle over which the incident flow forms an angle greater than  $45^\circ$ : for obstacles with rounded leading or trailing faces (Fig 3.5(c)-(f),(i)) we scale  $\ell_p$  with the radius of curvature of the front or rear; *i.e.*  $\ell_c = R \equiv D/2$ . For obstacles with a square front or rear face, we scale  $\ell_p$  by the length of that face; for the square obstacle in Fig 3.5(g); this corresponds to a scaling of  $\ell_c = 2R$ . For double disks and stadia aligned perpendicular to the flow (Fig 3.5(j)-(k)), we compose a scaling length from the radius of curvature of the top and bottom of the obstacle plus the square length of the section inbetween; *i.e.*  $\ell_c = 3R$ . Fig. 3.8(b) shows the scaled plug lengths,  $\ell_p/\ell_c$ . The success of the collapse is reinforced by Fig. 3.9(b), which performs the same scaling of the theoretical results. The simple algorithm also rationalizes the lack of plugs in the tilted square in Fig. 3.5(h), where no part of the obstacle is sufficiently inclined against the incident flow.

Note that there is little systematic difference in the results for isolated disks between the three different Carbopol suspensions when plotted against the Bingham number, which suggests that any dependence on the power-law index  $n$  of the non-linear plastic viscosity is relatively weak over the range of experimental conditions (in particular at low Bingham numbers). This feature is shared by the theoretical computations, which also display a weak dependence on the power-law index  $n$  (Fig. 3.9(c)).

Finally, we report the results of experiments for a single disk in a cell with untreated plates and a range of flow speeds to examine the importance of effective slip. Poumaere et al. [25] have previously suggested that wall slip can create complexity in the flow dynamics down narrow conduits. As illustrated in Fig. 3.8(c), although there is a small quantitative effect on plug lengths, the degree of fore-aft asymmetry remains unchanged, implying that surface interaction is not the cause of this asymmetry, and that wall slip does not appear to introduce qualitatively

different flow dynamics in our Hele–Shaw cells<sup>5</sup>.

### 3.4.3 Constraining the origin of asymmetry

The salient feature of our results is the marked fore-aft asymmetry in the plug regions and flow patterns developing around the obstacles that merits more explanation. To further constrain the origin of the fore-aft asymmetry, we conducted some additional tests which are explained as follows.

#### Steady flow around two disks aligned with the flow direction

First, we examined steady flow around two disks aligned with the flow, but with varying separations (Fig. 3.10). The varying separation implies that fluid elements progress along Lagrangian trajectories of different lengths as they deflect around the disks, such that any rheological evolution of fluid elements should be reflected in differences in the overall flow pattern. An increase in the separation distance between the disks leads to no observable effect on either the length of the plug at the front of the first disk or on that at the rear of the second disk. Furthermore, once the intervening distance between the plugs is sufficiently long that the stagnant plug bridging the gap has broken up, the front and rear plugs of the second disk are essentially the same length as those of the first. These observations limit the rheological changes that must occur along the streamlines to those that occur over distances of order the diameter of the disks. That is, the distance between the top of the disk and its front or back, which is a few millimetres and corresponds to a typical transit time of ten or so seconds, given that typical inlet flow speeds are order  $10^{-4}$  m/s.

Despite this, the data in Fig. 3.10 demonstrate that the plug bridging the gap can be longer than the combined length of the plugs at the front and back of an isolated disk. The leading obstacle does therefore cast a shadow on its follower,

---

<sup>5</sup>Note that all the experiments reported in this chapter were done with obstacles with quite smooth edges. In order to examine the effect of slip-condition at the edge of the obstacle, we performed a few tests with a disk with rough edge. The results indicate qualitatively similar fore-aft asymmetrical flow patterns around the obstacles with smooth and rough edges, although there is a slight increase in the length of the rear plug in case that the rough disk is used. See Appendix A for further details (Sec. A.3).

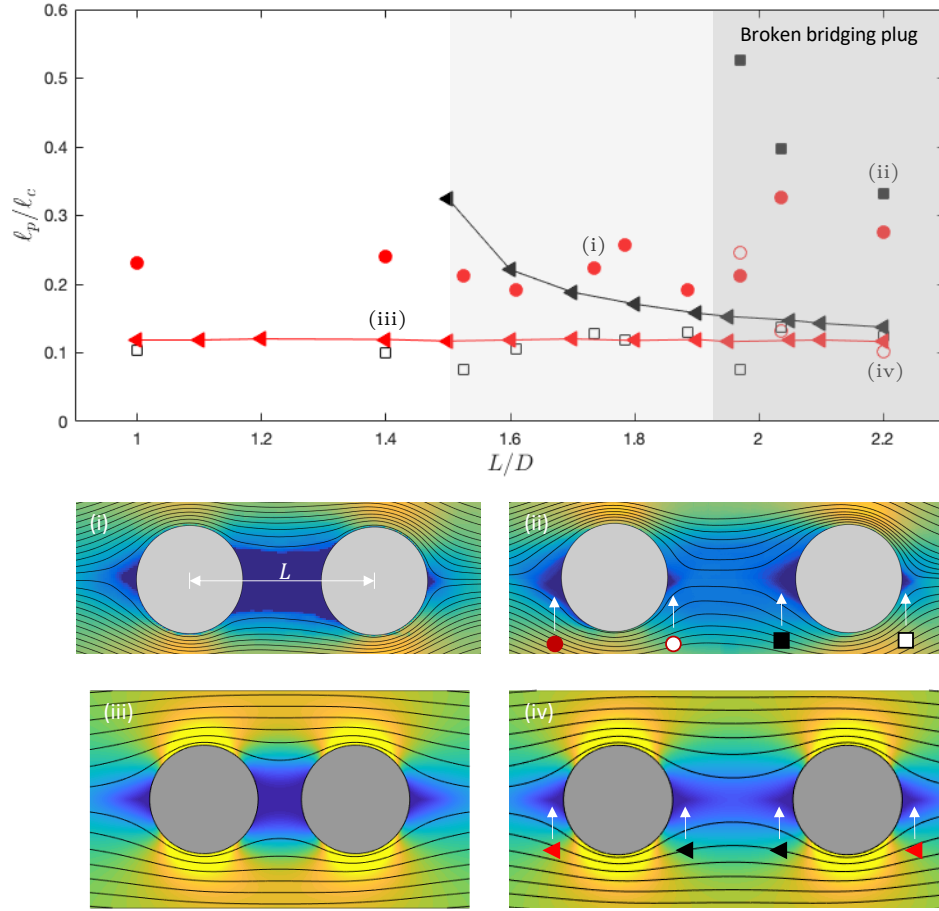


**Figure 3.10:** Plug lengths for two disks aligned with the flow as a function of the centre-to-centre separation  $L$ , for experiments with untreated sheets and numerical computations;  $B = 2.7$  and  $n = 0.57$  (0.06% Carbopol). The images (i)–(iv) below correspond to the separations identified in the main panel, with the symbols corresponding to the plug locations indicated, and show scaled speed maps (with colorbars as in Fig. 3.5, where  $X = 1.6$ ) and streamlines. Given the lack of any apparent trend with  $L$ , the scatter in the experimental data for the leading plug length (filled red circles), with a standard deviation of about 15%, gives a sense of the overall uncertainty in the measurements.

which leads to a slight increase in the length of the front plug attached to that second obstacle just after the bridge is broken. These more quantitative details of the flow adjustments induced by the interaction of the obstacles are obscured by the scatter in the experimental measurements, but are more clearly identified in theoretical computations, even though the fore-aft asymmetry is lost (see Fig. 3.10). Note that such interactions are very different from those occurring in unbounded flows around cylinders, where the yielded regions are localized to the obstacles and the surrounding plugs can sometimes (though not always) suppress any interaction [78]<sup>6</sup>.

### **Time-dependent flow around an isolated obstacle**

Next, we conducted tests designed to constrain, in a different way, any microstructural ageing or relaxation: for the flow around an isolated disk, we varied the inlet flux  $Q$  in a step-wise fashion over time, and extracted the time-dependent plug length at the front of the disk. As seen in Fig. 3.11, this length adopts its steady value after an undetectably rapid adjustment to the switch in flow rate. We repeated this test using a number of different protocols to increase or decrease the flow rate and found similar results (see Fig. 3.12). Thus, the characteristic relaxation time for rheological changes must be less than about ten seconds, the interrogation time for determining the plug size. This is consistent with both the lack of any larger-scale asymmetry in the flow patterns around separated disks, and the absence of any noticeable hysteresis above the yield stress in the up-down flow curves of Fig 3.2(a).

### **Flow of a thixotropic Carbopol solution around an isolated obstacle**

To emphasize this last point, we used a different viscoplastic suspension, highly-sheared 0.1% *wt/wt* Carbopol with significant thixotropic behaviour. As described before in Sec. 3.2, flow curves measured for this suspension did, indeed, exhibit

---

<sup>6</sup>We also performed a series of experiments to investigate the hydrodynamic interaction of obstacles oriented perpendicular to the flow direction. In accordance with the theoretical findings [8], our experiments confirm that the hydrodynamic interactions of obstacles have minor effects on the flow pattern and size of plug regions, when the disks are arranged perpendicular to the flow. The details of experimental findings for this orientation are reported in Appendix A (see Sec. A.4).

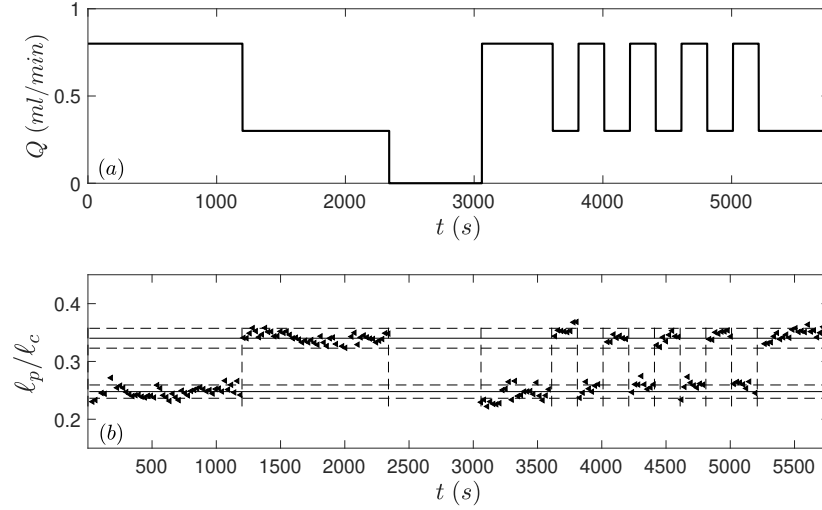


**Figure 3.11:** Time dependency of the plug size on the front and back of an isolated disk subject to a flowrate  $Q(t)$ . The tests were performed with 0.06% carbopol solution and treated sheets. The solid and dashed horizontal lines represent the average and standard deviation of steady state value reported in Fig 3.8(b).

significant hysteresis (Fig. 3.2(b)). With this second type of Carbopol in the obstructed Hele-Shaw cell, the flow patterns were still fore-aft asymmetric and the plug lengths were strongly time-dependent after step changes in flow rate (Fig. 3.13). In fact, experiments with this fluid were generally unreproducible and depended on the stress history of the fluid, in clear contrast to the main results reported in this chapter. To confirm this point and make a clear distinction between the obstructed flows of a simple and a thixotropic viscoplastic fluid in a Hele-Shaw cell, we performed a number of additional experiments with Laponite, which is typically known as a thixotropic yield stress fluid. The results are found in Appendix A (see Sec. A.5).

### 3.5 Conclusion

In this chapter, we have provided an experimental study of the flow of a yield-stress fluid around obstructions in a thin slot. We also complemented these experiments with theoretical computations that generalize our previous analysis of flows



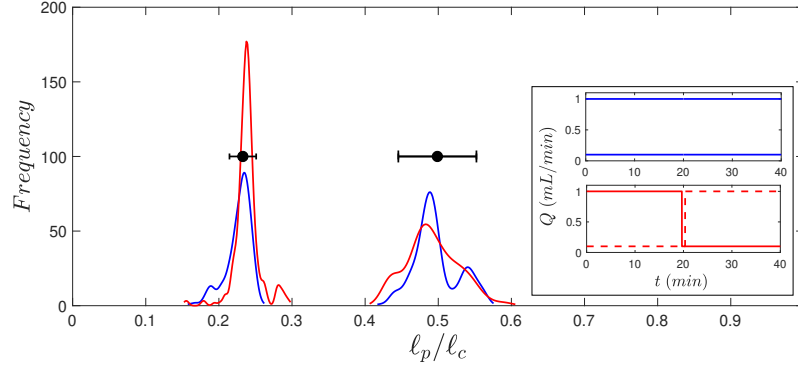


**Figure 3.12:** Distribution of normalized plug length measured during two steady tests (blue) and two unsteady tests (red). The inset indicates the diagram of flow rate by time during steady and unsteady tests. The results are reported for the length of plug region developing in the front of an isolated disk subjected to the flow of 0.06% Carbopol solution. The tests were conducted with treated sheets. The black dots and solid horizontal lines represent the average and standard deviation of steady state value for the plug lengths from Fig 3.8(b). Comparison between the results obtained from steady and unsteady tests does not show any signature of shear history dependence of the plug length.

of Bingham fluid in Hele-Shaw cells [8]. Both the experiments and theory demonstrate the appearance of stagnant plugs spanning the slot attached to the front and back of the obstacles, together with high-speed flows to either side. A number of trends observed in the experiments are successfully predicted by the theory. However, the experiments are strikingly different from the theoretical predictions in the fore-aft asymmetry of both the flow field and the size of the unyielded plugs. The asymmetry is not present in experiments with either a Newtonian fluid or, unlike in an unconfined geometry, a simple viscoelastic fluid. We find that the asymmetry is insensitive to effective slip over the walls of the slot, and must be connected to some sort of rheological hysteresis of the Carbopol suspension that was used. The experiments suggest that the hysteresis arises over flow distances of a few millimetres given the typical flow rates through the cell ( $O(10^{-4})$  m/s), which translates to relaxation times of ten or so seconds.

Carbopol suspensions have been observed to possess non-ideal rheology in pre-

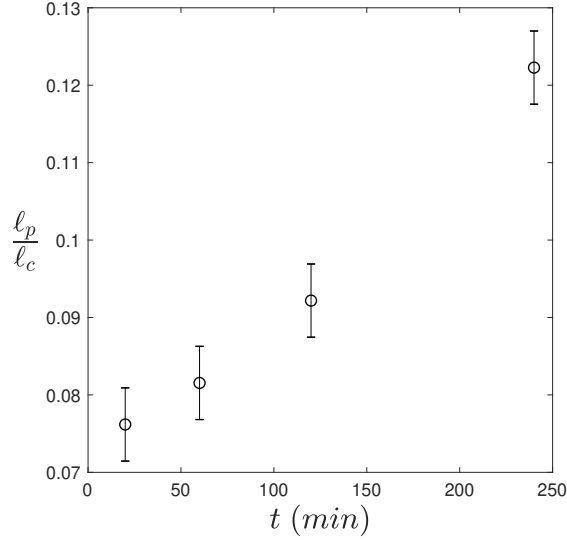


**Figure 3.13:** Time series of the plug length after a step change in flow rate behind a circular obstruction in the Hele-Shaw cell using the highly-sheared 0.1%-Carbopol (with flow rate  $Q = 0.05$  ml/min after the step change). Thixotropic flow curve of the material is reported in 3.2(b).

vious studies, either close to the yield stress or across a wider range of shear rates [33, 43, 44, 60]. Indeed, when we prepared a different suspension of Carbopol by vigorous mixing (Fig. 3.2(b) and Fig. 3.13), a pronounced thixotropy arose that significantly affected the flow patterns observed in the Hele-Shaw cell. However, the Carbopol that we used in most of our experiments exhibited no discernible hysteresis above the yield stress (Fig. 3.2(a)), while still showing strong fore-aft asymmetry.

A key detail of viscoplastic flow in a Hele-Shaw cell is the flow structure across the gap: the yield stress establishes shear layers against the walls of the cell which border a central plug-like flow spanning the midplane of the slot (Fig. 3.1). Material inside that pseudo-plug region is held slightly above the yield stress in order to accommodate the weak extension or shearing in the plane of the cell that permits flow around an obstruction [8, 29]. This feature aside, strain rates and stresses in

the plane of the cell are less significant than the shear rates and stresses across it. A significant fraction of the fluid across the slot is therefore always close to its yield stress throughout the quasi-two-dimensional flow pattern. Indeed, the thickness of the pseudo-plug at any point is dictated by the local shear stresses across the slot, which can be directly inferred from the midplane velocity. The measurements in Fig. 3.5 imply that the pseudo-plug thickens as fluid approaches the front of an obstacle, then thins more substantially as the material is swept through the high-speed regions at the top and bottom of the obstacle, before thickening once more in the wake. The pronounced fore-aft asymmetry observed in our flow patterns most plausibly arises either from relaxation over the shear layers or from hysteresis near the yield stress, which becomes embedded in the erosion or growth of the pseudo-plug and affects the macroscopic flow patterns. The lack of any noticeable hysteresis *above* the yield stress in the flow curves of the Carbopol suggests that relaxation over the shear layers is not responsible. However, further rheological work is required to identify the precise origin.

## Chapter 4

# Characterising wall-slip behaviour of Carbopol gels in a fully-developed Poiseuille flow<sup>1</sup>

### 4.1 Introduction

Concentrated dispersions including microgel pastes, granular suspensions and emulsions which exhibit viscoplastic behaviour, can be found in a wide variety of geophysical and industrial settings ranging from plumbing of mud volcanos to the recovery of oil [29]. The plasticity of these materials originates from their closed-packed amorphous structure that allows them to flow only if a stress greater than their yield stress is applied [80, 81]. Indeed, the motion of these materials is not only a function of their bulk flow properties, but also dependent on the interactions with the solid boundaries [29, 31]. In practice, viscoplastic fluids, like many other complex fluids, exhibit slip on the bounding walls, which significantly complicates their internal flow along thin conduits [23–25, 58]. The noticeable effect of the wall slip on the flow configuration of yield-stress fluids reveals the necessity of studying their slip mechanism.<sup>2</sup> The present study is designed to characterise the

---

<sup>1</sup>A version of this chapter was published in *Journal of non-Newtonian Fluids Mechanics* [76], and extracts of that research appeared in [79].

<sup>2</sup>For more details see Appendix B.

slip behaviour of Carbopol gels, which are dispersions of soft particles. Carbopol solutions have been used in a wide range of rheological and hydrodynamic studies as a widely accepted model yield-stress fluid because of their optical transparency, stability in time, as well as insignificant thixotropy and aging behaviour [50, 82–84].

Slip behaviour is often attributed to the migration of the disperse phase away from the bounding surfaces. Migration leads to the formation of a layer of solvent near the wall and is commonly related to the apparent slip layer [46]. In the case of yield-stress fluids made of soft particles, it is assumed that the elastic deformation of the particles against the wall leads to the creation of the lubrication layer. The thickness of this layer is dictated by the balance between the osmotic force of the suspension, the lubrication force caused by relative motion of shearing surfaces and particles, and the surface forces [18, 19, 22]. In addition, Seth *et al.* [19, 22] found a sliding threshold below which the particles attach to the surface, by examining the steady torsional flow of gels on adhering surfaces. The sliding threshold which is known as the sliding yield stress,  $\tau_{SY}$ , is smaller than the yield stress of the material,  $\tau_Y$ . The slip velocity can be related to the excess wall shear stress, i.e. the wall shear stress ( $\tau_w$ ) minus the sliding yield stress ( $\tau_{SY}$ ), by the following equation,

$$U_s = \beta(\tau_w - \tau_{SY})^p \quad (4.1)$$

where the prefactor,  $\beta$ , and exponent,  $p$ , were characterised for different ranges of wall shear stresses and different geometries in the literature. Meeker *et al.* [18] and Seth *et al.* [19, 22] studied the wall slip of microgel pastes in a steady torsional flow using optical rheometry. They suggested that the exponent,  $p$ , is a function of surface chemistry and its interaction with particles but does not vary with the concentration of gels over both the fully plugged regime, i.e.  $\tau_w < \tau_Y$ , and the deformation regime, i.e.  $\tau_w > \tau_Y$ .

For weakly adhering surfaces, the slip velocity changes by a quadratic scaling law over the fully plugged regime [18, 19, 22]. Moreover, below the yielding point, the prefactor is related to the microstructure of the fluid in terms of its elastic modulus,

$G_0$ , and the radius of the particles,  $R_p$ , as well as the viscosity of the solvent,  $\eta_s$ , by  $\beta \sim G_0 R_p / \eta_s$  [18]. Meeker *et al.* [18] and Seth *et al.* [19] showed that their phenomenological model for the wall-slip velocity of microgel pastes on the weakly adhering surfaces can be explained using the theory of elastohydrodynamic lubrication between soft particles and the wall. According to this theory, the thickness of the lubrication layer is set by the balance between the elastic and the viscous forces and hence varies with the slip velocity. Note that the attractive force contribution is only influential for very thin gaps, and does not affect the flow at moderate velocities.

Seth *et al.* [19, 22] examined slip velocity for the repulsive surfaces as well and indicated that for weak flows and where the repulsion dominates, the thickness of the slip layer is set by the surface forces and is not sensitive to the flow hydrodynamics. Hence, the slip velocity in this regime changes linearly with the excess shear stress. Seth *et al.* [19] showed that these results can be explained by the theoretical model developed based on hydrodynamic lubrication of soft particles under the effect of strong short-range repulsive forces. Note that for faster flows, the wall-slip is dominated by elastohydrodynamics and similar to the case of weakly adhering surfaces, the slip velocity varies quadratically with the wall-shear stress [19, 22].

Above the yielding point, the physical picture of the wall slip is more complex and the prefactor cannot be described as a function of microstructure of the fluid. Nevertheless, regardless of the surface chemistry, the slip velocity changes linearly with the wall-shear stress in this regime. It can be described by the hypothesis that above the yielding point the thickness of the slip layer is constant and proportional to the distortion of the particles, i.e.  $\gamma_Y R_p$ , where  $\gamma_Y$  is the yield strain [22].

Recently, exploiting flow visualization devices integrated with a capillary viscometer, the wall-slip behaviour of microgel pastes have been examined in pressure driven flows. However, there are discrepancies between the models reported in the literature for wall-slip behaviour of Carbopol gels with different concentrations in the Poiseuille flow. In particular, different values have been reported for

the exponent of the scaling law for Carbopol gels with various concentrations in different studies; i.e.  $0.87 < p < 2$ , over both the fully plugged and deformation regimes [23–26]. These studies have been performed for a fixed surface chemistry (with flow cells made of glass). Gonzalez *et al.* [23] and Aktas *et al.* [24] studied the capillary flow of 0.2% (wt/wt) Carbopol solution and delineated that the slip velocity increases with the wall shear stress through a power-law model, i.e.  $U_s \sim \tau_w^{0.87}$ . Poumaere *et al.* [6] reported a nearly linear scaling of the slip velocity with the wall shear stress,  $U_s \sim \tau_w^{1.32}$ , for the flow of 0.08% (wt/wt) Carbopol gel along a glass capillary. However, Geraud *et al.* [26] reported a quadratic model for the variation of slip velocity with respect to the wall stress,  $U_s \sim \tau_w^2$ , for the flow of 0.1% (wt/wt) Carbopol solution in a Hele-Shaw cell made of glass. Furthermore, from the available studies [23–26], we find that the effect of solvent viscosity or Carbopol concentration on the wall slip of Carbopol gel in the capillary flow is missing. The question raised here is if there is any general equation that can be used to describe the slip behaviour of Carbopol gels with different concentrations in a glass capillary tube. In particular, we are motivated to examine if the exponent of scaling law is independent of the concentration of the fluid and viscosity of the solvent and how the prefactor can be related to these parameters.

In the present study a novel experimental setup is used to provide high resolution measurement of the kinematics and dynamics of Carbopol solutions flow in a glass capillary tube. The setup was equipped with flow measurement tools as well as an optical coherence tomography (OCT) device as a high resolution imaging device. It allows us to directly visualize the flow of tracing particles seeded in the fluid. The measured velocimetric and viscometric data are analysed to provide a power-law correlation relating the wall-slip velocity of the gels to excess shear stress, as well as an estimation of their sliding yield stress. To assess the generality of the scaling law, Carbopol solutions with different concentrations, stirring rates during preparation, and solvent viscosities are used in our experiments. In addition, the thickness of the slip layer is estimated indirectly by analysing the velocity data and the dynamics of the flow.

The chapter is organized as follows. The rheological properties of Carbopol solu-

tions and details of experimental setup used in this study are described in Sec. 4.2 and Sec. 4.3, respectively. A systematic assessment of the validity and reliability of our velocimetric and viscometric measurements is presented in Sec. 4.4. Moreover, the image processing methodology, used to estimate the slip velocity, is described in this section with emphasis on its accuracy and validation. The results obtained for the sliding yield stress and wall-slip velocity are reported in detail in Sec. 4.5. The chapter ends with a discussion on the general phenomenological relationship between the wall-slip velocity of Carbopol gels in a capillary flow, and the wall shear stress.

## 4.2 Materials and rheometry

The microstructure of Carbopol gels and their macroscopic rheological behaviour depend on the polymer concentration and stirring rate during preparation [26]. We varied these two parameters to investigate the effect of fluid microstructure and rheology. A list of Carbopol gels, used in our experiments, as well as the parameters regarding their preparation are summarized in Table 1.

The working fluids were Carbopol solutions with 0.075%, 0.1%, 0.15%, 0.2%, 0.25%, and 0.3% weight concentrations. The solutions have been prepared according to the protocol discussed in detail in Sec. 3.2. It should be underlined that the mixtures were stirred by a propeller mixer for 48 hours at a low mixing rate of 300 *rpm*. In addition, a different Carbopol solution with a low viscosity was prepared by vigorously stirring 0.1% *wt/wt* Carbopol gel with a sharp blade at 1200 *rpm*, for around two and a half minutes (fluid C8 in Table 4.1). After preparing the solutions, 4.1  $\mu\text{m}$  polystyrene beads ( $\rho_p = 1.05 \text{ g/cm}^3$ ) were dispersed in the samples as tracing particles with a volume fraction of 0.005%. Samples were sonicated in water to disrupt aggregates and achieve uniform dispersion. Prior to each test, the samples were centrifuged at 1000 *rpm* for two minutes in order to remove air bubbles trapped in the gel.

The rheology of the fluids was measured using a Kinexus Ultra + rotational rheometer (Malvern Instruments, Worcestershire, United Kingdom). A parallel plate ge-



ometry with a diameter of 60 mm was used for rheological measurements. In order to minimize the effect of wall slip on the rheological measurements of the yield-stress fluids, 46  $\mu\text{m}$  roughness sandpaper was glued on the surface of the parallel plates. A series of shear-rate controlled tests for shear rates in the range of 0.0001 to 100  $1/\text{s}$  were done to determine the steady state flow curves of the fluids.

The rheological behaviour of the samples can be described well by a Herschel-Bulkley (HB) model. The HB parameters of the gels are reported in Table 4.1. The yield stress and apparent viscosity of the water-based gels increase by increasing their concentrations. The comparison between data obtained for glycerol solution-based gel and water-based gel reveals that increasing the viscosity of the solvent does not lead to a significant change in the rheological properties of the solution (compare fluid C2, and fluid C7 in Table 4.1). Moreover, we observed a significant decrease of the yield stress for 0.1%-Carbopol gel by stirring it at a high rate (see fluid C2, and fluid C8 in Table 4.1). The effect of the preparation protocol and mixing rate on the rheological behaviour of Carbopol gels have been studied before by Geraud *et al.* [26]. As described in [26], stirring the gel at a high rate might lead to the breakage of microgels in smaller units and significant modification of its microstructure.

### 4.3 Experimental setup

During this study we attempted to measure the kinematics and dynamics of a laminar flow of Carbopol gels in a glass capillary tube. Therefore, an experimental setup which includes a viscometric unit and a flow visualization unit was designed and built. A schematic image of the experimental setup is shown in Fig. 4.1(a).

The capillary tube used in this study is made of borosilicate glass and has an inner diameter ( $D$ ) of  $1.160\text{ mm} \pm 3\text{ }\mu\text{m}$  and a length ( $L$ ) of 381 mm. The outer profile is a triangular prism. It is worth mentioning that the inner diameter of the capillary tube and its uncertainty were measured by imaging its inner surface at four different points along the capillary tube. The imaging was carried out by using a confocal microscope equipped with a 10X-objective lens that provides a spatial resolution

Sample	Concentration <i>wt/wt %</i>	Solvent	Highly Sheared	$\tau_Y$ <i>Pa</i>	K <i>Pa.s<sup>n</sup></i>	n
C1	0.075	Water	—	1.4	2.2	0.4
C2	0.1	Water	—	6.0	3.8	0.4
C3	0.15	Water	—	15.1	10.6	0.4
C4	0.2	Water	—	25.8	14.0	0.4
C5	0.25	Water	—	28.1	17.4	0.4
C6	0.3	Water	—	32.4	19.8	0.4
C7	0.1	Glycerol solution(33% <i>wt/wt</i> )	—	8.0	5.2	0.4
C8	0.1	Water	Yes	0.1	0.4	0.6

**Table 4.1:** List of Carbopol gels including different parameters used to prepare them and their rheological properties. The HB parameters were obtained from the best Herschel-Bulkley fit of the Carbopol solutions with R-squared better than 0.99.

of about  $1 \mu m$ . The dynamics of the flow in the glass capillary tube was measured directly through a viscometric unit which consists of a syringe pump (kdScientific) and inline pressure sensors (Elveflow). Two sets of pressure sensors with measuring ranges of  $0 - 340 \text{ mbar}$  and  $0 - 2 \text{ bar}$ , and an accuracy of 0.2% of the full scale were used in our experiments to measure the pressure drop along the capillary tube. An optical coherence tomography device from Thorlabs (TEL1300V2-BU) was used to visualize the flow of the working fluid seeded by polystyrene beads.

The OCT is a real-time imaging modality that works based on interferometry with a broad bandwidth light source. The device is used to obtain cross-sectional images of a specimen from the backscattered light, with micrometer-scale axial and transverse resolution and millisecond temporal resolution [85]. The OCT focuses a collimated beam with the center wave length of  $1300 \text{ nm}$  to the specimen by using a 5x-objective lens. The depth of focus of the vertical imaging is approximately  $3.5 \text{ mm}$  in a medium with the same refractive index as air, while the lateral field of view is adjusted to be  $5 \text{ mm}$ . The lateral scanning of the sample is performed by moving the vertical scanning beam laterally through a two-galvo mirror system. The spacial resolution of vertical imaging of the sample is around  $3.5 \mu m$  while its

lateral resolution, which is limited to the thickness of the scanning beam, is around  $13 \mu m$ . The cross-sectional images of the flow generated by the OCT are automatically recorded on a computer disk with a rate of 10 per second [85]. A sample OCT image of tracing particles across the capillary tube is shown in Fig. 4.1(b).

The capillary tube was fixed on a stage such that its flat outer surface is exposed towards the OCT beam. This helps to minimize the effect of unwanted refraction on the capillary wall and consequently aberrations in the images. Besides, in order to maximize the contrast between the images of tracing particles and the background, the OCT beam was slightly tilted with respect to the normal of the outer capillary surface ( $\theta \sim 3^\circ$ ); see Fig. 4.1(a). Before each experiment, the capillary tube was cleaned using distilled water, followed by rinsing with methanol. The fluid was pumped through the capillary tube for approximately two minutes before flow measurements commenced. We conducted experiments at various flow rates to span a relatively wide range of Bingham numbers,  $0.1 < B < 6$ . The Reynolds number in our experiments is limited to  $10^{-7} < Re < 1$ . Here the Reynolds number, and the Bingham number are defined as,

$$Re = \frac{16}{8^{n-1}\pi^{2-n}} \left( \frac{n}{3n+1} \right)^n \frac{\rho_f Q^{2-n} D^{3n-4}}{K},$$

$$B = \frac{\tau_Y}{\tau_w},$$

where  $\rho_f$  is the density of the fluid,  $Q$  is the imposed flow rate through the capillary tube.

#### 4.4 Experimental measurements and uncertainties

The wall shear stress and the slip velocity are the key parameters calculated in this study through velocimetric and viscometric measurements of the Poiseuille flow. The wall shear stress is calculated by  $\tau_w = (D/4L)\Delta P$ , where  $\Delta P$  is the measured pressure drop along the capillary tube. The error in the wall shear stress coming from the uncertainty in the measurement of the capillary diameter is less than 0.3%. Hence, the uncertainty in the calculated values of wall shear stress is directly

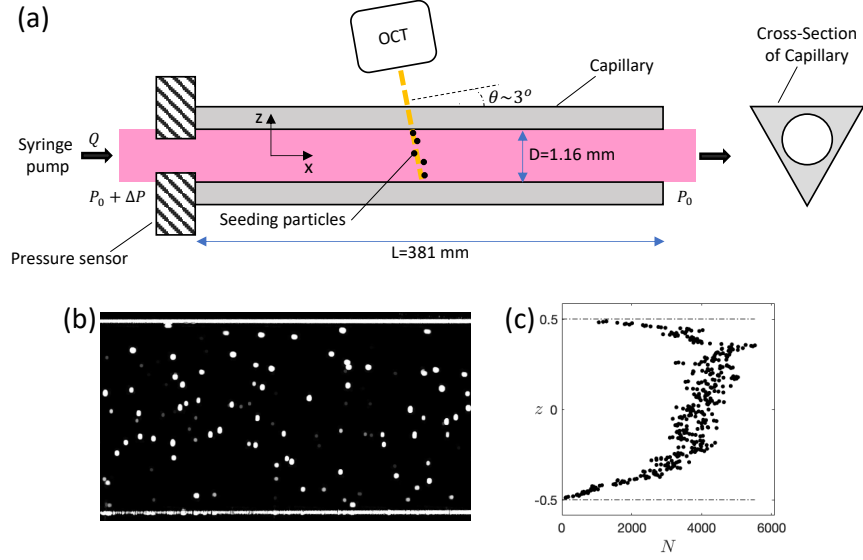


**Figure 4.1:** (a) Schematic diagram of the experimental setup, (b) an image of tracing particles in  $x$ - $z$  plane acquired by the OCT. The white lines in this image indicates the wall positions. Note that the position of the particles along  $z$ -direction were corrected by considering the effect of refraction on the capillary wall. Considering the linearity of Snell's law, we mapped the measured positions of particles and walls to their true positions, by applying a linear scaling. The scale factor is obtained from the ratio of the measured diameter of capillary tube in the OCT-images and its actual size. (c) The number of velocity vectors,  $N$ , that contribute to each bin across the capillary tube. Here, the  $z$ -axis represents the distance from the centerline of the cell, normalized by the diameter of the capillary tube. Note that the velocity data were obtained from applying the PTV to 1000 paired images. Then the PTV data were averaged using a spatial binning size of  $5\mu m$ .

related to the accuracy of our pressure drop measurements. The slip velocity is estimated by a linear extension of the velocity profile to the wall position. Therefore, the validity of our slip data is strongly dependent on the accuracy of measurement of the velocity profile and the wall position.

Direct visualization of the flow was exploited to study flow kinematics in the capillary tube. The velocity profile across the capillary tube was measured using an augmented PTV technique, described in detail in [86] and implemented in a commercial analysis package (LaVision Davis 7.2). The resolution provided by this technique is in the same order of magnitude as the tracing particles diameter, hence the velocity near the wall is measured accurately.<sup>3</sup> The velocity vectors obtained from raw PTV data disperse randomly. In order to sort out the data, the cross-section of the pipe is divided into a number of bins with a thickness of  $5\text{ }\mu\text{m}$ . The velocity profile was constructed by taking the average of velocity vectors in each bin separately. A typical distribution of velocity vectors, obtained from the PTV for a specific case study, is indicated in Fig. 4.1(c). Every single point on the velocity profile is obtained by using at least 100 PTV data points.

A portion of the light incident on the sample reflects from the inner surface of the capillary wall, due to the difference in refractive indices of the glass and the working fluid (see Fig. 4.1(b)). It provides enough contrast with respect to the image background to recognize the wall position in the OCT images. An edge detection code was used to determine the position of the wall with an accuracy of  $10 - 15\text{ }\mu\text{m}$ .

#### 4.4.1 Validation of experimental measurements

We examined the accuracy of the velocity measurements, and the validity of the viscometric measurements by studying the flow of a Newtonian fluid, 31% *wt/wt* glycerol solution along the capillary tube at different flow rates. Results are depicted in Fig. 4.2(a–b). The normalized velocity profiles measured for the glycerol

---

<sup>3</sup>It should be underlined that under the assumption of negligible body force, the measured velocities for the tracing particles, in the vicinity of the wall, represent the flow field in this region well.

solution at three different flow rates all coincide and correlate well with the theoretical parabolic curve across the whole width of the channel (with  $R^2 = 99\%$  and  $L_2 = 0.010$ ) and  $50 \mu\text{m}$  to the wall-position (with  $R^2 = 97\%$  and  $L_2 = 0.013$ ), where  $R^2$  and  $L_2$  represent the R-squared and the second norm of error, respectively (see Fig. 4.2(a)).

The flow curves of the solution obtained by using the capillary viscometric unit and the rotational rheometer with parallel plate geometry are compared in Fig. 4.2(b) at different shear rates. In the case of the capillary tube geometry, the apparent wall shear rate is determined using the Rabinowitsch equation [87],

$$\dot{\gamma}_w = 8Q/(\pi D^3) \left[ 3 + \frac{d \ln(8Q/(\pi D^3))}{d \ln(\tau_w)} \right],$$

where  $Q$  is the imposed flow rate. As shown in Fig. 4.2(b), the results obtained from our capillary device show good agreement with rheological data from the rotational rheometry.

Regarding the comprehensive literature on the complex rheology of viscoplastic fluids [1, 83, 84], possible time-dependent behaviour of these fluids can be considered as a potential source of uncertainty in the velocimetric and viscometric measurements of the flow [25]. We performed a time-dependent experiment to investigate the dynamic response of the fluid within the range of flow rates in our experiments. Fig. 4.3 represents the flow curve measured during a varied flow rate by time test, for fluid C1. As indicated in the inset of this figure, the fluid is sheared over a ramp-up and ramp-down test with a time step of 1 min. The wall shear stress corresponding to each flow rate is calculated by averaging the measured pressure drop over time. The data corresponding to the ramp-up test overlap those obtained during the ramp-down test. Slight discrepancies observed when the wall shear stress is below the yield stress, are in the order of magnitude of the experimental measurements errors.

It can be concluded from the results in Fig. 4.3 that the steady shear stress measured at each step is not influenced by pre-shearing, shear history, or any other source of

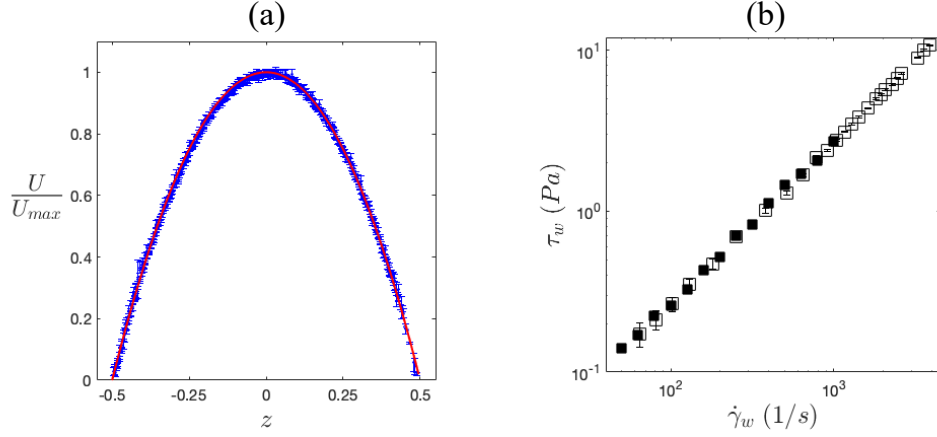


**Figure 4.2:** Benchmarking the (a) velocimetric measurements and (b) viscometric measurements with a Newtonian fluid, 31% *wt/wt* glycerol solution. Panel (a) presents the normalized velocity profiles of the solution corresponding to three different average velocities, 0.16 mm/s, 0.8 mm/s, and 1.7 mm/s (blue dots). The red curve represents the theoretical velocity profile. Panel (b) presents the flow curves of the solution obtained from the capillary viscometer (empty symbols), and a rotational rheometer with parallel plates geometry (filled symbols).

time dependency related to the rheology of the fluid or response time of our experimental setup, at a long enough time scale which is in the order of magnitude of our measurements time resolution, i.e. 60 s. Hence, the repeatability of our steady state tests and measurements is guaranteed. It should be underlined that the data reported in the next section were measured two minutes after starting a constant flow rate test, in order to have steady flow in the capillary tube.

#### 4.4.2 Estimation of the slip velocity

In this study, the slip behaviour was studied using direct visualization of the flow. The wall-slip velocity is estimated by linear extrapolation of velocity data corresponding to the region within 50  $\mu\text{m}$  of the wall, to the wall position. A similar methodology has been applied in [25, 26] to determine the slip velocity by analysing the flow field near the shearing surfaces. The methodology used to estimate the slip velocity is shown in Fig. 4.4(a–b). Normalized velocity profiles for

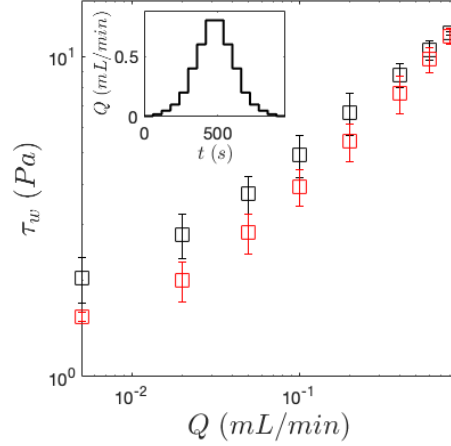


**Figure 4.3:** Intrinsic response of the gel: capillary flow curve of 0.075% wt/wt Carbopol solution (fluid C1) measured during a varied flowrate by time test (see inset). Data obtained for ramp-up and ramp-down tests are presented by black squares, and red squares, respectively.

the flow of the glycerol solution, and fluid C1 at two different shear stresses above and below the yield stress are plotted here with a focus on the near-wall velocity data. For the flow of glycerol solution, the fitted line on near-wall velocity data, over different flow rates, crosses the zero-velocity at a point located in the middle of the upper and lower bounds of the wall position (see Fig. 4.4(a)). This confirms the validity of the technique used to estimate the slip velocity over a wide range of wall shear rates. However, as shown in Fig. 4.4(b), the Carbopol gel apparently slips on the capillary wall, in both fully plugged and deformation regimes. In the case of fully plugged flow, tracing particles 4  $\mu m$  of the wall position move at the same pace as those in the middle of the capillary tube. The slip velocity in the deformation regime is estimated by linear extension of the velocity profile to the wall position.

Alternatively, the slip velocity can be quantified indirectly by analysing the capillary rheometry data. The slip flow rate,  $Q_s$ , can be estimated by subtracting the flow rate calculated based on Herschel-Bulkley model and no-slip condition on the



wall, from the imposed flow rate,  $Q$ , [24, 88],

$$Q_s = Q - \frac{\pi D^3}{8(\frac{1}{n} + 1)K^{\frac{1}{n}}} \frac{(\tau_w - \tau_Y)^{\frac{1}{n}+1}}{\tau_w} \left[ 1 - \frac{2(1 - \frac{\tau_Y}{\tau_w})^2}{\frac{1}{n} + 3} - \frac{2(1 - \frac{\tau_Y}{\tau_w})}{\frac{1}{n} + 2} \frac{\tau_Y}{\tau_w} \right] \quad (4.2)$$

where the HB parameters of the fluids,  $K$ ,  $n$ ,  $\tau_Y$  are given in Table. 4.1. Accordingly, the wall-slip velocity can be estimated by  $U_s = 4Q_s/(\pi D^2)$ . We used rather the direct methodology to estimate the slip velocity due to its independence on the rheological properties of the fluid and measured dynamics of the flow that might include noticeable uncertainties.

In addition to the slip velocity, characterising the thickness of the apparent slip layer that develops at the wall is of interest in this study. According to the literature, the thickness of this layer is expected to be roughly less than one micron [18, 24, 25]. This ultra-thin layer is very difficult to be visualized directly. Alternatively, the thickness of the apparent slip layer can be estimated indirectly by  $\Lambda = \eta_s U_s / \tau_w$ , under isothermal and laminar conditions and by the assumption that it contains an ultra-thin particle-depleted, fully developed, Newtonian and incompressible layer of the solvent fluid [45].

## 4.5 Results and discussion

### 4.5.1 Sliding yield stress

Figure 4.5(a) displays the capillary flow curves of the Carbopol gels. Besides, the friction factor calculated from the flow curve data is illustrated versus Reynolds number in the inset of Fig. 4.5(a). The comparison between the experimental friction factor and the theoretical line obtained from the Herschel-Buckley model with a no-slip condition on the wall shows the signature of wall-slip behaviour of the Carbopol gels, particularly at low Reynolds numbers. The salient feature of the flow curves is their linearity below the yielding point (see Fig. 4.5(b)). Our flow visualization results confirm that the linear region corresponds to a pure plug flow (see the blue curve in Fig. 4.4(b)). It can be interpreted as the lubrication of unyielded gel over a thin layer of a Newtonian fluid on the wall. As expected, above

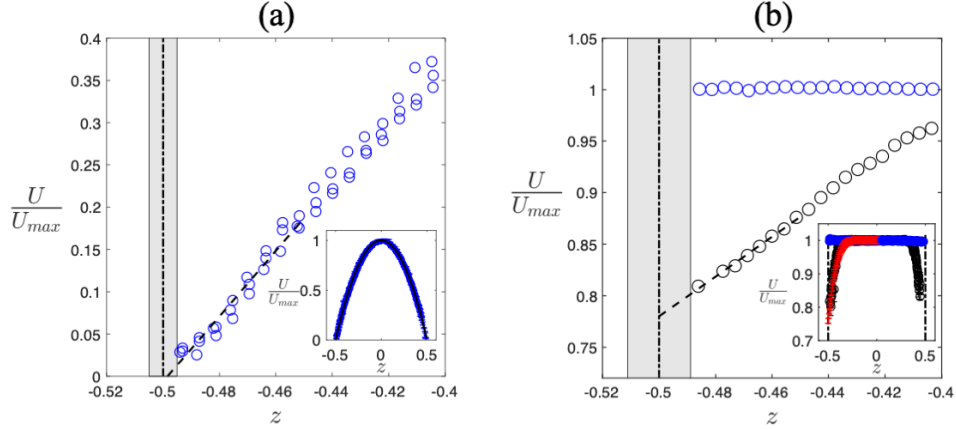


**Figure 4.4:** (a) Normalized velocity profiles for (a) a 31% wt/wt glycerol solution, and (b) a Carbopol solution (fluid C7), at  $B = 1.5$  (blue), and  $B = 0.7$  (black); the dashed line represents the fitted line on velocity data corresponding to the region  $50 \mu m$  of the wall position. The gray box, and the dashdotted line show the bounds of the wall position and its center, respectively. The complete velocity profiles across the pipe are replotted in the insets of the panels. The red symbols represent the analytical curve calculated by using the rheological parameters of the gel (see Table 4.1).

the yielding point, flow is due to both deformation and slip (see the black curve in Fig. 4.4(b)). Non-linearity of the flow curves in this region is related to the shear thinning behaviour of the yielded Carbopol.

The slip behaviour of the fluid contradicts the common belief of the yielding threshold for the motion of fluid along the capillary tube. The question raised here is if there is a sliding threshold for the flow. Seth *et al.* [22] proved the presence of the sliding yield stress in the steady torsional flow and related it to the attractive forces between the soft particles and the shearing surfaces. Regarding the linear behaviour of the flow curves below the yielding point, we estimate the value of the sliding threshold by linear extrapolation of the flow curve over this region to the zero flow rate. Results are illustrated in the inset of Fig. 4.5(b). For water-based Carbopol gel with a concentration greater than 0.075%, the sliding threshold changes linearly with the yield stress, as  $\tau_{SY} = (0.18 \pm 0.02) \tau_Y$ . According to our

results, another parameter that affects the sliding yield stress is the viscosity of solvent. The sliding yield stress for glycerol solution-based Carbopol gels, scaled by the viscosity ratio of its solvent to water, i.e.  $\eta_s/\eta_w$ , follows the linear relationship obtained for the water-based Carbopol gels (see the inset of Fig. 4.5(b)). In other words, by increasing the viscosity of the base fluid, the sliding yield stress increases by roughly the same ratio.

#### 4.5.2 Wall slip

The values of the slip velocity for the flow of Carbopol gels at different flow rates are estimated by using the direct technique (described in Sec. 4.2). The data for the slip velocities of Carbopol gels at different wall shear stresses are presented in Fig. 4.6(a). For each Carbopol gel, the slip velocity increases with the wall shear stress, in both fully plugged and deformation regimes. Alternatively, the values of slip velocity are calculated from Eq. 4.2. The corresponding values obtained for fluid *C2* and fluid *C3* are shown by dashed curves. The agreement between the data obtained from Eq. 4.2 and those obtained from direct estimation of the wall-slip velocity confirms the assumption of an insignificant confinement effect [26] and the validity of a HB model for the fluid rheology considering the actual length scale of the problem.

The estimated values for the thickness of the slip layer are shown in Fig. 4.6(b). For each Carbopol gel, the slip layer thickens with increasing wall shear stress until it reaches a plateau which is a function of gel concentration. According to the theory [18, 19], the thickness of the slip layer is proportional to the deformation of soft microgels. This deformation results from the interplay between the osmotic force, hydrodynamic lubrication force and surface forces. The growth of the slip layer by the wall-shear stress in the deformation regime implies non-negligible effect of hydrodynamic force on the deformation of particles. Since the deformation of microgels is limited by their yielding strain, the thickness of the slip layer remains constant above the yielding point. The influence of the normal stress or pressure on the wall-slip of polymer solutions and melts was discussed in the literature before [89]. Interestingly, our results show no sign of discernible change in the slip layer

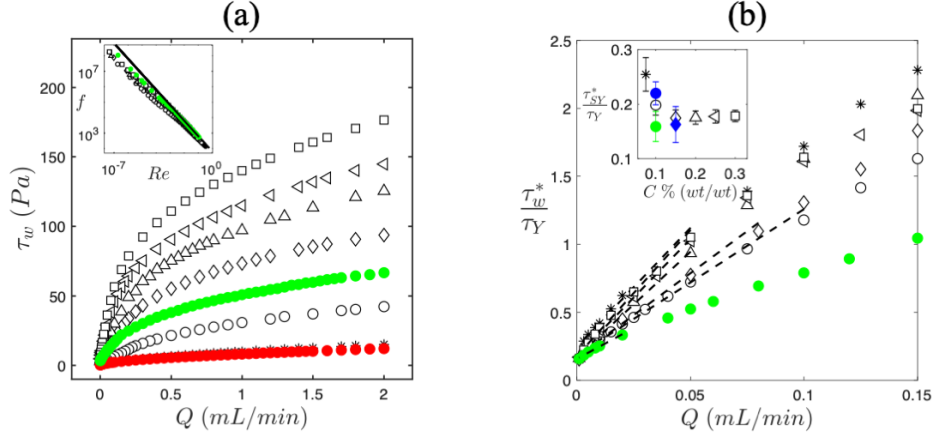


**Figure 4.5:** (a) Wall shear stress versus flow rate for capillary flow of Carbopol gels with concentrations of 0.75% (\*), 0.1% (○), 0.15% (◇), 0.2% (△), 0.25% (◁), 0.3% (□); The data corresponding to the highly sheared 0.1% wt/wt Carbopol gel and glycerol solution-based 0.1% wt/wt Carbopol gel are indicated by ●, and ●, respectively. In addition, the friction factor versus Reynolds number is illustrated in the inset of panel (a); the solid line in this figure represents the analytical results obtained based on Herschel-Bulkley model and no-slip condition on the wall. For all the cases except for the highly sheared 0.1% wt/wt Carbopol gel, the linear regime before yielding and non-linear shear thinning regime after yielding is observable. The enlarged linear region for Carbopol solutions are shown in panel (b). (b) Wall shear stress normalized by the yields stress versus the flow rate; the dashed lines represent the fitted lines on the data in the linear region ( $\tau_w < \tau_Y$ ). The inset of panel (b) presents the sliding yield stress normalized by the yield stress with respect to the concentration of the Carbopol gels. To emphasize the effect of viscosity of the solvent, we prepared 0.1% wt/wt Carbopol gel and 0.15% wt/wt Carbopol gel with a different concentration of glycerol, 11% wt/wt, and calculated the sliding yield stress. The corresponding values are shown in the inset of panel (b) with blue symbols. Note that in panel (b), the values of wall shear stress and sliding yield stress obtained for glycerol solution-based Carbopol gels were scaled by the viscosity ratio of the glycerol solution to water, i.e.  $(\tau_w^*, \tau_{SY}^*) = \frac{(\tau_w, \tau_{SY})}{\eta_s/\eta_w}$ .

thickness with the pressure, above the yielding point. Note that these observations are limited to the range of pressure in our experiments.

As indicated in Fig. 4.6(a–b), wall-slip velocity and thickness of the lubrication layer decrease with increasing concentration of Carbopol gel. One possible explanation is related to the osmotic deswelling of Carbopol microgels at higher concentrations; the higher the concentration of Carbopol gel is, the higher the induced osmotic pressure is obtained that pushes the soft particles more against the shearing surfaces and leads to greater deformation of the microgels [18, 22, 90, 91].

Studying the data reported in Fig. 4.6 allows us to investigate a general scaling law for the slip velocity of Carbopol gels. The whole set of data in both regions below and above the yielding point show a relatively similar trend with respect to the excess shear stress. The regression analysis of the data indicates that over the entire range of wall shear stresses, the slip velocity for water-based Carbopol solutions changes by a power-law relation with respect to the excess shear stress,  $U_s = f(C)(\tau_w - \tau_{SY})^{1.04 \pm 0.06}$  ( $R^2 = 0.996$ ), where the prefactor is well represented by a function of the gel concentration,  $f(C) = 6.23 \times 10^{-5} C^{-3.54}$  ( $R^2 = 0.987$ ). More precisely, below the yielding point, the slip velocity data slightly deviate from the linear variation trend, while above the yielding point the slip velocity versus excess wall stress exhibit strictly linear behaviour. The quasi-linear variation of slip velocity with shear stress was also predicted by Seth *et al.* [19, 22] for the steady torsional flow and Gonzalez *et al.* [23], and Poumaere *et al.* [25] for the capillary flow, over the deformation regime.

A comparison of slip velocities obtained for glycerol solution-based and water-based 0.1% Carbopol gel reveals the roughly linear dependence of the slip velocity on the fluidity of the solvent, i.e.  $1/\eta_s$ . As shown in Fig. 4.6(a), the slip velocities obtained for fluid C7 scaled by the viscosity ratio of water to glycerol solution, follow those predicted for fluid C2 well. The linear dependence of slip velocity on the fluidity of the solvent is in accordance with the lubrication model and experimental results reported in [18, 19] for the wall-slip velocity of microgel pastes in a steady torsional flow and on both weakly attractive and repulsive surfaces. It was

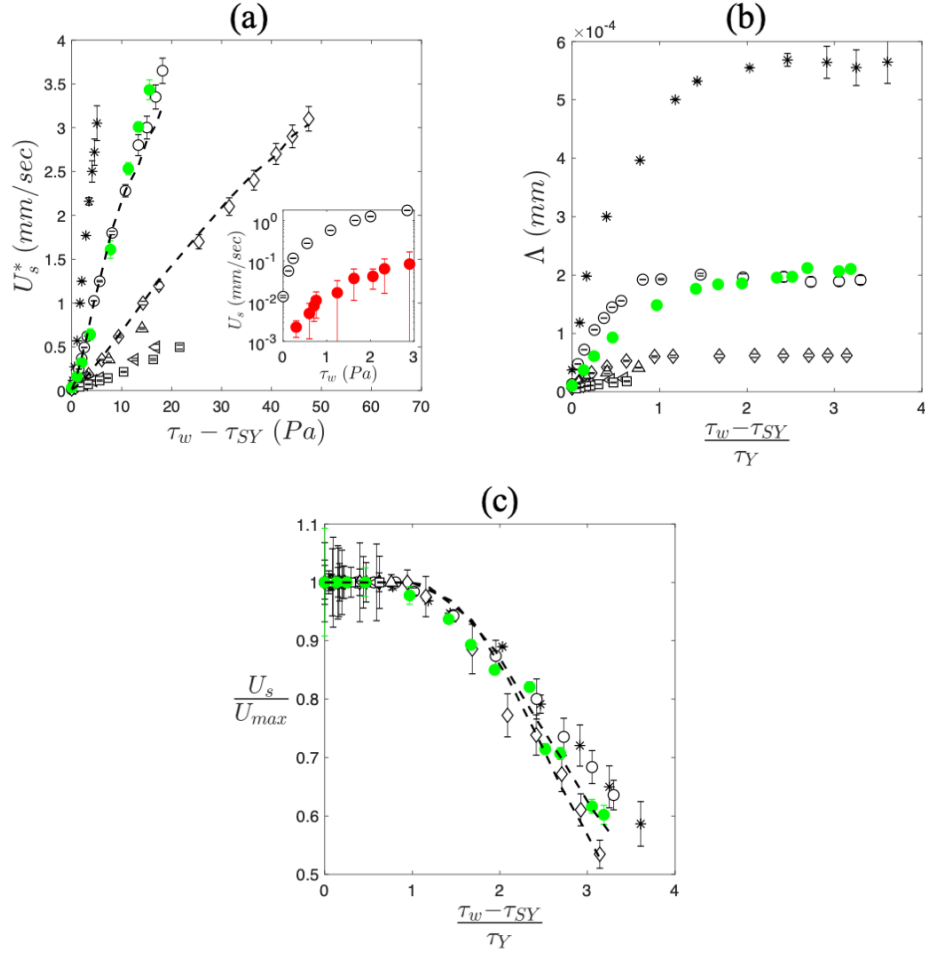


**Figure 4.6:** Variation of (a) the slip velocity with the excess shear stress, (b) the thickness of the slip layer with the excess shear stress normalized by the yield stress, (c) the slip velocity normalized by the maximum velocity with the excess shear stress normalized by the yield stress. Note that, in panel (a), the values of slip velocity obtained for glycerol-solution based Carbopol gel (fluid C7) was scaled by the viscosity ratio of water to solvent,  $U_s^* = \frac{U_s}{\eta_w/\eta_s}$ . The values of slip velocity corresponding to fluid C2 and fluid C8 are compared in the inset of the panel (a). The symbols used in this figure are similar to those defined in the caption of Fig. 4.5. The dashed lines in panel (a) and (c) represent the values of slip velocity calculated from Eq. 4.2 for fluid C2 and fluid C3.

also indicated that the wall-slip velocity of microgel pastes in a steady torsional flow varies by the elastic modulus of the material and the radius of the soft particles [18, 19]. Meeker *et al.* [18] indicated that a decrease in either the radius of microgels or the elasticity of the material leads to a decrease in the slip velocity. These two parameters vary with the gel concentration and the stirring rate during its preparation. The higher the stirring rate is, the smaller the microgels are, the lower the elastic modulus is, and the more fluid like the resultant solution is [26]. Hence, it is interesting to compare the wall-slip behaviour of two gels with the same base and concentration, but prepared at different stirring rates. We repeated slip measurement tests for the highly sheared gel (fluid C8) and compared the data with those predicted for the gently mixed gel (fluid C2). Results are illustrated in the inset of Fig. 4.6(a). In agreement with the experimental results reported by Meeker *et al.* for the wall-slip of microgel pastes in a steady torsional flow, a significant decrease in the slip velocity is observed when we use the Carbopol solution prepared at the higher stirring rate.

To have a better interpretation of the data, we consider the normalized slip velocity,  $U_s/U_{max}$ , against the normalized excess shear stress,  $(\tau_w - \tau_{SY})/\tau_Y$  (see Fig. 4.6(c)). The interesting point is that the normalized slip velocities corresponding to the Carbopol gels with different concentrations and solvent viscosities follow each other closely (see Fig. 4.6(b)), and they are well represented by

$$\frac{U_s}{U_{max}} = 1 - (0.04 \pm 0.01) \left( \frac{\tau_w - \tau_{SY}}{\tau_Y} \right)^{2 \pm 0.05} (R^2 = 0.937),$$

above the yielding point. However, we do not have a theory to quantitatively explain the aforementioned experimental based model for normalized slip velocity in the deformation regime.

## 4.6 Conclusion

The slip behaviour of Carbopol gels in a pressure driven flow was investigated by velocimetric and viscometric measurements of the flow in a glass capillary tube. Two flow regimes were obtained for Poiseuille flow of Carbopol gels. Below the

yield stress, a fully plugged flow was obtained that is only due to slip at the capillary walls. The linear form of the capillary flow curve in this regime, obtained from our viscometric measurements, proved the idea of lubrication of the unyielded gel by a thin layer of a Newtonian fluid. Above the yielding point, a sheared layer of gel clearly slips on the wall and the contribution of slip-flow rate to the total flow rate is not negligible. The sliding threshold below which the gel sticks to the capillary wall was estimated by analyzing the viscometric measurements. It was found that the sliding threshold changes linearly by the yield stress of the gel and roughly linearly by the viscosity of its solvent.

Our findings suggest the existence of a general relationship to explain the wall slip of Carbopol gels in a Poiseuille flow (see Eq. 4.1). The slip velocity is linked to the dynamics of flow by a quasi-linear polynomial,  $U_s^* = f(C)(\tau_w - \tau_{SY})^{1.04 \pm 0.06}$ , where the prefactor,  $f(C)$  can be defined as a monotonic function of the concentration of the gel. Our results confirm that increasing the viscosity of the solvent by a factor leads to a decrease in the wall-slip velocity by the same factor. In addition, the wall slip is linked to the microstructure of the fluid which was varied by the concentration of the polymer and the stirring rate during preparation. Increasing the concentration of the fluid or stirring the gel at a higher rate during preparation leads to a significant decrease in the slip velocity. However, the exponent of the scaling law for the slip velocity with respect to the excess shear stress is independent of the solvent viscosity and concentration of the gels. Accordingly, the thickness of the slip layer was found to increase with the wall shear stress in the fully plugged regime and to finally reach a constant value above the yielding point.

From the modified lubrication theory explained in Ref [19, 22], one might expect that for a wetting surface of glass, the repulsive forces between the surface and Carbopol microgels dominate and the slip velocity changes linearly with the wall-shear stress. From this perspective, the quasi-linear phenomenological relationship obtained here for the variation of wall-slip velocity with respect to the wall-shear stress below the yielding point might be attributed to the contribution of repulsive forces. Moreover, in accordance with the theory, above the yielding point the slip layer thickness tends to a constant value and the slip velocity varies



linearly with the wall-shear stress. Despite these agreements, our experimental findings imply that the physical picture of wall-slip behaviour of Carbopol gel in the glass capillary tube is more complex and cannot be explained thoroughly by the modified hydrodynamic lubrication theory [19]. Our experiments indicate that the role of weakly attractive surface forces which manifest themselves in the presence of slight sliding threshold is not negligible. Furthermore, in contrast to the theory the effect of hydrodynamic forces are not negligible at low shear stresses; the slip-layer thickness increases by increasing the slip velocity.

## Chapter 5

# Observation of reacting multi-layer flows in a Hele-Shaw cell<sup>1</sup>

### 5.1 Introduction

In this chapter, we address the problem of vertically stratified multi-layer flows in a 3-layer Hele-Shaw cell from a theoretical and experimental point of view. The fluid layers are miscible and a chemical reaction between the layers leads to gelation at the interface. A schematic image of the flow in this system is depicted in Fig. 5.1(a). The original motivation of this work stems from the fabrication of hydrogel based biomaterial by chemical patterning at the interfaces of two fluid streams in a parallel flow system that finds its application in the field of scaffold engineering. Scaffolds are biocompatible materials that act as a replacement to organ and tissue transplantation and designed to mimic the extracellular matrix by providing structural support that promotes cell attachment and proliferation.

A technique to fabricate biomaterial is 3D extrusion printing, i.e. in-situ layering of liquids coupled with gelation at their interface, to rapidly produce hydrogels [93].

---

<sup>1</sup>A version of this chapter is ready for submission for publication [92].

Natural polymers such as alginate or nano-fibrillated cellulose are particularly suitable for in-situ layering as they gelate when contacted with a salt solution [93–96]. Under creeping flow conditions, Boyd et al. [97] demonstrated the potential of this process by printing sculpted bodies. They considered fabrication of the hydrogel at small scale by combining two laminar flows of the gel precursor solutions, a salt solution and an alginate solution, in a microfluidic device. We are motivated by the results of previous studies on microfluidic patterning of hydrogels and the scientific challenge to scale up the process to produce structures at larger scales.

In this research, we consider scaling up the reactive multi-layer flow in a planar two-dimensional channel. In particular, we scale up the aspect ratio of the geometry. The inertial forces are small and the system operates at relatively low Reynolds number, i.e.  $Re < 1$ . A particular application for this configuration is in the production of skin scaffolds [98]. The skin scaffold is required to be thin and accurate in thickness. In this concept, this reactive multi-layered flow system in a Hele-Shaw cell can be considered as a good candidate for printing skin scaffolds. In this flow system, the gel layer develops on one interface due to the reaction between two fluid streams and the gelled product is lubricated and transported along the channel by the upper and lower Newtonian fluid streams (see Fig. 5.1(a)). What seems necessary here is first to maintain a stable flow configuration, and second to control the rate of the gel production under the stable flow regimes. Hence, a systematic study is needed to delineate the conditions for stable operation under different flow conditions, and to determine the growth rate of the gel layer.

The Hele-Shaw cell provides a simple rectangular geometry where inertia is small and the principal stress is along the thickness direction (Fig. 5.1(a)). Typically, the Hele-Shaw flows of Newtonian fluids with no layering operate at low inertia, which inherently ensures a stable and 1-D flow. However, in our vertically stratified flow configuration, the layering is questionable; i.e. the viscosity stratification, density difference between the layers, and the chemical reaction coupled to local rheology, have the potential to destabilize the flow configuration.

From the literature, we expect that the viscosity stratification at such a low Reynolds

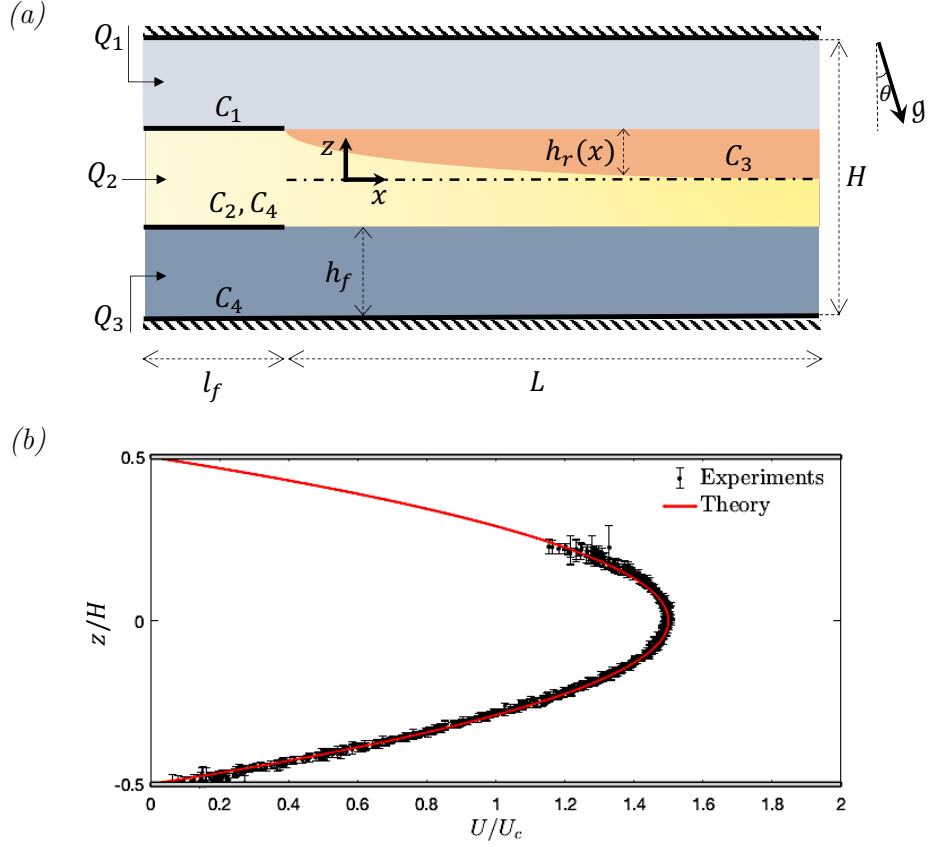


**Figure 5.1:** Overview of the experimental Hele-Shaw cell and variables. (a) Schematic of the Hele-Shaw cell at an inclination angle  $\theta$  where  $Q_1$ ,  $Q_2$  and  $Q_3$  are the flowrates of each fluid stream. Each fluid stream is considered as a dilute solution of four species in water, where  $c_i$  represents the concentration of  $i$ -species. The third component,  $c_3$ , is the product of chemical reaction between the first two components,  $c_1$  and  $c_2$ . The forth component,  $c_4$ , is non-reactive and affects the density of the solution. The thickness of the channel  $H = 3$  mm, entrance length  $l_f = 20$  mm, entrance height  $h_f = 0.75$  mm, reactor length  $L = 200$  mm and width  $W = 57$  mm. The position of the gel layer is defined as  $h_r(x)$ . (b) Experimental measurements of the velocity field for a Newtonian fluid at an average velocity  $U_c = 100 \mu\text{m/s}$  with no layering and no reaction, i.e.  $c_{1-4} = 0$ .

number miscible flow does not have noticeable destabilizing effects [99]. In particular, the effect of viscosity difference at low Reynolds number was investigated numerically in a separate study for an iso-dense layered flow [92]. Representative results for  $Re = 3$ , and  $Pe = \infty$  are presented in Fig. 5.2(a)–(d) where the stability of layered, non-reactive Newtonian fluids that differ in viscosity, is compared. The flow field is unconditionally stable over a wide ranges of viscosity ratio between the core and sheath flow. It might be attributed to the fact that in such an inertia-less flow the stress state is dominated by viscous shear. However, in our vertically stratified flow configuration the density differences between the layers have the potential to destabilize the flow with slight inclination angles [100]. Because the stress state is very different to conventional Hele-Shaw flows, i.e. the gravitation body force is negligible, the effects of orientation and density gradients in this vertically stratified flow configuration are nontrivial and potentially place demanding constraints on the bounds in which a stable flow can be achieved.

Another parameter that plays an important role on the interfacial stability in this flow configuration is the yield stress of the fluid. Previous studies on the iso-dense core-annular flow and planar displacement flow of a viscoplastic fluid suggested that the flow can remain stable if the interfacial stress is less than the yield stress of the layered fluid [101, 102]. In Hele-Shaw flows, a similar stabilizing mechanism can be implied. What is unclear is if the flow can remain stratified through viscoplastic lubrication when a gravitational body force is present.

Furthermore, the effects of diffusion and reaction on the flow configuration become increasingly important in cases where rheology is coupled to composition, as it has been reported in the past that a fast chemical reaction can trigger interfacial instabilities from non-monotonic rheology [103–105]. According to the literature, stability in this case depends on the diffusivity of each species, the rate of reaction and consequent yield stress of the gel in comparison to the interfacial stresses. In particular, Burghel and Frigaard [105] demonstrated that the two-layer, horizontally stratified flows in a Hele-Shaw cell can be destabilized by a fast chemical reaction. They considered two-layer flows of an aqueous sucrose solution (at high pH, titrated with sodium hydroxide) with an aqueous Carbopol-sucrose solution (at

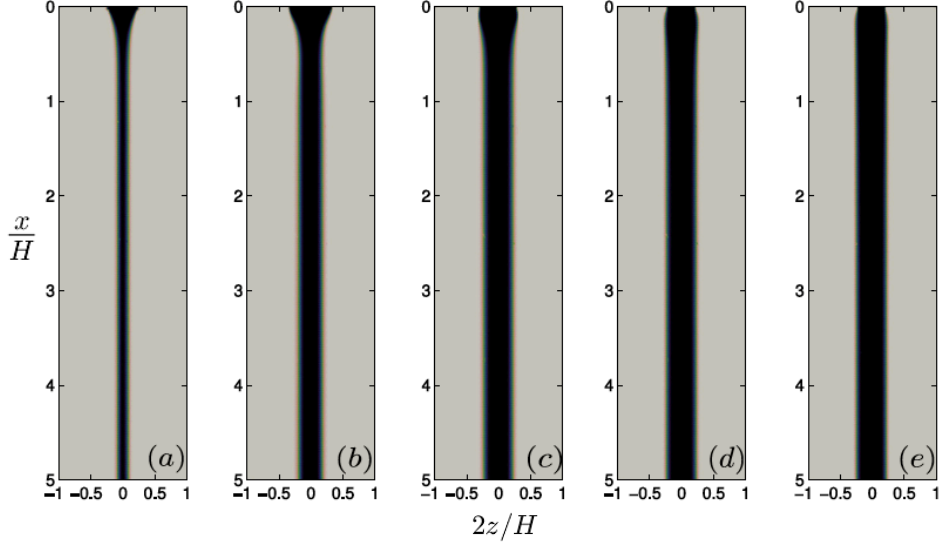


**Figure 5.2:** Numerical simulations of the concentration profiles in a layered flow [92]. The concentration profile for the inner layer (1) and outer layer (2) are denoted by black, and grey, respectively. The layers are assumed to be miscible and the fluids are Newtonian with no reaction and no diffusion, and  $Re = 3$ ,  $Pe = \infty$ , and  $Q_1/Q_2 = 1$ . The simulations were conducted for various viscosity ratios (a)  $\eta_1/\eta_2 = 0.01$ , (b)  $\eta_1/\eta_2 = 0.1$ , (c)  $\eta_1/\eta_2 = 1$ , (d)  $\eta_1/\eta_2 = 10$ , (e)  $\eta_1/\eta_2 = 100$ .

low pH). Due to the fast reaction between the layers, the neutralization of Carbopol occurs at the interface. It leads to the creation of a yield stress fluid at the interface with a shear viscosity that is much higher than that of each pure fluid stream. They speculated that the interfacial instabilities observed in this flow can be attributed to non-monotonic viscosity variation, instigated by the reaction. We note, however, that the effect of density differences across the interface in [105] is unclear. It should be underlined that in our study the flow configuration is different; in this work we layer the fluids along the thickness direction, i.e. along the principal shear stress across the cell. The question raised here is if the chemical reaction leads to instability in our flow configuration or not.

We approach generalizing the stability of these flows by considering three flow

configurations: 1) unreactive flow, 2) flow with a fully-reacted viscoplastic layer and 3) reactive flow, i.e. flow with a developing viscoplastic layer, and investigate the stability in relation to inclination angle, flow-rate ratio between the layers and, when applicable, the concentration ratio between the layers. As mentioned the density differences between the layers can be considered as a destabilizing factor of the flow configuration at slight inclination angles. In order to study the effect of this parameter on the flow configuration and its stability, we examine the multi-layered flow in two asymptotic states of the reactive flow, unreactive flow, and fully-reacted viscoplastic lubricated flow. Experimental visualization of flow across the slot is exploited to examine the stability of the flow pattern. In addition, a theoretical study is used to estimate the velocity profile across the slot under different flow conditions. The effect of reaction on the hydrodynamic stability is studied by considering the reactive multi-layered flow of an alginate and a salt solution in a horizontally aligned cell. Furthermore, the growth of the thickness of the gel layer under stable flow conditions are estimated theoretically and experimentally.

The structure of the chapter is as follows. The theoretical modelling and governing dimensionless parameters of the problem are outlined in Sec. 5.2. The solutions used in our experiments and their rheological behaviour are explained in Sec. 5.3. The experimental setup, experimental conditions, and methodologies used to measure the flow interfaces are detailed in Sec. 5.4. The results are presented in Sec. 5.5. First, the flow regimes observed at different flow conditions are explained in Sec. 5.5.1. Second, the experimental results regarding the growth of the gel layer in a reactive flow are described in Sec. 5.5.2. The chapter ends with a brief summary of the findings.

## 5.2 Theory

The problem under consideration is the three-layer flow of incompressible and miscible generalized Newtonian fluids along a Hele-Shaw cell. The flow is driven by an imposed pressure gradient and a component of gravity along the channel. Considering the large aspect ratio of the channel, the flow is assumed to be two dimensional. In addition, since the fluids are miscible, the effect of interfacial tension on

the interfaces can be neglected. Each fluid layer can be considered as a dilute solution of four species in water, such that its properties are linked to the concentration of the species. We consider a chemical reaction involving three species, shown as



where  $c_i$  denotes the mass concentration of  $i$ -species, and the stoichiometric coefficients (a,b) can change depending on the type of reaction. The non-reactive component,  $c_4$ , introduces buoyancy into the system and hence only affects the density along the layering in Fig. 5.1. Given that the governing dimensionless groups of the problem are defined as follows.

The Reynolds-number indicates the ratio of inertia forces to the viscous forces,

$$Re = \frac{\rho_c U_c H}{\mu_c} \quad (5.2)$$

where  $U_c$  is the average velocity in the channel,  $H$  is the depth of the channel, and  $\rho_c, \mu_c$  are respectively the density and viscosity of the water which are considered as the reference density and viscosity in this problem. The (Newtonian) Bingham number,  $BN$ , describes the ratio of the yield stress of the reacted fluid to the viscous stress developing in the lubricating Newtonian fluids,

$$BN = \frac{\tau_{Y,c}}{\mu_c U_c / H} \quad (5.3)$$

where  $\tau_{Y,c}$  is the reference value for the yield stress that can be estimated as the yield stress of the fully-reacted material. In addition, the ratio of viscosity between the  $j$ -th fluid stream and water (upper stream) is,

$$m_j = \frac{K_j (U_c / H)^{n_j - 1}}{\mu_c} \quad (5.4)$$

where  $K_j$ , and  $n_j$  denote the consistency and shear thinning index of  $j$ -fluid stream at the inflow. Note that in our experiments, the upper and lower fluid streams are Newtonian, hence  $n_1 = n_3 = 1$ . The ratio of buoyancy stresses caused by the



density difference between the  $j$ -th layer and water layer to the viscous stresses is represented by  $\chi_j$ ,

$$\chi_j = \frac{Re}{Fr_j^2} \sin \theta \quad (5.5)$$

where  $\theta$  is the inclination angle of the channel (see Fig. 5.1), and  $Fr_j = U_c / \sqrt{At_j g H}$  is the Froude number which represents the ratio of inertia stress to the stresses caused by density difference. Note that  $g$  denotes the gravity acceleration and  $At_j = \frac{\rho_j - \rho_c}{\rho_c} \geq 0$  is the Atwood number, that indicates the dimensionless density differences between the  $j$ -th layer and water (upper layer).

The Péclet number,  $Pe$ , represents the advective transfer rate of a specie to its diffusive transfer rate,

$$Pe_i = \frac{H U_c}{D_i} \quad (5.6)$$

where  $D_i$  is the diffusivity parameter corresponding to  $i$ -species. It should be underlined that only the diffusion of reactive agent,  $c_1$ , is considered here. Hence, in this work we set  $Pe_{2,3,4} = \infty$ , highlighting the behaviour of a single component diffusing in a reacting system with slight density gradients. Hence, here  $Pe = Pe_1 > 0$ .

The ratio of advection time scale over the reaction time scale is represented by the Damköhler number,

$$Da = \frac{k c_{2,c}^a H}{M_2^a U_c} \quad (5.7)$$

where  $k$  is the reaction rate<sup>2</sup>,  $M_2$  is the molecular weight of the reactant component, and  $c_{2,c}$  is the reference concentration for the reactant component which is assumed to be its inflow concentration.

During this study we consider three different scenarios of three-layer flows through the Hele-Shaw cell,

- (i)  $Da = 0$ ,  $BN = 0$ ,  $Pe \sim \infty$ : Unreactive flow of 3 layers of Newtonian fluid,

---

<sup>2</sup>see Eq. (C.6) in Appendix C for more details.

- (ii)  $Da = 0$ ,  $BN > 0$ ,  $Pe \sim \infty$ : Fully-reacted flow of a viscoplastic fluid layer lubricated by 2 Newtonian fluid layers,
- (iii)  $Da > 0$ ,  $BN > 0$ ,  $Pe > 0$ : Reacting flow of 2 layers of Newtonian fluid in a 3-layer flow (with a developing gel layer).

The theoretical formulation of the problem, that explains the fluid dynamics of the flow, mass transfer and chemical reaction of the species, as well as the link between them, are detailed in Appendix C (see Sec. C.1). Note that there is an ongoing numerical study which aims to solve the governing equations of the problem. The details of the numerical approach are explained in [92].

In this research, we approach the three aforementioned cases theoretically in order to provide a comparison with the experimental findings. Simplifications have been applied to the governing equations of the problem and theoretical schemes were developed to obtain estimations for the stable flow field of the flow without reaction, and the growth of the gel layer in the reactive flow. In particular, a 1-D theoretical approach is used to predict the flow field for fully developed and stable flow regimes in the slot, oriented at different inclination angles. Besides, an idealized analytical model is used to solve for the mass transport of the species in a constant velocity field, in order to provide an estimation of the growth of the thickness of the gel layer. The details of analytical approach are discussed in Appendix C (see Sec. C.2).

### 5.3 Fluid characterisation

Aqueous suspensions of medium-viscosity alginic acid sodium salt (MP Biomedicals) contacted with  $CaCl_2$  and Carbopol (Lubrizol) contacted with  $NaOH$  provided the main working fluids in our experiments.

In particular, a solution of acidic Carbopol ( $pH \sim 3$ ) and neutral Carbopol ( $pH \sim 7$ ) with mass concentration of 0.06% are used in our experiments as the middle layer fluid in the unreactive and fully-reacted cases, respectively. For both unreactive and fully-reacted cases, we use water-sugar mixture with the density of  $1.05 \text{ g/cm}^3$  as

Case	Mixture	$c_1/c_2$	$c_2$ (w/w) %	$\tau_y$ Pa	$K$ Pa · s <sup>n</sup>	$n$
Unreacted alginate (A)	<i>CaCl</i> <sub>2</sub> /alginate	0	0.25	0	0.01	0.96
Reacted alginate (B)	<i>CaCl</i> <sub>2</sub> /alginate	0.09	0.25	0.4	0.42	0.60
Acidic Carbopol (C)	<i>NaOH</i> /Carbopol	0	0.06	0	0.004	1
Neutral Carbopol (D)	<i>NaOH</i> /Carbopol	0.29	0.06	0.2	0.39	0.57

**Table 5.1:** Herschel-Bulkley (HB) coefficients for dilute mixtures of alginate or Carbopol ( $c_1$ ) with a reacting agent ( $c_2$ ). Note that the HB parameters were obtained from the best Herschel-Bulkley fit of the Carbopol solutions with R-squared better than 0.95.

the densest fluid and pure water as the lightest fluid that form the lower and upper layer in the channel, respectively.

For the reactive experiments, we used aqueous suspensions of medium-viscosity alginic acid sodium salt and the salt solution (*CaCl*<sub>2</sub>). The salt solution was pumped toward the upper layer, while the alginate solution is pumped toward the middle layer. Similar to the two other cases, the sugar solution with the density of 1.05 g/cm<sup>3</sup> was used as the bottom layer fluid. Moreover, we added sugar to the alginate solution in order to increase its density to 1.02 g/cm<sup>3</sup> and to ensure that the configuration is density stratified at a horizontal orientation.

The rheological properties of the material were characterised using a rheometer with roughened parallel plates (AR2000, TA Instruments). The rheology for a range of mixtures (Table 5.1) were measured and fitted to the Herschel-Bulkley model. Figure 5.3 indicates the corresponding flow curves for the acidic Carbopol, and neutral Carbopol, as well as unreacted and reacted 0.25%-alginate solution.

The flow curves in Fig. 5.3 show that the yield stress and consistency index of the alginate solution increase with the addition of the reacting agent, calcium salt. The same scenario occurs for the Carbopol solution. Adding *NaOH* to the acidic Carbopol solution, neutralizing the solution, leads to an increase in the yield stress and consistency of the fluid. Knowing this, either Carbopol or alginate with con-

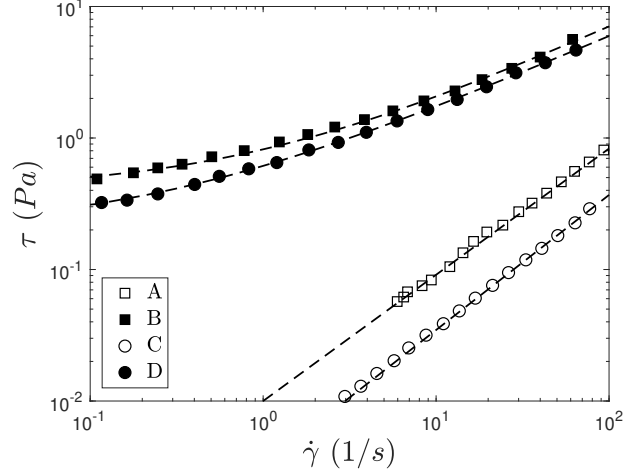


**Figure 5.3:** Flow curves for the alginate and Carbopol solutions listed in Table 5.1. The dashed lines give the Herschel-Bulkley fits in Table 5.1.

centration of  $c_2$ , and  $NaOH$  or  $CaCl_2$  with a concentration of  $c_1$ , can be considered as the reactive materials in our 4-component disperse system. Sugar with the concentration of  $c_4$  is the non-reactive component which affects the density of the fluid (see Fig. 5.1(a)).

## 5.4 Experimental details

### 5.4.1 Experimental setup

The experimental results reported in this work were obtained with a Hele-Shaw cell constructed out of an aluminium frame housing two glass panels for the walls. The cell was mounted on a 3-axis rotation stage (Thorlabs) to control the orientation of the channel within  $\pm 5^\circ$  from a horizontal alignment. Two aluminium inserts were placed in the channel to separate the working fluids before layering and the dimensions were set such that  $H/W \sim H/L \ll 1$  and the entrance length  $l_f \gg h_f$  to ensure the flow is fully developed before layering and reaction. Note that the aluminium inserts were spaced equidistant from each other so the entrance height

for each fluid stream was identical, i.e.  $h_f \sim H/3$  (see Fig. 5.1(a)).

For layered and reacting configurations, the flow of the inner and outer fluids were provided by two separate syringe pumps (KD Scientific). The experiments were initiated by first filling the channel with water and then successively introducing stream (3)  $\rightarrow$  (1) to avoid gravity currents at a horizontal orientation. Once each stream was introduced into the channel the inclination angle was set by adjusting the 3-axis stage to within  $\pm 0.1^\circ$ .

The main focus of our experimental study is on determining the flow interfaces developing in the slot. Hence,  $0.5 \mu\text{m}$  particles with the mass concentration of 0.05% were added to the middle-layer fluid. An optical coherent tomography device (OCT) was used to visualize the multi-layer flow in the channel. The OCT generated cross-sectional images of the sample, the particles and channel surface, with micrometer-scale axial and transverse resolution and millisecond temporal resolution [85]. The vertical ( $z$ -component) and lateral ( $x$ -component) field of view were approximately 3.5 mm and 5 mm, respectively. The image recording rate was 10 frames per second.<sup>3</sup> Imaging occurred over a number of small regions-of-interest and subsequently were stitched together to create a composite image of the cell. In order to exploit the OCT-imaging, the OCT-probe was tilted with respect to the ground around five degrees.

We were successful in our design and benchmarked the cell with a 5% glycerol solution with no reaction and no layering (Fig. 5.1(b)) and found good agreement to our theoretical estimates of the fully developed 1-D velocity field. Note that the OCT-PTV technique described in Sec. 4.4, has been applied to measure the velocity profile across the channel.

### 5.4.2 Experimental conditions

Experiments were performed with the working fluids listed in Table 5.1 for a range of operating conditions in unreactive, fully-reacted and reacting flows. The operat-

---

<sup>3</sup>Details of the OCT-imaging were given in Sec. 4.3.

Experiment	Stream 1	Stream 2	Stream 3	$\rho_3 - \rho_1$	$\rho_2 - \rho_1$	$Q_T$	$U_1/U_2$	$\theta$
	$c_1$	$c_2, c_3, c_4$	$c_4$	g/mL	g/mL	mL/min		
Unreactive	0	0.06,0,0	12	0.05	0	0.9	1	(-5,5)
Fully-reacted	0	0,0.06,0	12	0.05	0	0.9	0.5,1,2	(-5,5)
Reactive	0.05,0.1,0.15	0.25,0,6	12	0.05	0.02	0.9	4,16	0

**Table 5.2:** Inlet conditions for the experimental work. The brackets  $(\cdot)$  represent a range of experiments within the two bounds and all other conditions are fixed values. The stream concentrations ( $c_{1 \rightarrow 4}$ ) are all in  $(w/w)\%$  where the stream notations can be found in Fig. 5.1(a).

Experiments	$Re$	$At_3$	$BN$	$\chi_3/1000$	$m_2$	$\frac{U_{c,2}}{U_{c,1}}$	$Pe$	$Da$
Unreactive	0.31	0.05	0	-4:4	4.16	0.5,1,2	$\infty$	0
Fully-reacted	0.31	0.05	7018	-4:4	1925	0.5,1,2	$\infty$	0

**Table 5.3:** Ranges of dimensionless groups in unreactive and fully-reacted experiments. Note that the negligible difference between the density of middle layer (2) and upper layer (1), as well as that between the viscosity of the lower layer (3) and upper layer (1), imply  $At_2 \sim 0$ ,  $\chi_2 \sim 0$ , and  $m_3 \sim 1$ .

ing conditions for the experiments are listed in Table 5.2, where we only report the initial concentrations for each stream shown in Fig. 5.1(a). Note that  $Q_1 = Q_3$  for all of the experiments.

The ranges of dimensionless groups, over which the unreactive and fully-reacted experiments have been performed, are reported in Table 5.3. In these two cases, the effect of density difference between the layers on the flow patterns developing in the cell is studied by conducting the experiments at different inclination angles. Hence, both sets of experiments have been performed at a constant  $At$ -number but different values of  $\chi_3$ -numbers. In all the experiments, the Reynolds number is fixed at  $Re = 0.31$ , but the flow rate ratio changes between 0.5 to 2.

### 5.4.3 Measuring the flow interfaces

We determine the position of interfaces developing in the cell by analysing the cross sectional images generated by the OCT. An edge detection code has been applied to the OCT-images to determine the position of interfaces between three flow layers and side walls of the slot. The edge detection algorithm used here is a gradient-based technique that can detect the flow boundaries on the basis of the discontinuity in gradient of intensity along the lines perpendicular to the flow. Note that the intensity difference is caused by the back-scattered light from sub-micron particles in the middle layer.

In the case of reactive flows, a gel layer develops inside the alginate solution. The sub-micron particles were present in both reacted alginate layer and unreacted alginate layer. Hence, determining the boundary between reacted and unreacted alginate layers is more complex.

As described in [106], the possible Brownian motion of sub-micron beads within the alginate layer might lead to time variance in the interference signal resulting from the backscattered light from them. Consecutive images of the beads in the unreacted layer show significant temporal fluctuations, in the Lagrangian system moving with the local mean streaming velocity, due to their Brownian motions. However, the relatively high viscosity of the reacted layer hinders the Brownian motion of seeded beads and their consequent fluctuations. In other words, the particles trapped within the reacted layer are transferred by the macroscale flow along the channel, while those in unreacted layer fluctuate with respect to the macro-scale flow due to their Brownian motions. We exploit the sharp contrast between the degree of fluctuations in the reacted and unreacted layer in order to determine the gelled region. In this study, we quantify these fluctuations by measuring the temporal variability in the backscattered light from tracing beads over the interrogation windows moving with the same speed of the macroscopic flow. The details of the quantitative method used to predict the position of reacting front are explained in Appendix C (see Sec. C.3).

## 5.5 Results

### 5.5.1 Flow configuration

#### Effect of density difference

As mentioned before, we consider the unreactive and fully-reacted cases in order to study the possible flow regimes and instabilities that might occur under the effect of density differences at slight inclination angles. The experiments were performed for  $Re = 0.31$  to characterise the operational stability as a function of inclination angle with no reaction. We use the analytical approach, described in Sec. C.2, to characterise the stable flow structures developing at different inclination angles and inlet flow rate ratios. Furthermore, the flow patterns have been studied experimentally to identify any sign of mixing and instability at different inclination angles.

Our experimental observations confirm that the unreactive flows are unconditionally stable over the range of our experiments. A sample spatio-temporal diagram of the flow pattern across the cell, for  $Q_2/Q_1 = 1$ , and  $\chi_3 = 3000$ , is shown in Fig. 5.4(a).

Experimental and theoretical results for fully reacted case is shown in Fig. 5.5. Our theoretical findings predict three possible flow regimes that depend on the inclination angle (Regimes *I*, *II*, and *III* in Fig. 5.5(a)). The form of the velocity profile corresponding to each regime is shown in this Fig. 5.5(b). The negative velocity obtained based on the 1-D model is not physical, although it can be interpreted as the signature of recirculation in the lower or upper layer at large absolute values of  $\chi_3$ -numbers. It should be underlined that our experimental observations confirm the presence of recirculation in these regimes. Note that qualitatively similar flow regimes were predicted for the unreacted case with the difference that the velocity profile corresponding to the middle layer is not plug like any more.

As shown in Fig. 5.5(a), for the fully reacted case, our experimental observations suggest that the flow remains unconditionally stable over a wide range of



$\chi_3$ -numbers, i.e.  $\chi_3 \in [-1800, 2000]$ . But, the surprising feature of our experiments is that hydrodynamically unstable flow regimes or mixing events were observed outside of this region. It should be mentioned that these observations are in contrast with numerical simulation of the problem that predict unconditionally stable flow over the range of our experiments (see [92]). The unstable regimes are shown with hatched areas in Fig. 5.5(a). In addition, the spatio-temporal diagram of the flow pattern in stable and unstable regimes are shown in Fig. 5.5 (*i – iii*).

We observed buckling of the viscoplastic fluid where the inclination angle affects the resulting trajectory (Fig. 5.5(i) and (iii)). Similar observations have been reported for stratified and displacement flows in inclined channels, at a high Reynolds number [100]. However, to our best knowledge, there is no evidence of instability of multi-layered flow system at such a low Reynolds number, i.e.  $Re = 0.31$ . We hypothesized that this complex behaviour can be attributed to the elastomechanical response of the Carbopol to the interfacial stress caused by the recirculating fluid in upper and lower fluid stream (regimes *I* and *III* in Fig. 5.5(b)). Note that we only report certainty in the orientation up to  $\pm 0.1$  along the  $x$ - and  $y$ -axes, which may be contributing to a crossflow (component of velocity in  $y$ -direction) and the uncharacteristic behaviour in regime *III*.

Overall, the mechanism of instabilities observed in our experiments has not been understood well and a numerical solution of the problem which includes the effect of elastic behaviour of the middle layer is required to verify the hypothetical explanations described here.

### **Effect of reaction**

Our experimental results for the fully-reacted flow confirm that the flow configuration is highly sensitive to the inclination angle. In other words, the density difference between the layers destabilizes the flow at even slight inclination angles. Hence, we study the reactive flow in a horizontally oriented Hele-Shaw cell at which the unreactive and fully-reacted flows remain stable. The question we try to answer is if the reaction itself has a destabilizing effect on the flow config-

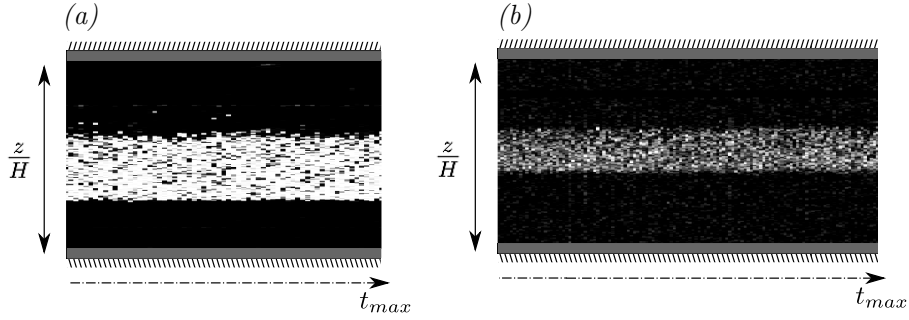


**Figure 5.4:** Representative spatio-temporal diagrams of (a) an unreactive flow ( $Q_2/Q_1 = 1$ ,  $\chi_3 = 3000$ ), and (b) a reactive flow ( $Q_2/Q_1 = 0.25$ ,  $c_1 = 0.1\%$  wt/wt,  $c_2 = 0.25\%$  wt/wt,  $\chi_3 = 0$ ). The images highlight the time evolution of the middle layer which was seeded by the tracing beads. Measurements were performed at a fixed position, as a function of time where  $t_{max}$  is 15 s in (a) and 45 s in (b). Note that the materials used for the unreactive and reactive cases were explained in Table. 5.2.

uration or not. Previous studies suggested that the fast reaction leads to a local rheology change in the fluid stream and this may cause instabilities to form [103–105]. However, our experimental observation suggests that the reactive multi-layered flow with low inertia ( $Re \sim 0.3$ ) remains unconditionally stable over a wide ranges of salt concentration and flow rate ratios, listed in Table 5.2. As an instance, the spatio-temporal plot of the reactive flow for  $Q_2/Q_1 = 0.25$ ,  $c_1 = 0.1\%$  wt/wt,  $c_2 = 0.25\%$  wt/wt, is shown in Fig. 5.4(b).

### 5.5.2 Characterising the reacting front

The next step is to determine the growth of the gelated region with reaction. In order to ensure the hydrodynamic stability of the flow system, all the following studies were done in a horizontally oriented Hele-Shaw cell (i.e.  $\chi_3 \sim 0$ ).

In the reactive process, the calcium salt diffuses from the top layer into the middle layer causing a gel transition at the interface. It should be noted that the time scale of the chemical reaction,  $t_{ch}$  is much shorter than hydrodynamic time scales of the

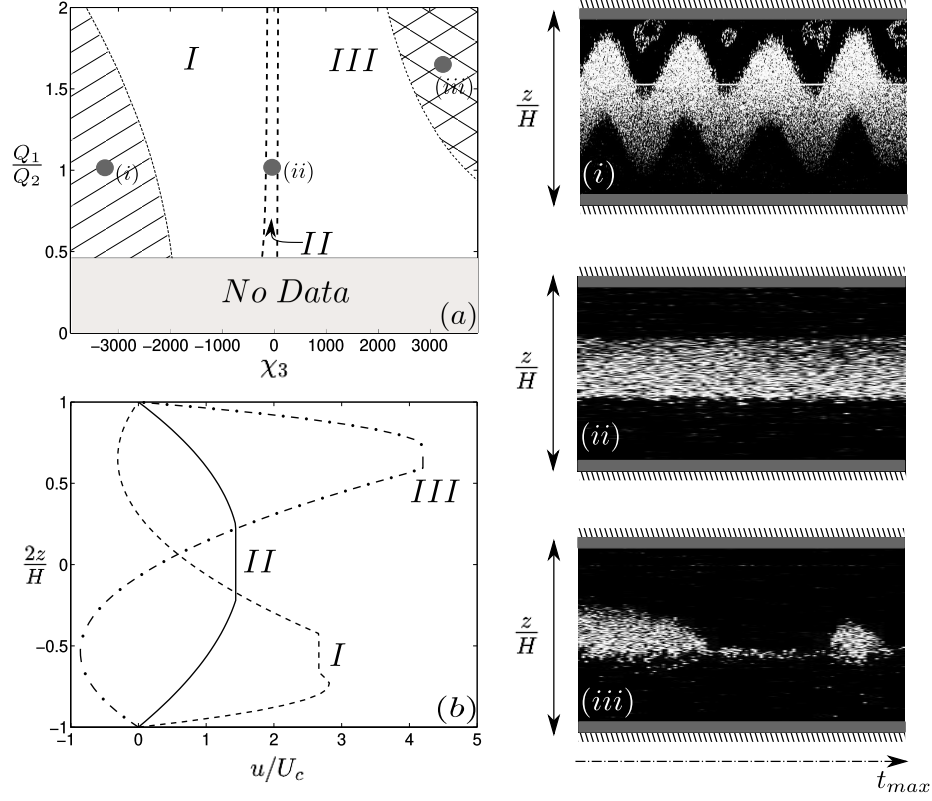


**Figure 5.5:** Representative diagrams of hydrodynamic stability of a fully reacted flow in a Hele-Shaw. (a) A representative stability diagram with complex behaviour. The data were collected with water in the upper layer (1), fully-reacted Carbopol in the middle layer (2), and a water/sugar mixture in the lower layer (3) (see Table 5.2, and Fig. 5.1). Note that  $Q_1 = Q_3$  for all of the cases shown here. Regions *I*, *II* and *III* represent the three possible flow regimes that depend on the inclination angle and the hatched areas denote unstable flow regimes. For cases (i), (ii) and (iii) we display the time evolution of the second layer, measured at a fixed position, as a function of time where  $t_{max}$  is 130 s, 15 s and 25 s, respectively. (b) Representative fully developed velocity profiles for regions *I*–*III* in (a). Note that the three flow regimes (*I*–*III*) and corresponding velocity profiles were obtained from a 1-D theoretical prediction, while the unstable regions were found by experimental observations.

problem that are the advection time, i.e.  $t_a = H/U_c$ , diffusion time, i.e.  $t_D = H^2/D$ , and viscous time, i.e.  $t_v = \rho H^2/\mu_c$ , in this problem. The average diffusion coefficient of salt in liquid alginate is assumed to be roughly  $D \sim 0.3 \text{ mm}^2/\text{s}$  [92, 107]. In addition, all our reactive experiments have been performed at the average velocity of  $0.097 \text{ mm/s}$ . Therefore, one can estimate  $t_D \sim 1700 \text{ s}$ ,  $t_a \sim 31 \text{ s}$ , and  $t_v \sim 9 \text{ s}$ , while the characteristic time scale at which reaction occurs is in the order of micro seconds. Hence, a clear separation of time scales of the problem is obtained,  $t_{ch} \ll t_v < t_a < t_D$ . Therefore, as the upper and middle fluids come into contact, the fast reaction instantaneously establishes a layer of reacted fluid at the interface with a yield stress and elevated viscosity. The fresh unreacted fluids are brought into contact at slow time scale of advection, and the reacted layer broadens diffusively at a slower time scale. In view of this, it can be assumed that the thickness of gel layer produced on the interface is dependent on the diffusive length scale of the reactive component, i.e.  $h_r \sim \sqrt{t_a D}$  [108]. We performed a series of theoretical and experimental studies to examine the validity of this assumption.

An estimation for the growth of the gel layer is obtained using the theoretical approach described in Sec. C.2. The results are reported in Fig. 5.6(a) for  $Da = 1000$ , and different values of  $Pe$ . As shown in this figure, our theoretical findings confirm that the gel layer grows linearly with the square root of distance from the layering point,  $\sqrt{x}$ .

The experimental results for the growth of the gelated region along the channel are presented in Fig. 5.6(b). The results were obtained for a fixed inlet flow rate ratio,  $Q_{1,3}/Q_2 = 4$ , and a fixed concentration of alginate,  $c_{2,c} = 0.25\% \text{ wt/wt}$ . Figure 5.6(b) represents the ratio of the thickness of the gel layer to that of channel versus the root square of the ratio of advective time scale to the diffusive time scale. According to our experimental results, an initial film of gel layer forms at the layering point. It should be noted that the numerical simulation of the problem confirms the creation of this initial layer (see [92]). We hypothesize that it might be formed due to the mixing of the fluids at the layering point. The length scale of the mixing region is much less than the height of the separation plate, which is shown by  $(\star)$  in Fig. 5.6(b). It implies that the mixing region might be the result of

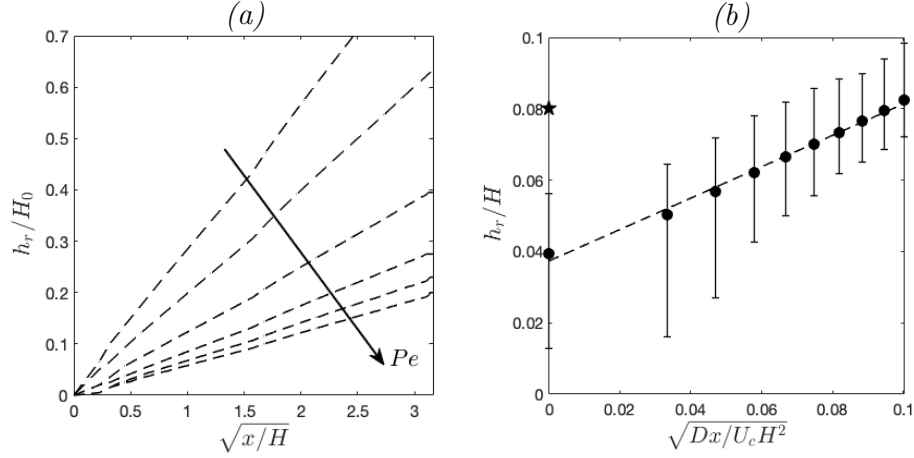


**Figure 5.6:** Growth of the gel layer  $h_r(x)$  with reaction in a Hele-Shaw cell: (a) Theoretical values obtained for the ratio of the thickness of the reacted layer over that of initial alginate layer before reaction,  $H_0$ . The results were obtained for  $Da = 1000$ , and  $Pe = 50, 100, 250, 500, 750, 1000$ . (b) Experimental results for the averaged thickness of reacted layer normalized by the thickness of the channel versus the square root of the advective time scale over diffusive time scale. The data reported in panel (b) correspond to  $Re = 0.31$  ( $Q = 0.9$  mL/min), 0.25% wt/wt-alginate, and 0.1% wt/wt-salt solution. Here, the thickness of the separation plate in the cell is presented by  $\star$ . The error in the estimate is coming from the uncertainties involved with the image processing method and was found by varying the correlation coefficient cut-off, defined in Sec. C.3, by 5%.

low inertia<sup>4</sup>. Note that the Reynolds number is very small, but not zero, and that's why a small region of mixing is formed which stabilizes quickly. After the layering point the reacted region grows diffusively and changes linearly by a square root of the distance travelled along the reactor. The thickness of the gel at the end of the reactor, therefore, is dictated by the residence time in the reactor (or the advective time scale) and the diffusion coefficient.

<sup>4</sup>According to the results obtained from the numerical simulation of the problem, there is a small velocity deficit at the trailing edge of the separation plates that leads to the creation of an initial mixing layer [92].

## 5.6 Conclusion

In this work, we addressed the scalability of the size and aspect ratio of the extrusion bioprinters, by generalizing the low inertia flow of miscible layered fluids in a Hele-Shaw cell, where chemical composition is coupled to local rheology. In order to determine an operating window for the Hele-Shaw 3D-extrusion printer, a systematic experimental study was performed to delineate the requirements that ensure the hydrodynamic stability of the flow, as well as the growth rate of the gel layer under stable flow conditions.

The vertically density stratified multi-layered flow in unreactive, fully-reacted, and reactive systems were studied in order to determine the effect of density difference between the layers at slight inclination angles and the reaction on the hydrodynamic stability of the flow. Our experimental observation showed a significant sensitivity of the flow pattern to a slight deviation from horizontal alignment, when the middle layer includes a yield stress fluid (0.06% Carbopol); i.e. instabilities have been observed at slight inclination angles. It has been well established in the literature that the yield stress is a stabilizing parameter for high Reynolds number flows [e.g. 101, 102]. However, we hypothesize that the surprising instabilities observed in this study for the fully-reacted case can be attributed to the complex rheology of the yield stress fluids, in terms of their noticeable elasticity below and around the yielding point. To move further ahead in our understanding of the mechanism of these flow instabilities, further numerical works, which are capable of modelling the complex rheological behaviour of yield stress fluids, are required. Despite these complexities, our experiments confirm the unconditional stability of the fully-reacted flow at nearly horizontal orientation, when  $-1800 < \chi_3 < 2000$ .

We investigated the reactive flow in a horizontally oriented Hele-Shaw cell, and our experimental results suggested the unconditional stability of the flow over a range of reactive-component concentrations and flow rate ratios. Despite our findings, the instability and mixing events were reported in the previous study on the reactive layered flow in a Hele-Shaw cell [105]. From the perspective of our experimental findings, we speculated that these complexities reported in the previ-

ous work [105] might be related to the significant sensitivity of such low inertia flow configurations to the density difference between the layers at slight deviation from the horizontal orientation, and not the local rheological changes caused by the chemical reaction at the interface.

We also studied the growth of the gel layer under stable flow conditions. This will assist in controlling the production of high aspect ratio materials in the Hele-Shaw printer. In agreement with our theoretical findings, our experimental measurements showed that the thickness of the gel layer grows diffusively, i.e.  $h_r/H \sim \sqrt{Pe^{-1}x/H}$ , confirming that the thickness of the recovered material is set by the advective time scale of the flow.

## Chapter 6

# Summary and conclusions

The general theme of this research is to improve our understanding of the complex features of a viscoplastic fluid flow in a thin conduit. In this thesis, we focused on the flow of a simple yield stress fluid, Carbopol, and addressed three representative flow problems in detail that encompass different aspects of viscoplastic fluid flows in confined geometries. Firstly, we examined the flow of Carbopol in an obstructed Hele-Shaw cell. Secondly, we studied the wall-slip behaviour of Carbopol gels in a fully developed capillary flow. Thirdly, we examined the reactive and stratified 3-layer flow in a horizontal Hele-Shaw cell. The methodology used to approach these problems has been mainly experimental, although in some specific cases we have also tried to provide theoretical predictions based on an idealized Herschel–Bulkley model. Comparison between the idealized theoretical findings and experimental observations provide more insight toward the flow complexities stemming from non-ideal rheological behaviour of practical viscoplastic fluids.

The present chapter is outlined as follows. The significant findings and scientific contributions of this research are reviewed in Sec. 6.1. In this section, we first summarize the main results and novel contributions made to understanding of each flow problem. Then, a description of a larger picture of our findings and the progress we made in this field is given. We wrap up the chapter with a brief description of the limitations, and possible improvements corresponding to each flow problem, as well as general recommendations for future research direction (Sec. 6.2).



## 6.1 Results and contributions

In the following section, we first summarize the significant results, insights and novel contributions regarding each flow problem. Then, the general context of this research, which clarifies the overall progress in this field, is explained.

In the first phase of this research we have provided an experimental study of the flow of Carbopol, a simple yield stress fluid, around obstructions in a thin slot. Our observations confirm that the stagnant plugs develop at the front and rear of the obstacles, and they lengthen along the flow direction by increasing the Bingham number. These results are in accordance with the theoretical findings obtained based on an idealized Herschel-Bulkley model. However, a salient feature of our experimental results is the marked fore-aft asymmetry of both the plugged regions and flow field developing around the obstruction, which contradicts the theoretical findings. The asymmetry is robust and insensitive to the shape and orientation of obstacles, to the effect of wall slip, to temporal variations in the inlet flux, and to any rheological evolution associated with flow around multiple obstacles. Previous studies indicated a similar fore-aft asymmetry for such a flow in unconfined geometries and attributed it to the viscoelastic relaxation or thixotropy of the fluid [67, 68]. Both effects appear to be minimized in the Hele-Shaw geometry, suggesting a different origin for the fore-aft asymmetry. Our experiments exhibit the signature of rheological changes of the fluid elements as they deflect around the obstacles and suggest that these changes occur over the distance of a few millimetre or time-scale of a few seconds (roughly 10 s). However, we have not observed any signs of relaxation with a similar time scale in the flow curves of the material above the yielding point. Hence, we conjecture that hysteretic rheological behaviour near the yield stress in the pseudo-plug region, and specifically a difference in the manner in which material approaches or diverges from the yield point, are responsible.

The second phase of this research was dedicated to studying the wall-slip behaviour of Carbopol gels in a pressure driven flow. To the best of our knowledge, this is the first study in this field that considered the slip velocity of Carbopol gels with different concentrations and different solvent viscosities in a Poiseuille flow. Our

results suggest that, for gently mixed Carbopol gels, the slip velocity scaled by the viscosity ratio of water and solvent is linked to the excess wall-shear stress through,  $U_s^* = f(C)(\tau_w - \tau_{SY})^{1.04 \pm 0.06}$ , where the exponent is independent of gel concentration and solvent viscosity, and the prefactor is a monotonic function of the concentration of the gel,  $f(C) = 6.23 \times 10^{-5} C^{-3.54}$ . Moreover, our experiments indicate a significant decrease in the slip velocity, when the Carbopol gel was highly stirred during its preparation. In a broader sense, the experiments show that the slip velocity is linked to the microstructure of the fluid which was varied by both the concentration of the polymer and the stirring rate during the gel preparation. Furthermore, our results confirm that there is a sliding threshold for the flow that changes linearly by the yield stress of the gel and roughly linearly by the viscosity of its solvent.

In the third phase of this research we considered low inertia and reactive 3-layer flow in a Hele-Shaw cell where the fluid layers are vertically stratified and miscible. The objective is to examine the hydrodynamic stability of the flow under different flow conditions as well as to predict the growth rate of gel layer at the interface. In this study we first considered the two asymptotic states of the reactive flow, unreactive flow and fully-reacted flow, in order to examine the effect of density difference between the layers at slight inclination angles on the hydrodynamic stability of the flow. Our experiments show that the hydrodynamic stability of such a low inertia flow is significantly sensitive to the inclination angle, in the case of fully-reacted flow (i.e. instability events observed out of  $-1800 < \chi_3 < 2000$ ). These complex events were not predicted by the numerical simulation of the problem developing based on the idealized Herschel-Bulkley model for the rheology of the fluid. We speculate that these instabilities might be linked to the elastic response of the middle layer fluid (Carbopol) to the interfacial stress caused by the recirculation in the upper or lower layer at slight inclination angles. Despite these complexities, our experiments for reactive flows in a horizontally aligned cell suggest that the fast chemical reaction *per se* does not lead to any mixing or instability over the range of our experimental parameters. In addition, our experiments confirm that the thickness of the gel layer grows diffusively, i.e.  $h_r/H \sim \sqrt{Pe^{-1}x/H}$ , under the stable flow conditions.

The three representative problems addressed in this thesis highlight the complex flow characteristics of Carbopol gels, which has widely been known as a simple yield stress fluid, in confined geometries. These complexities which are robust and significant cannot be predicted by the theoretical solutions developed based on idealized rheological models such as Bingham or Herschel-Bulkley. The disagreement between theory and experiment is connected to the deficiencies of these idealized models in describing the time dependent behaviour of Carbopol gels in terms of their hysteric behaviour near the yielding point, elastic response at low shear stresses, and apparent slip on the solid boundaries. In this context, our work clearly demonstrates the need for developing new frameworks to understand the non-ideal rheological behaviour of Carbopol gels.

## **6.2 Thesis limitations and recommendations for future work**

For each of three problems studied in this thesis, some of the limitations, which may also be considered as possible extensions are explained in the following section. In addition, an overall recommendation for future direction of the thesis is presented.

The first problem we studied in this these is the viscoplastic fluid flow in an obstructed Hele-Shaw cell. Our experimental study constrains the possible explanations for the marked fore-aft asymmetry of flow around obstructions in a Hele-Shaw cell and clarifies that the mechanism for the asymmetry in a narrow slot is rather different from those discussed in an unconfined material (elasticity or thixotropy). With our best understanding of what might be the explanation, we hypothesized that this fore-aft asymmetry can be attributed to the critical rheological behaviour of Carbopol near the yielding point, which manifests itself in the hysteresis in the flow curve. However, the nature of the hysteresis in the flow curve of the Carbopol solution and its contribution to the fore-aft asymmetrical flow around the obstacles have not been clear yet. Hence, more rheological work is required to understand the physical picture of this hysteresis and its effect on the flow. In addi-

tion to this, there are a number of other limitations and corresponding suggestions which are discussed as follows.

The current experimental setup was designed only to measure the kinematics of the flow through the cell. We could think of improvements to try to measure the pressure drop along the cell in order to determine the hydraulic resistance of the cell and the effect of fluid rheology and cell geometry on it.

Following on from the previous point, it could be interesting to equip our experimental setup with a birefringence imaging system and try to measure the stress field for the flow of an alternative yield stress fluid such as Laponite, which exhibits birefringent properties. It might bring more insight to understanding the flow features and examine some of our hypotheses including stress relaxation around the obstacles.

Moreover, due to some limitations of the experimental setup, including the limited size of the flow cell, limited range of the flow rates, limited maximum pressure in the flow cell, etc., our experiments have been performed only for Carbopol gels with low concentrations. It could be interesting to modify the experimental setup appropriately and examine if we could generalize our results for Carbopol solutions with higher concentrations or other yield stress fluids like emulsions and colloidal gels.

Our results are limited to the flow around blockages of the slot. The next step might be to investigate the flow through stepwise contractions or expansions in the slot width. Furthermore, a natural extension of the results for flow around two obstacles is to consider the flow in a more complex geometry, slot with randomly roughened walls that contains contractions and expansions. It would provide a better understanding of, first, the characteristics of non-Darcian flow in a porous medium and, second, the effect of hydrodynamic interactions of expansions and contractions on the flow configurations and stagnant regions.

The second problem we studied in this thesis is the wall-slip behaviour of Carbopol

gels in a fully developed capillary flow. Our results suggested a relationship between the slip velocity and wall-shear stress, as well as the viscosity of solvent and fluid concentration. The sensitivity of the wall-slip velocity to the gel concentration and stirring rate during its preparation implies its dependence on the microstructure of the fluid. However, we could not determine a quantitative relationship between these two parameters. To continue this study, microscopic imaging of the Carbopol structure at different concentrations and stirring rates is required to characterise a quantitative relation between the typical size of soft particles and the slip velocity.

Furthermore, the effect of surface chemistry on the wall-slip behaviour of Carbopol was not investigated in this study. Our experiments have been performed only with a glass capillary. A further step of this study would be to examine the wall slip of the gels on repulsive and attractive surfaces and investigate if a similar form of relationship for a slip velocity would be held.

The third problem that we addressed in this thesis is reactive and stratified 3-layer flow in a horizontal Hele-Shaw cell. We speculated that the hydrodynamic instabilities observed at slight inclination angles are attributed to the elastic behaviour of the material below the yielding point. However, we do not have enough evidence to examine our hypothesis and therefore the origin of instability at slight inclination angles has remained an open question. From this perspective, a systematic stability analysis is required to further investigate the root causes of these complex events. It would be interesting to extend the numerical studies to more complex rheological models that include the elastic and viscoelastic behaviour of the practical viscoplastic fluids.

In addition, our experiments for the reactive flows were operated over a narrow range of solute concentrations. It would be of value to consider the stability of the flow configuration and the effect of osmotic pressure at higher concentrations of solute and reactant. In a broader sense, this fundamental study paves the way for the extrusion bioprinters that are capable of generating large scale structures. Naturally, the next step of this study would be to investigate the functionality of extrusion process and the properties of the generated bio-structures to examine if

they meet the mechanical and functional requirements for practical use.

Overall, to continue the research presented in this thesis, further rheological work is required to characterise the dynamics of the yielding transition and temporal behaviour of the Carbopol gel near the yielding point. This will assist in developing a general model that accounts for the non-ideal rheological behaviour of the fluid as well as slip velocity near the wall. The next step would be to develop a numerical implementation of the general constitutive model in a CFD code and provide simulations of the flow problems studied in this thesis to better delineate which physical factors are responsible for the non-ideal effects observed in this work.

# Bibliography

- [1] P. Coussot. Yield stress fluid flows: A review of experimental data. *J. Non-Newtonian Fluid Mech.*, 211:31–49, 2014. → pages 2, 8, 9, 16, 70
- [2] B. Lecampion and D. I. Garagash. Confined flow of suspensions modelled by a frictional rheology. *J. Fluid Mech.*, 759:197–235, 2014.
- [3] S. H. Bittleston, J. Ferguson, and I. A. Frigaard. Mud removal and cement placement during primary cementing of an oil well–laminar non-newtonian displacements in an eccentric annular Hele-Shaw cell. *J. Eng. Math.*, 43 (2-4):229–253, 2002. → pages 3, 6, 7, 25, 31
- [4] R. Majidi, S. Miska, L. G. Thompson, M. Yu, J. Zhang, et al. Quantitative analysis of mud losses in naturally fractured reservoirs: the effect of rheology. *SPE Drill. Complet.*, 25(04):509–517, 2010.
- [5] T. Chevalier, C. Chevalier, X. Clain, J. C. Dupla, J. Canou, S. Rodts, and P. Coussot. Darcy’s law for yield stress fluid flowing through a porous medium. *J. Non-Newtonian Fluid Mech.*, 195:57–66, 2013.
- [6] T. Chevalier, S. Rodts, X. Chateau, C. Chevalier, and P. Coussot. Breaking of non-newtonian character in flows through a porous medium. *Phys. Rev. E*, 89(2):023002, 2014.
- [7] A. Roustaei and I. A. Frigaard. The occurrence of fouling layers in the flow of a yield stress fluid along a wavy-walled channel. *J. Non-Newtonian Fluid Mech.*, 198:109–124, 2013. → pages 2, 3, 6, 31
- [8] D. R. Hewitt, M. Daneshi, N. J. Balmforth, and D. M. Martinez. Obstructed and channelized viscoplastic flow in a Hele-Shaw cell. *J. Fluid Mech.*, 790:173–204, 2016. → pages xiv, xvii, 3, 21, 25, 27, 28, 32, 34, 35, 40, 42, 50, 51, 55, 57, 58, 137, 138

- [9] J. G. Savins. Non-newtonian flow through porous media. *J. Ind. Eng. Chem.*, 61(10):18–47, 1969. → pages 3, 6
- [10] F. Boyer, É. Guazzelli, and O. Pouliquen. Unifying suspension and granular rheology. *Phys. Rev. Lett.*, 107(18):188301, 2011. → page 6
- [11] M. J. Economides, K. G. Nolte, et al. *Reservoir stimulation*, volume 2. Prentice Hall Englewood Cliffs, NJ, 1989. → pages 7, 31
- [12] E. V. Dontsov and A. P. Peirce. Slurry flow, gravitational settling and a proppant transport model for hydraulic fractures. *J. Fluid Mech.*, 760: 567–590, 2014.
- [13] J. Adachi, E. Siebrits, A. Peirce, and J. Desroches. Computer simulation of hydraulic fractures. *Int. J. Rock Mech. Min. Sci.*, 44(5):739–757, 2007. → page 7
- [14] G. C. Vradis and A. L. Protopapas. Macroscopic conductivities for flow of bingham plastics in porous media. *J. Hydraul. Eng.*, 119(1):95–108, 1993. → pages 6, 7
- [15] A. K. Mirzadjanzade, Z. M. Akhmedov, R. S. Gurbanov, A. D. Amirov, G. I. Barenblatt, V. M. Entov, Y. V. Zaitsev, et al. On the special features of oil and gas field development due to effects of initial pressure gradients. In *8th World Petroleum Congress*. World Petroleum Congress, 1971. → pages 3, 7, 31
- [16] M. Cloitre and R. T. Bonnecaze. A review on wall slip in high solid dispersions. *Rheol. Acta*, 56(3):283–305, 2017. → pages xiv, 3, 16, 18, 20
- [17] S. G. Hatzikiriakos. Slip mechanisms in complex fluid flows. *Soft Matter*, 11(40):7851–7856, 2015. → page 16
- [18] S. P. Meeker, R. T. Bonnecaze, and M. Cloitre. Slip and flow in soft particle pastes. *Phys. Rev. Lett.*, 92(19):198302, 2004. → pages 3, 17, 18, 19, 20, 61, 62, 73, 75, 77, 79
- [19] J. R. Seth, M. Cloitre, and R. T. Bonnecaze. Influence of short-range forces on wall-slip in microgel pastes. *J. Rheol.*, 52(5):1241–1268, 2008. → pages xiv, 3, 17, 18, 19, 20, 61, 62, 75, 77, 79, 80, 81
- [20] M. A. Delgado, J. M. Franco, P. Partal, and C. Gallegos. Experimental study of grease flow in pipelines: wall slip and air entrainment effects. *Chem. Eng. Process. Process Intensif.*, 44(7):805–817, 2005. → page 3



- [21] X. Zhang, M. Liu, K. Bikane, and Y. Li. Evaluation of wall slip effects on the flow characteristics of petroleum coke–water slurry flow along pipelines. *Asia-Pac. J. Chem. Eng.*, 12(5):818–826, 2017. → page 3
- [22] J. R. Seth, C. Locatelli-Champagne, F. Monti, R. T. Bonnecaze, and M. Cloitre. How do soft particle glasses yield and flow near solid surfaces? *Soft Matter*, 8(1):140–148, 2012. → pages 3, 16, 19, 20, 61, 62, 74, 77, 80, 137
- [23] J. Pérez-González, J. J. López-Durán, B. M. Marín-Santibáñez, and F. Rodríguez-González. Rheo-piv of a yield-stress fluid in a capillary with slip at the wall. *Rheol. Acta*, 51(11-12):937–946, 2012. → pages 60, 63, 77
- [24] S. Aktas, D. M. Kalyon, B. M. Marín-Santibáñez, and J. Pérez-González. Shear viscosity and wall slip behavior of a viscoplastic hydrogel. *J. Rheol.*, 58(2):513–535, 2014. → pages 17, 19, 63, 73
- [25] A. Poumaere, M. Moyers-González, C. Castelain, and T. Burghelea. Unsteady laminar flows of a carbopol® gel in the presence of wall slip. *J. Non-Newtonian Fluid Mech.*, 205:28–40, 2014. → pages 15, 19, 42, 52, 60, 70, 71, 73, 77
- [26] B. Geraud, L. Bocquet, and C. Barentin. Confined flows of a polymer microgel. *Eur. Phys. J. E*, 36(3):30, 2013. → pages 3, 20, 63, 64, 65, 71, 75, 79
- [27] W. Coleman. Hydraulic fracturing disclosure: A brief comparison of state disclosure requirements, 2016. URL <http://tjogel.org>. [Online; accessed 8-May-2016]. → pages xii, 6
- [28] J. Plank. Oil well cementing, 2017. URL <http://www.bauchemie-tum.de/master-framework>. [Online; accessed 14-March-2018]. → pages xii, 6
- [29] N. J. Balmforth, I. A. Frigaard, and G. Ovarlez. Yielding to stress: recent developments in viscoplastic fluid mechanics. *Annu. Rev. Fluid Mech.*, 46: 121–146, 2014. → pages xii, xiii, 8, 11, 12, 13, 32, 33, 36, 58, 60
- [30] P. R. S. Mendes and E. S. S. Dutra. A viscosity function for viscoplastic liquids. *Ann. T. Nord. Rheol. Soc.*, 12:183–188, 2004. → page 9
- [31] D. Bonn, M. M. Denn, L. Berthier, T. Divoux, and S. Manneville. Yield stress materials in soft condensed matter. *Rev. Mod. Phys.*, 89(3):035005, 2017. → pages 9, 15, 16, 60

- [32] G. Ovarlez. Rheometry of Visco-Plastic Fluids. In G. Ovarlez and S. Hormozi, editors, *Lectures on Visco-Plastic Fluid Mechanics*, pages 127–163. Springer, 2019. → pages xiii, 10, 13, 14, 15, 36, 130, 131, 135
- [33] A. M. V. Putz and T. I. Burghilea. The solid–fluid transition in a yield stress shear thinning physical gel. *Rheol. Acta*, 48(6):673–689, 2009. → pages 10, 15, 58
- [34] G. Ovarlez and X. Chateau. Influence of shear stress applied during flow stoppage and rest period on the mechanical properties of thixotropic suspensions. *Phys. Rev. E*, 77(6):061403, 2008. → pages xiii, 11, 14
- [35] F. Caton and C. Baravian. Plastic behavior of some yield stress fluids: from creep to long-time yield. *Rheol. Acta*, 47(5-6):601–607, 2008. → page 12
- [36] T. Divoux, C. Barentin, and S. Manneville. From stress-induced fluidization processes to herschel-bulkley behaviour in simple yield stress fluids. *Soft Matter*, 7(18):8409–8418, 2011. → page 12
- [37] F. Ahonguio, L. Jossic, and A. Magnin. Influence of surface properties on the flow of a yield stress fluid around spheres. *J. Non-Newtonian Fluid Mech.*, 206:57–70, 2014. → page 14
- [38] C. Derec, G. Ducouret, A. Ajdari, and F. Lequeux. Aging and nonlinear rheology in suspensions of polyethylene oxide–protected silica particles. *Phys. Rev. E*, 67(6):061403, 2003. → page 14
- [39] P. Coussot, H. Tabuteau, X. Chateau, L. Tocquer, and G. Ovarlez. Aging and solid or liquid behavior in pastes. *J. Rheol.*, 50(6):975–994, 2006. → page 14
- [40] I. A. Gutowski, D. Lee, J. R. de Bruyn, and B. J. Frisken. Scaling and mesostructure of carbopol dispersions. *Rheol. Acta*, 51(5):441–450, 2012. → pages xiii, 14
- [41] P. H. T. Uhlerr, J. Gus, C. Tis, X. M. Zhang, J.Z.-Q. Zhou, and T.-N. Fang. The shear-induced solid-liquid transition in yield stress materials with chemically different structures. *J. Non-Newtonian Fluid Mech.*, 125(2-3): 101–119, 2005. → page 15
- [42] G. Ovarlez, S. Rodts, X. Chateau, and P. Coussot. Phenomenology and physical origin of shear localization and shear banding in complex fluids. *Rheol. Acta*, 48(8):831–844, 2009. → page 15

- [43] T. Divoux, C. Barentin, and S. Manneville. Stress overshoot in a simple yield stress fluid: An extensive study combining rheology and velocimetry. *Soft Matter*, 7(19):9335–9349, 2011. → pages 15, 36, 58
- [44] M. Dinkgreve, M. Fazilati, M. M. Denn, and D. Bonn. Carbopol: From a simple to a thixotropic yield stress fluid. *J. Rheol.*, 62(3):773–780, 2018. → pages 15, 36, 37, 58
- [45] D. M. Kalyon. Apparent slip and viscoplasticity of concentrated suspensions. *J. Rheol.*, 49(3):621–640, 2005. → pages 16, 73
- [46] V. Vand. Viscosity of solutions and suspensions. i. theory. *J. Phys. Chem.*, 52(2):277–299, 1948. → pages 16, 61
- [47] P. Lidon, L. Villa, and S. Manneville. Power-law creep and residual stresses in a carbopol microgel. *Rheol. Acta*, 56(3):307–323, 2017. → page 16
- [48] R. T. Bonnecaze and M. Cloitre. Micromechanics of soft particle glasses. *Adv. Polym. Sci.*, 236:117–161, 2010. → pages xiv, 18
- [49] A. Magnin and J. M. Piau. Cone-and-plate rheometry of yield stress fluids. study of an aqueous gel. *J. Non-Newtonian Fluid Mech.*, 36:85–108, 1990. → page 20
- [50] J. M. Piau. Carbopol gels: Elastoviscoplastic and slippery glasses made of individual swollen sponges: Meso-and macroscopic properties, constitutive equations and scaling laws. *J. Non-Newtonian Fluid Mech.*, 144(1):1–29, 2007. → pages 20, 61
- [51] M. Christel, R. Yahya, M. Albert, and B. A. Antoine. Stick-slip control of the carbopol microgels on polymethyl methacrylate transparent smooth walls. *Soft Matter*, 8(28):7365–7367, 2012. → pages 21, 138
- [52] V. Mansard, L. Bocquet, and A. Colin. Boundary conditions for soft glassy flows: slippage and surface fluidization. *Soft matter*, 10(36):6984–6989, 2014. → page 20
- [53] N. J. Jalaal, M. Balmforth and B. Stoeber. Slip of spreading viscoplastic droplets. *Langmuir*, 31(44):12071–12075, 2015. → pages 20, 21
- [54] G.M. Homsy, H. Aref, K. S. Breuer, J.W.M. Bush, C. Clanet, M. Fermigier, S. Hochgreb, J.R. Koseff, B.R. Munson, K.G. Powell, D. Quere, J.J. Riley, C.R. Robertson, A.J. Smits, S.T. Thoroddsen, and J.M. Wallace. *Multimedia Fluid Mechanics DVD-ROM*. CUP, 2008. → page 22

- [55] V.M. Entov. Analogy between equations of plane filtration and equations of longitudinal shear of nonlinearly elastic and plastic solids. *J. Appl. Math. Mech.*, 34(1):153–164, 1970. → pages 22, 25
- [56] I.C. Walton and S.H. Bittleston. The axial flow of a Bingham plastic in a narrow eccentric annulus. *J. Fluid Mech.*, 222:39–60, 1991. → pages 23, 32
- [57] N.J. Balmforth and R.V. Craster. A consistent thin-layer theory for Bingham plastics. *J. Non-Newtonian Fluid Mech.*, 84(1):65–81, 1999. → pages 23, 32
- [58] M. Danehsi, J. Mckenzie, N. J. Balmforth, , D. M. Martinez, and D. R. Hewitt. Obstructed viscoplastic flow in a Hele-Shaw cell. *Phys. Rev. Fluids*, 2019. → pages 30, 60
- [59] A. N. Beris, J. A. Tsamopoulos, R. C. Armstrong, and R. A. Brown. Creeping motion of a sphere through a bingham plastic. *J. Fluid Mech.*, 158:219–244, 1985. → page 31
- [60] A. M. V. Putz, T. Burghelea, I. A. Frigaard, and D. M. Martinez. Settling of an isolated spherical particle in a yield stress shear thinning fluid. *Phys. Fluids*, 20(3):033102, 2008. → pages 31, 32, 37, 45, 58
- [61] D. L. Tokpavi, P. Jay, A. Magnin, and L. Jossic. Experimental study of the very slow flow of a yield stress fluid around a circular cylinder. *J. Non-Newtonian Fluid Mech.*, 164(1-3):35–44, 2009. → pages 31, 32, 45
- [62] Y. Holenberg, O. M. Lavrenteva, A. Liberzon, U. Shavit, and A. Nir. PTV and PIV study of the motion of viscous drops in yield stress material. *J. Non-Newtonian Fluid Mech.*, 193:129–143, 2013. → page 37
- [63] L. Jossic, F. Ahonguio, and A. Magnin. Flow of a yield stress fluid perpendicular to a disc. *J. Non-Newtonian Fluid Mech.*, 191:14–24, 2013. → page 32
- [64] H. Ozogul, P. Jay, and A. Magnin. Nonrecirculating flow of a yield stress fluid around a circular cylinder in a poiseuille flow. *AIChE J.*, 62(12):4554–4563, 2016. → pages 31, 32
- [65] O. G. Harlen. The negative wake behind a sphere sedimenting through a viscoelastic fluid. *J. Non-Newtonian Fluid Mech.*, 108(1-3):411–430, 2002. → pages 31, 43

- [66] M. T. Arigo and G. H. McKinley. An experimental investigation of negative wakes behind spheres settling in a shear-thinning viscoelastic fluid. *Rheol. Acta*, 37(4):307–327, 1998. → page 31
- [67] I. Cheddadi, P. Saramito, B. Dollet, C. Raufaste, and F. Graner. Understanding and predicting viscous, elastic, plastic flows. *Eur. Phys. J. E*, 34(1):1, 2011. → pages 32, 105
- [68] D. Fragedakis, Y. Dimakopoulos, and J. Tsamopoulos. Yielding the yield-stress analysis: a study focused on the effects of elasticity on the settling of a single spherical particle in simple yield-stress fluids. *Soft matter*, 12(24):5378–5401, 2016. → pages 32, 105
- [69] B. Gueslin, L. Talini, B. Herzhaft, Y. Peysson, and C. Allain. Flow induced by a sphere settling in an aging yield-stress fluid. *Phys. Fluids*, 18(10):103101, 2006. → page 32
- [70] I. Cheddadi and P. Saramito. A new operator splitting algorithm for elastoviscoplastic flow problems. *J. Non-Newtonian Fluid Mech.*, 202:13–21, 2013. → page 32
- [71] P. Saramito. A new constitutive equation for elastoviscoplastic fluid flows. *J. Non-Newtonian Fluid Mech.*, 145(1):1–14, 2007. → page 32
- [72] B. Dollet and F. Graner. Two-dimensional flow of foam around a circular obstacle: local measurements of elasticity, plasticity and flow. *J. Fluid Mech.*, 585:181–211, 2007. → page 32
- [73] S. Drost and J. Westerweel. Hele-Shaw rheometry. *J. Rheol.*, 57(6):1787–1801, 2013. → pages 34, 43
- [74] G. Ovarlez. Rheology of visco-plastic suspensions. In *Lectures on Visco-Plastic Fluid Mechanics*, pages 165–194. Springer, 2019. → page 37
- [75] S. Hormozi, D. M. Martinez, and I. A. Frigaard. Stable core-annular flows of viscoelastic fluids using the visco-plastic lubrication technique. *J. Non-Newtonian Fluid Mech.*, 166(23-24):1356–1368, 2011. → pages 37, 39
- [76] M. Daneshi, A. Pourzahedi, D. M. Martinez, and D. Grecov. Characterising wall-slip behaviour of carbopol gels in a fully-developed poiseuille flow. *J. Non-Newtonian Fluid Mech.*, 269:65–72, 2019. → pages 42, 60

- [77] E. Chaparian and I. A. Frigaard. Cloaking: Particles in a yield-stress fluid. *J. Non-Newtonian Fluid Mech.*, 243:47–55, 2017. → page 47
- [78] E. Chaparian, A. Wachs, and I. A. Frigaard. Inline motion and hydrodynamic interaction of 2d particles in a viscoplastic fluid. *Phys. Fluids*, 30(3):033101, 2018. → page 55
- [79] A. Pourzahedi. *Rheo-PTV analysis of complex fluids*. PhD thesis, University of British Columbia, 2018. → page 60
- [80] A. J. Liu and S. R. Nagel. Nonlinear dynamics: Jamming is not just cool any more. *Nature*, 396(6706):21, 1998. → page 60
- [81] V. Trappe, V. Prasad, L. Cipelletti, P. N. Segre, and D. A. Weitz. Jamming phase diagram for attractive particles. *Nature*, 411(6839):772, 2001. → page 60
- [82] G. Benmouffok-Benbelkacem, F. Caton, C. Baravian, and S. Skali-Lami. Non-linear viscoelasticity and temporal behavior of typical yield stress fluids: Carbopol, xanthan and ketchup. *Rheol. Acta*, 49(3):305–314, 2010. → page 61
- [83] P. Coussot, L. Tocquer, C. Lanos, and G. Ovarlez. Macroscopic vs. local rheology of yield stress fluids. *J. Non-Newtonian Fluid Mech.*, 158(1-3): 85–90, 2009. → page 70
- [84] T. Divoux, D. Tamarii, C. Barentin, S. Teitel, and S. Manneville. Yielding dynamics of a herschel–bulkley fluid: a critical-like fluidization behaviour. *Soft Matter*, 8(15):4151–4164, 2012. → pages 61, 70
- [85] R. A. Leitgeb, R. M. Werkmeister, C. Blatter, and L. Schmetterer. Doppler optical coherence tomography. *Prog. Retin. Eye Res.*, 41:26–43, 2014. → pages 66, 67, 93
- [86] F. Scarano and M. L. Riethmuller. Advances in iterative multigrid piv image processing. *Exp. Fluids*, 29(1):S051–S060, 2000. → page 69
- [87] B. Rabinowitsch. Über die viskosität und elastizität von solen. *Z. Phys. Chem.*, 145(1):1–26, 1929. → page 70
- [88] D. I. Wilson. Industrial Applications of Yield Stress Fluids. In G. Ovarlez and S. Hormozi, editors, *Lectures on Visco-Plastic Fluid Mechanics*, pages 195–259. Springer, 2019. → page 73

- [89] H. S. Tang and D. M. Kalyon. Time-dependent tube flow of compressible suspensions subject to pressure dependent wall slip: Ramifications on development of flow instabilities. *J. Rheol.*, 52(5):1069–1090, 2008. → page 75
- [90] R. Borrega, M. Cloitre, I. Betremieux, B. Ernst, and L. Leibler. Concentration dependence of the low-shear viscosity of polyelectrolyte micro-networks: From hard spheres to soft microgels. *Europhys. Lett.*, 47(6):729, 1999. → page 77
- [91] H. A. Barnes. A review of the slip (wall depletion) of polymer solutions, emulsions and particle suspensions in viscometers: its cause, character, and cure. *J. Non-Newtonian Fluid Mech.*, 56(3):221–251, 1995. → page 77
- [92] T. Treskatis, J. MacKenzie, M. Daneshi, A. Wachs, and D. M. Martinez. Creating strong medical-grade hydrogel tubing through large scale 3d extrusion printing. *To be submitted*. → pages xxi, 82, 85, 86, 90, 97, 100, 101, 144
- [93] Z. J. Meng, W. Wang, R. Xie, X. J. Ju, Z. Liu, and L. Y. Chu. Microfluidic generation of hollow ca-alginate microfibers. *Lab Chip*, 16(14):2673–2681, 2016. → pages 82, 83
- [94] U. H. Pham, M. Hanif, A. Asthana, and S. M. Iqbal. A microfluidic device approach to generate hollow alginate microfibers with controlled wall thickness and inner diameter. *J. Appl. Phys.*, 117(21):214703, 2015.
- [95] K. Y. Lee and D. J. Mooney. Alginate: properties and biomedical applications. *Prog. Polym. Sci.*, 37(1):106–126, 2012.
- [96] K. M. O. Håkansson, A. B. Fall, F. Lundell, S. Yu, C. Krywka, S. V. Roth, G. Santoro, M. Kvik, L. P. Wittberg, and L. Wågberg. Hydrodynamic alignment and assembly of nanofibrils resulting in strong cellulose filaments. *Nat. Commun.*, 5:4018, 2014. → page 83
- [97] D. A. Boyd, A. R. Shields, P. B. Howell, and F. S. Ligler. Design and fabrication of uniquely shaped thiol–ene microfibers using a two-stage hydrodynamic focusing design. *Lab Chip*, 13(15):3105–3110, 2013. → page 83
- [98] J. L. Drury and D. J. Mooney. Hydrogels for tissue engineering: scaffold design variables and applications. *Biomaterials*, 24(24):4337–4351, 2003. → page 83

- [99] D. Truzzolillo and L. Cipelletti. Hydrodynamic instabilities in miscible fluids. *J. Phys. Condens. Matter*, 30(3), 2018. → page 85
- [100] K. C. Sahu, H. Ding, P. Valluri, and O. K. Matar. Pressure-driven miscible two-fluid channel flow with density gradients. *Phys. Fluids*, 21(4):043603, 2009. → pages 85, 97
- [101] M. Moyers-Gonzalez, I. A. Frigaard, and C. Nouar. Stable two-layer flows at all re; visco-plastic lubrication of shear-thinning and viscoelastic fluids. *J. Non-Newtonian Fluid Mech.*, 165(23-24):1578–1587, 2010. → pages 85, 102
- [102] S. Hormozi, D. M. Martinez, and I. A. Frigaard. Stable core-annular flows of viscoelastic fluids using the visco-plastic lubrication technique. *J. Non-Newtonian Fluid Mech.*, 166(23-24):1356–1368, 2011. → pages 85, 102
- [103] K. C. Sahu and R. Govindarajan. Linear stability of double-diffusive two-fluid channel flow. *J. Fluid Mech.*, 687:529–539, 2011. → pages 85, 98
- [104] T. Burghilea, K. Wielage-Burchard, I. A. Frigaard, D. M. Martinez, and J. J. Feng. A novel low inertia shear flow instability triggered by a chemical reaction. *Phys. Fluids*, 19(8):083102, 2007.
- [105] T. I. Burghilea and I. A. Frigaard. Unstable parallel flows triggered by a fast chemical reaction. *J. Non-Newtonian Fluid Mech.*, 166(9-10):500–514, 2011. → pages 85, 86, 98, 102, 103
- [106] M. Jalaal, C. Seyfert, B. Stoeber, and N. J. Balmforth. Gel-controlled droplet spreading. *J. Fluid Mech.*, 837:115–128, 2018. → page 95
- [107] H. Williams, M. McPhail, S. Mondal, and A. Münch. Modeling gel fiber formation in an emerging coaxial flow from a nozzle. *Journal of Fluids Engineering*, 141(1):011107, 2019. → page 100
- [108] R. B. Bird. Transport phenomena. *Appl. Mech. Rev.*, 55(1):R1–R4, 2002. → pages 100, 140
- [109] B. W. Thompson. Secondary flow in a Hele-Shaw cell. *J. Fluid Mech.*, 31(2):379–395, 1968. → page 125
- [110] G. V. L. Moisés. *The influence of thixotropy in start-up flow of yield stress fluids in a pipe*. PhD thesis, University of British Columbia, 2016. → pages 130, 131, 132



- [111] G. V. L. Moisés, L. S. Alencar, M. F. Naccache, and I. A. Frigaard. The influence of thixotropy in start-up flow of yield stress fluids in a pipe. *J. Petrol. Sci. Eng.*, 171:794–807, 2018. → pages 130, 131
- [112] Y. M. Joshi, G. R. K. Reddy, A. L. Kulkarni, N. Kumar, and R. P. Chhabra. Rheological behaviour of aqueous suspensions of laponite: new insights into the ageing phenomena. *Proc. R. Soc. London, Ser. A*, 464(2090): 469–489, 2007. → pages 130, 131
- [113] J. Labanda and J. Llorens. Influence of sodium polyacrylate on the rheology of aqueous laponite dispersions. *J. Colloid Interface Sci.*, 289(1): 86–93, 2005. → page 131
- [114] G. Ovarlez, S. Cohen-Addad, K. Krishan, J. Goyon, and P. Coussot. On the existence of a simple yield stress fluid behavior. *J. Non-Newtonian Fluid Mech.*, 193:68–79, 2013. → page 135
- [115] C. E. Brennen. *Fundamentals of multiphase flow*. Cambridge university press, 2005. → page 140
- [116] A. Faghri and Y. Zhang. *Transport phenomena in multiphase systems*. Elsevier, 2006. → pages 140, 141

## Appendix A

### Appendix to Chapter 3

To keep the body of the second chapter of this thesis as coherent and concise as possible, we have moved extra material regarding the details of our experimental findings to this chapter (Appendix A). This chapter includes experimental results concerning the evolution of velocity field for the flow of a Carbopol solution along the cell containing an isolated obstacle (Sec. A.1), the details of the shape of plugged regions developing around the obstacles (Sec. A.2), the effect of rough surface of an obstacle on the plug regions (Sec. A.3), hydrodynamic interaction of the obstacles when they are oriented normal to the flow direction (Sec. A.4), as well as the characters of the flow of a thixotropic yield stress fluid (Laponite) in an obstructed Hele-Shaw cell (Sec. A.5).

#### A.1 Verification of velocity field along the channel

In order to determine the evolution of the transverse velocity field along the channel, measurements took place in ten equally spaced cross sections from  $x = -45$  mm (7.5 mm from inlet) to  $x = 45$  mm (7.5 mm from outlet). The results are illustrated in Fig. A.1. The results confirm that the fully developed flow established at the upstream and downstream of the channel.

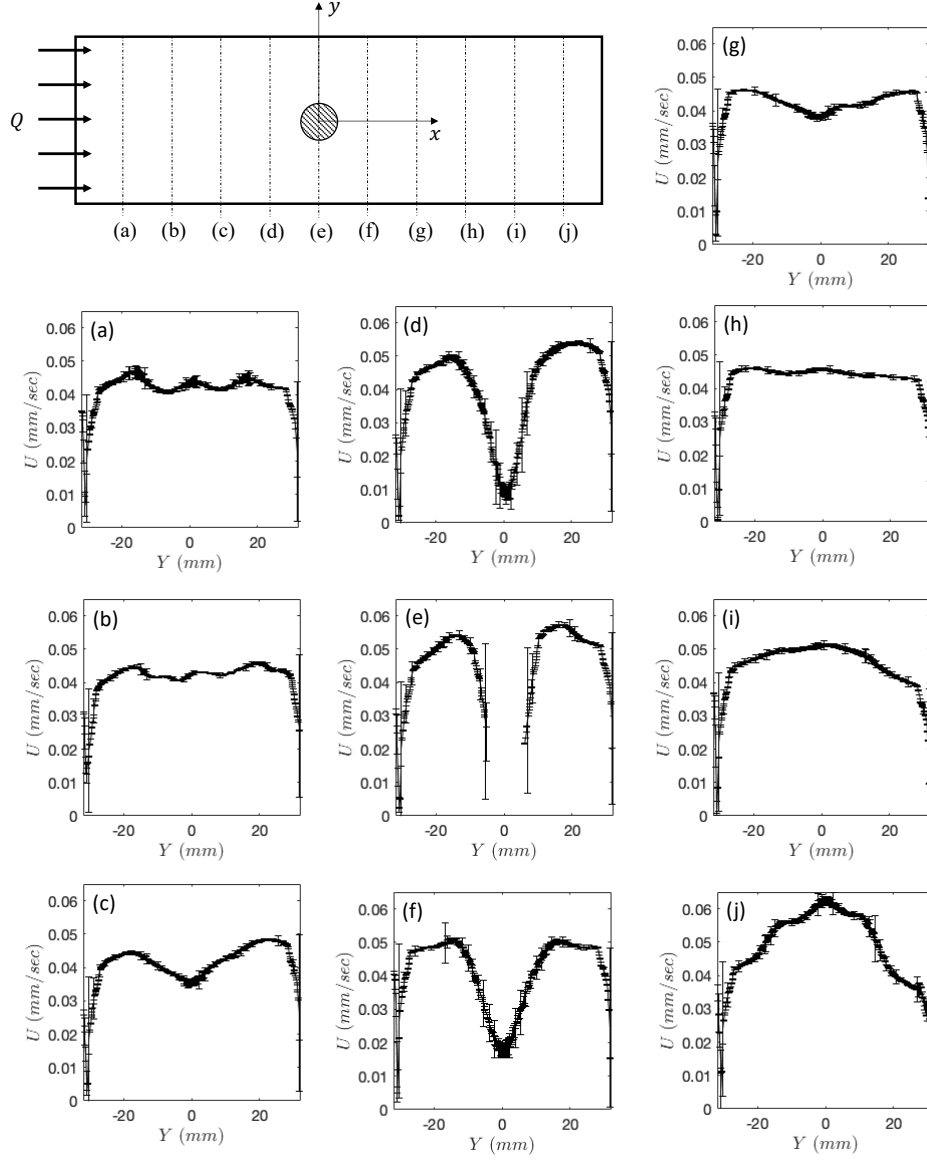


**Figure A.1:** Transverse velocity profiles measured along the width of the channel at (a)  $x = -45$  mm (7.5 mm from inlet), (b)  $x = -35$  mm, (c)  $x = -25$  mm, (d)  $x = -15$  mm, (e)  $x = -5$  mm, (f)  $x = 5$  mm, (g)  $x = 15$  mm, (h)  $x = 25$  mm, (i)  $x = 35$  mm, (j)  $x = 45$  mm (7.5 mm from outlet). Note that the velocity measurements were performed in the central horizontal plane of the cell ( $z = 0$ ).

## A.2 Shape of the rigid zones developing around the obstacles

The analysis of the static yielding surfaces developing at the front and back of the obstacles with different shapes, i.e. disk, stadium, square, and attached-disks, highlights an important feature of our findings about the shape of the rigid zones. The square root of the area of the static zones versus their orthogonal length is depicted in Fig. A.2. As clear from this figure, the square root of the area of the quasi-triangular shaped static zones is almost identical to their orthogonal plug length. It in turn indicates that the shape of static zones can be considered to be the isosceles right triangle. In other words, the average tip angle of the plugged region is close to 90 degrees. It should be noted that at large Bingham numbers, i.e.  $B > 6$ , the data slightly deviates from the line of equality and the tip angle of the plugged region becomes smaller.

Studying the static yielding surfaces developing in the front of a square shaped obstacle sheds more light on our findings. The plug regions developing in the front of a square-shaped obstacle at three different Bingham numbers, are shown in Fig. A.3. As depicted in Fig. A.3(a), for small Bingham numbers the plugged region spans a fraction of the front face of the obstacle. By increasing the Bingham number, longer and wider rigid zones form. For  $B = 6.1$ , the boundary of the upstream plugged region intersects the front face of the obstacle at its corners, see A.3(b). The interesting point is that at larger Bingham numbers the front face of the obstacle remained entirely hidden within the shadow of stagnant region, while it lengthens more in the flow direction, see Fig. A.3(c). In addition, the shape of the plugged region is more like a wedge than a triangle. It confirms that at large Bingham numbers the average tip angle of the plugged region decreases from right angle and the wedge-shape plug forms that elongates in the direction of the flow. Therefore, it can be hypothesized that at the limit,  $B \rightarrow \infty$ , the obstacle plugs the flow at a long strip in its front and back that spans the entire width of the obstacle perpendicular to the flow.

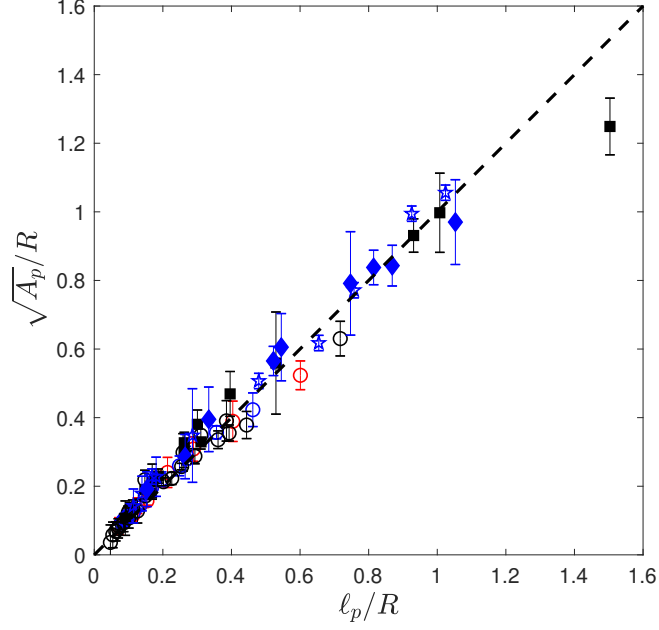


**Figure A.2:** The normalized square root of the area of the stagnant regions,  $\sqrt{A_p}/R$ , versus the normalized orthogonal plug length,  $\ell_p/R$ . The symbols used in this figure are similar to those defined in the legend of Fig. 3.8. The dashed line represents the equality line.

### A.3 Effect of surface properties of the obstacle

It is interesting to examine the effect of the slip-condition at the edge of the obstacles. All tests reported in Chapter 3 were done with obstacles with quite smooth edge that provides wall slip for the flow of Carbopol gels on them. The theoretical solution of the problem is developed based on the Hele-Shaw model (see Sec. 2.3). The Hele-Shaw model is an asymptotic theory, in which the tangential velocity condition on the obstacle plays no role on the leading-order solutions [109]. Note that the Hele-Shaw model cannot be used to predict the flow near the obstacle and holds valid only in the outer region, where  $(\frac{\partial^2}{\partial z^2} \gg \frac{\partial^2}{\partial x^2} + \frac{\partial^2}{\partial y^2})$ . Hence, the tangential slip condition on the obstacle has no effect on the plug size as long as the Hele-Shaw model applies. If the plug length is comparable to the depth of the channel

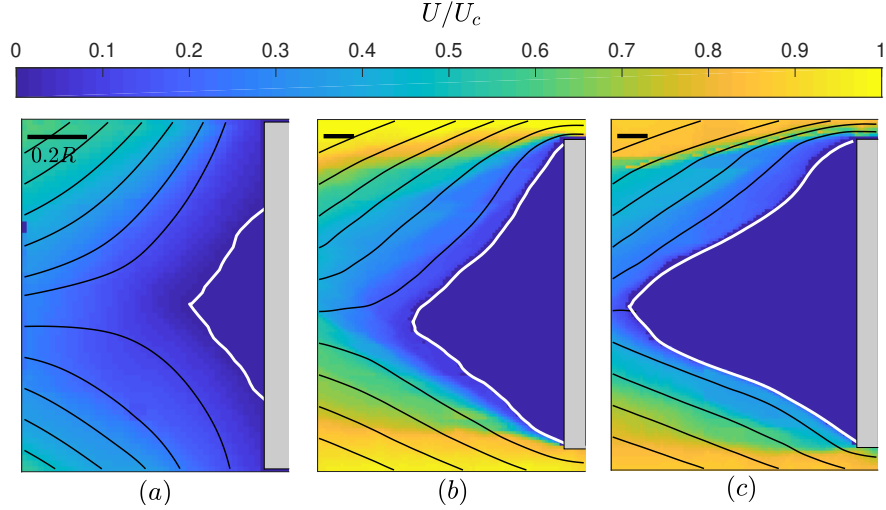


**Figure A.3:** The speed contours of the flow in the upstream of a square shaped obstacle are shown for (a)  $B = 1.07$ , (b)  $B = 6.10$ , (c)  $B = 10.41$ . The results were obtained for the flow of 0.06% Carbopol in a channel with untreated sheets. The obstacle is indicated by a gray box in the images. The scale-bar on the images represent  $0.2R$ .

then the Hele-Shaw model does not apply, so the tangential condition on the obstacle might become important. But in general it is hard to say what the effect of slip would be in this limit; one might imagine that slip on the obstacle would give a smaller plug because the fluid can somehow slide around the obstacle, but it is not obvious and evidenced. In fact, an inclusive 3d-numerical simulation of the problem is required to determine the effect of tangential slip condition on the obstacle, which is beyond the scope of the current study.

We performed a series of experiments to examine the effect of slip-condition on the edge of the obstacle, in particular, on the length of plug regions developing at its upstream and downstream. The 0.06%-Carbopol gel is used as the working fluid in our experiments. The tests were carried out for both a magnetic disk with quite smooth edge and a disk with rough edge cut from a plastic rubber. An elementary inspection of the surface texture of the rough disk using a Confocal microscope

and a 10-X objective lens, proved the presence of random roughness pattern on the edge of the obstacle with a characteristic length in the order of 50-500  $\mu m$ .

The lengths of the plugged regions developing around both smooth and rough obstacles are reported in Fig. A.4 for different Bingham numbers. The results show noticeable fore-aft asymmetry in the plug regions for the disk with rough edge surface, unless it is weaker in comparison with that obtained for a smooth disk. Note that the plug length developing in the front of the obstacle is not sensitive to the surface properties of the obstacle. However, the size of the rigid zone downstream of the obstacle is systematically larger for the obstacle with rough edge. The no-slip condition on the obstacle edge necessitates the gel to be sheared over the obstacle at a higher shear rate. From the rheological perspective, one might speculate that changing the shear history of the fluid around the obstacle might affect the flow at the downstream of the obstacle.

#### **A.4 Obstacles normal to the flow direction**

In this section, we consider the flow configuration around obstacles arranged perpendicular to the incident flow. The results obtained for the cases of attached and detached obstacles are reported in Fig. A.5. As indicated in Fig. A.5(a), when the obstacles are attached together, a large plugged region develops in the front and back of the obstacles, that spans the cavity between the them. It can be attributed to the relatively wide cross section of the attached circles that is two times greater than that of an isolated obstacle. However, when the obstacles are detached, they interact with the flow differently (Fig. A.5(b)). In this case, the obstacles channel the flow into the gap between them at a relatively high flux. Similar to what was indicated for an isolated obstacle, the plugged regions form in the front and back of these obstacles, with the difference that the rigid zones are tilted toward the horizontal line of symmetry between them. This can be caused by the different flux on the top and bottom of each disk. It should be mentioned that the lengths of these plugs are a few percent smaller than if the obstacles are isolated. Therefore, arranging the detached obstacles perpendicular to the flow has a relatively minor effect on the shape and size of plugged rigid zones. In addition, these results ex-

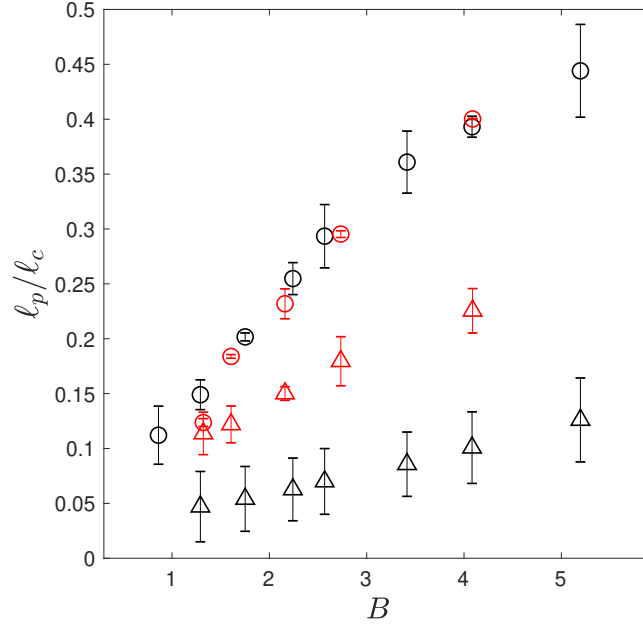


**Figure A.4:** A comparison of the scaled plug length for the flow of 0.06% Carbopol around a disk with a smooth surface (black symbols) and a disk with a rough surface (red symbols). The circles and triangles represent the length of the front plug and the rear plug, respectively.

hibit a weaker fore-aft asymmetry of the plugged regions in comparison with those predicted for an isolated obstacle (see Fig. 3.8).

Comparing the flow pattern developing in the cases of attached and detached obstacles brings us to the question whether the large plugged regions developing in the front and back of the attached obstacles and its consequent resistance against the flow might shrink just by separating the obstacles by a small distance. In order to answer this question, we positioned the obstacles at a narrow separation distance,  $L = 2.1R$ , and calculated the local flow rate between the obstacle. The 3d-velocity profile between the obstacles has been obtained by combining the velocity data measured for 20 planes equally spaced between top and bottom sheets of the channel and the local flow rate was calculated by integrating the 3d-velocity field over



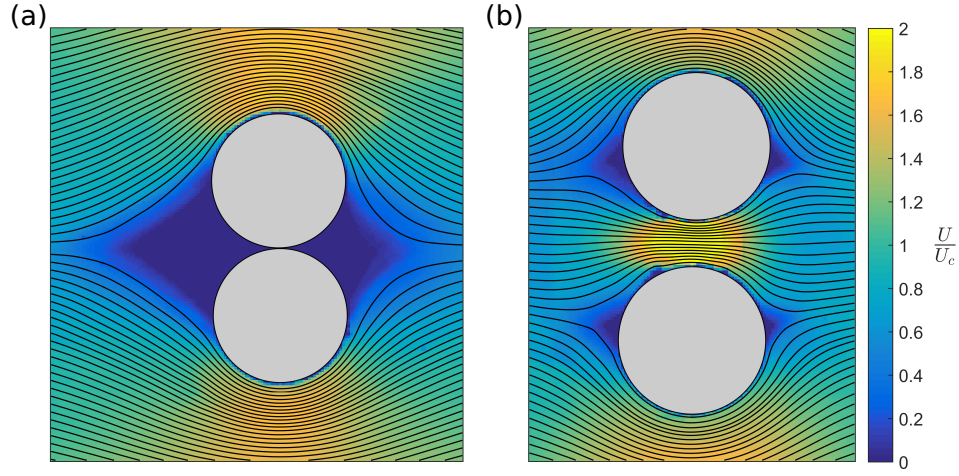


**Figure A.5:** Contours of the velocity magnitude for the flow of 0.06% Carbopol around two disks arranged normal to the flow direction, and positioned at different separation distances : (a)  $L = 2R$ , and (b)  $L = 2.5R$ . The Bingham number is fixed at  $B = 2.7$ .

the depth of the channel and distance between the obstacles. Figure A.6 indicates the ratio of average velocity between the obstacles ( $U_m$ ) and average velocity at the upstream of the channel, with respect to the Bingham number. As indicated in this figure, at small Bingham numbers,  $B < 3$ , the obstacles channelizes the flow into the gap between them at a higher local flux, i.e.  $U_m/U_c > 1$ . However by increasing the Bingham number, the ratio shrinks to less than one and the contribution of flow rate between the obstacles to the total flow rate decreases. The interesting point is that, even at very large Bingham numbers, the gap between the obstacles remains open to the flow.

## A.5 Flow of a thixotropic fluid (Laponite) along an obstructed Hele-Shaw cell

In contrast with simple yield stress fluids, thixotropic yield stress fluids exhibit a

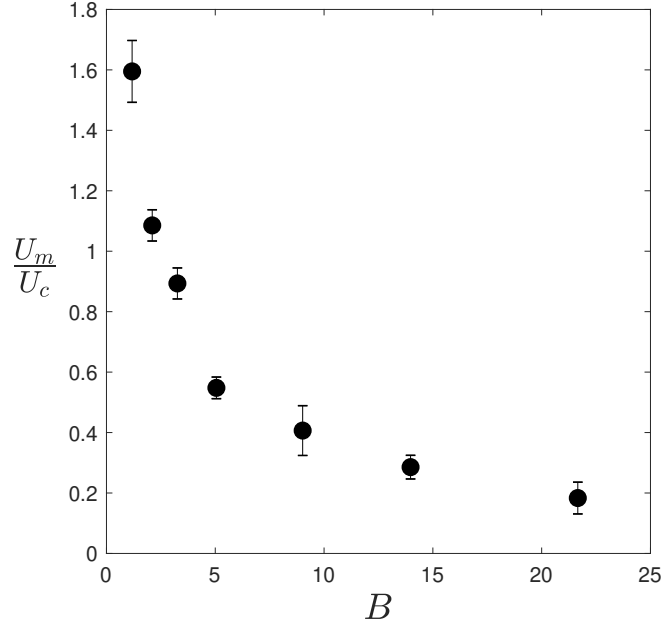


**Figure A.6:** Ratio of average velocity between obstacles,  $U_m$ , over the average velocity at the upstream of the cell, for different Bingham numbers. The results were obtained for the flow of 0.06% Carbopol around two disks oriented normal to the flow direction and separated by  $L = 2.1R$ .

shear-history-dependent behaviour. The objective of the study presented in this section is to investigate the effect of history-dependent rheology of these fluids on their flow in an obstructed slot. For this reason, we used an aqueous suspension of Laponite (Rockwood) which is widely known as a transparent thixotropic fluid. The rheological behaviour of the Laponite suspension at different concentrations and ionic strengths, in terms of its shear-dependent properties and transient responses, has been studied in the literature, recently [32, 110–112]. The viscoelastic behaviour of the material below the yielding point and its shear-thinning behaviour above the yielding point have been evidenced in previous studies [110, 111]. With regard to the transient behaviour of the material, it has been shown that elastoplastic properties of the material exhibit significant ageing; namely, as the material rests, its static yield stress spontaneously increases and tends to an asymptote [32, 110, 111]. Then, if the material experiences a high shear flow, its viscosity

decreases by time until it reaches a steady state value. If it subsequently is subjected to a low shear flow, the structure of the fluid evolves and it thickens by the passing of the time [32, 110, 111]. The question we try to answer qualitatively is how the time-dependent behaviour of this fluid influences the flow in an obstructed slot.

For this study, a Laponite suspension (with Laponite concentration of  $1.25\text{ wt\%/wt\%}$  and NaCl-concentration of  $0.005\text{ mol/L}$ ) was prepared following the protocol detailed in [110–112]. It should be underlined that during the preparation, the sample was mixed using the propeller mixer for  $48\text{ hr}$  and at  $300\text{ rpm}$  in order to get a homogeneous suspension. At the end, the suspension was preserved in a closed bucket and left it at rest for 7 days before running the experiments, for initial ageing. In fact, the ageing period of the Laponite suspension can be as long as one year [110, 113]. However, significant build-up of its microstructure and consequently major change in the rheology of the fluid are expected to occur during the first week [110, 113].

Before running the experiments, tracing particles were added to the fluid sample contained in a glass beaker following the procedure described in Sec. 3.2. Next, the fluid sample is vigorously mixed with a magnetic stirrer at  $500\text{ rpm}$  and for  $1\text{ hr}$ , in order to obtain a reproducible initial state. Then, we filled the syringes, used for injecting the fluid into the channel, with the pre-sheared material and left them at rest for  $3\text{ hr}$ .

In the first phase of this study, we examine the flow of Laponite around an isolated disk. As reported in [110], the rheological properties of Laponite suspension and in particular its static yield stress is strongly dependent on the shear history and resting time. Knowing this, we designed a start-up flow experiment to investigate the effect of thixotropic behaviour of the fluid on the evolution of plug region developing around an obstacle. Different stages of the experiment are presented in Fig. A.7(a). First the connecting tube and the channel are filled with the fluid at a high flow rate,  $Q = 10\text{ mL/min}$  (*first stage*). Then the fluid is left at rest for  $10\text{ min}$  (*second stage*). After the resting period, the flow is driven at a low flow rate,  $Q = 1\text{ mL/min}$ , and the plug region developing in the front of the obstacle

is monitored (*third stage*). Note that during the first stage, the fluid is pre-sheared at a high rate along the connecting tube. Besides, the inlet manifold provided an extra vigorous pre-shearing of the fluid, before it is sheared in the slot. It should be underlined that wall-shear rate along the connecting tube is three times greater than that along the slot.

The evolution of plug length by time is reported in Fig. A.7(b). As indicated in this figure, the plug evolves as time goes by and eventually tends to a steady state value. The rapid increase in the plug length occurs when  $0 < t < t_{1,cr}$ , during which the fluid rested in the channel is replaced by the fluid rested in the pipe. The fluid rested in the channel has the history of being sheared along the tube and the inlet manifold during the first stage. In addition, the plug region grows gradually over  $t_{1,cr} < t < t_{2,cr}$ , during which the fluid in the connecting tube and the half of the channel ahead of the obstacle is replaced by the fresh fluid from syringes. For  $t > t_{2,cr}$ , the steady state condition is achieved and the length of plug region remains constant.

Gustavo et al. [110] studied the shear-history dependent behaviour of Laponite suspensions in an start-up experiment and showed that the pre-shearing of the fluid before rest leads to a significant decrease in the apparent yield stress. Knowing this, it can be assumed that during the last stage of our experiment (constant flow at a low rate  $Q = 1$  mL/min), the yield stress of the material approaching the leading edge of the obstacle increases and consequently the plug lengthens along the flow direction, until the whole fluid ahead of the obstacle both in channel and connecting pipe is replaced by fresh fluid from the syringe pump. In other words, the shear-history dependence of the yield stress of the fluid manifests itself in the growth of plug length by time.

The streakline images of the flow near the front and back of the obstacle and at the steady state condition are shown in Fig. A.8. Similar to what was reported for the simple yield stress fluid in Chapter 3, the results for Laponite present striking fore-aft asymmetry of the flow around the obstacle.

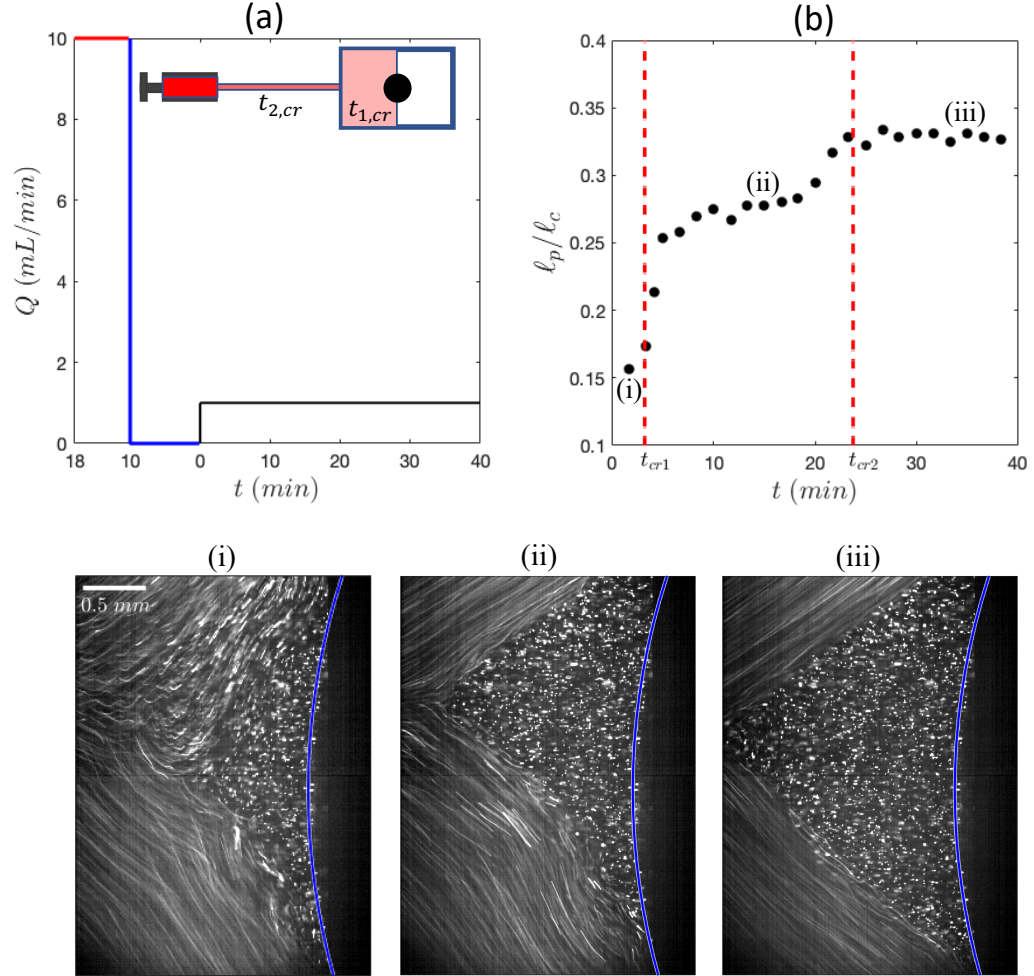


**Figure A.7:** Time dependency of the plug size on the front of an isolated disk subject to the flow of 1.25% Laponite at the constant flow of  $Q = 1$  mL/min followed by a period of 8 min pre-shearing at a high flow rate ( $Q = 10$  mL/min) and a 10 min rest period. The varied flow-rate by time test is described in panel (a). The evolution of the plug length by time is shown in panel (b). Here,  $t_{cr1}$  and  $t_{cr2}$  represent the time-span during which the pre-sheared fluid in the channel and the connecting tube are replaced by the fresh fluid, respectively. The average images of the flow in the front of the disk are shown here for three cases (i)–(iii).

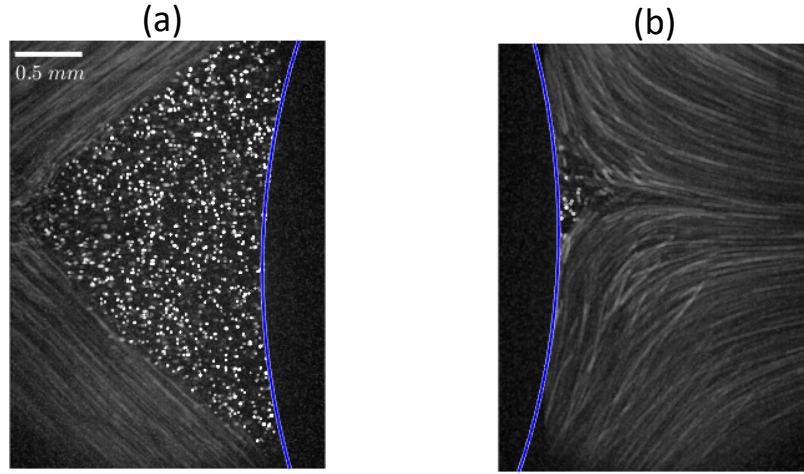


**Figure A.8:** An average image of flow of tracing particles in 1.25% Laponite near the (a) front, and (b) back of a disk. The images were obtained after running the test at a constant flow rate of  $Q = 1$  mL/min for around 35 min. Here the blue line indicates circumference of the obstacle.

Another interesting feature of the flow of Laponite around the obstacle is the discontinuity of velocity field at the static yielding surfaces. In order to provide a quantitative understanding of this phenomenon, we compare the velocity profile across the yielding surfaces for two steady state cases: flow of Laponite and flow of 0.075% Carbopol around a disk. We calculated the velocity profile along a number of lines perpendicular to the static yielding surface (see inset of Fig. A.9). A PTV-technique that provides high resolution in space, was exploited to calculate the velocity profile across the yielding surface.

The velocity profiles across the static yielding surfaces for both Laponite and 0.075% Carbopol are illustrated in Fig. A.9). As expected, in the case of 0.075% Carbopol, the velocity profiles tend smoothly toward zero at the static yielding surfaces. However, in the case of Laponite, approaching the yielding surface from the flow region, the velocity profiles tend to a finite value and a clear discontinuity is observed in the interface between the static region and flow region. From theory (see Sec. 2.3), we know that the velocity magnitude in the mid-plane of the cell

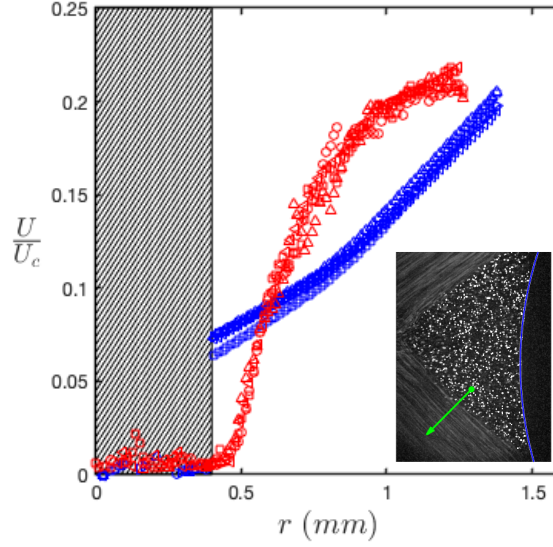


**Figure A.9:** The steady state velocity profiles along a series of lines crossing the static yielding surfaces perpendicularly (see green axis in the inset). The blue symbols and red symbols correspond to a flow of 1.25% Laponite, and a flow of 0.075% Carbopol, respectively. For both cases the flow rate was fixed at  $Q = 1$  mL/min.

is linked to the wall-shear rate. In this context, the discontinuity of the velocity profiles at the static yielding surface can be considered as a signature of the phenomenon of ‘viscosity bifurcation’; i.e. thixotropic materials cannot flow steadily at shear rates below a critical value,  $\dot{\gamma}_c$ . By contrast, for a simple yield stress fluid as the shear stress tends to the yield stress, the shear rate goes to zero [32]. Note that recent studies on the rheology of thixotropic yield stress fluids, confirm the discontinuity of the shear rate at the interface between the unyielded and yielded region and consequently existence of the shear-banding, in a simple shear flow (couette flow) [32, 114].

In the second phase of this study, we consider the flow of Laponite around two disks aligned with the flow direction. The images of streaklines of the flow near the front and back of the obstacles are illustrated in Fig. A.10, for a specific separation distance ( $L = 4.5R$ ). The noticeable feature of the flow is its fore-aft asymmetry

around both upstream and downstream obstacles. The flow between the obstacles is intuitively slower than that at the upstream of the channel. That's why the plug regions developing around the downstream obstacle are larger than corresponding ones developing around the upstream obstacle.

From the lagrangian point of view, this experiment can be considered as a suitable framework for studying the effect of the thixotropic behaviour of the fluid on the hydrodynamic interaction of the obstacles. In order to determine the effect of thixotropy, we should place the obstacles at a longer separation distance such that the flow between the obstacles is fully developed. One might expect that the thixotropic behaviour of the fluid manifests itself in the difference between the plug regions developing around the upstream and downstream obstacles. However, the dimensions of the channel used in our experiments were limited. Hence, the next step might be to use a longer channel and study the flow around obstacles positioned at a longer separation distance.

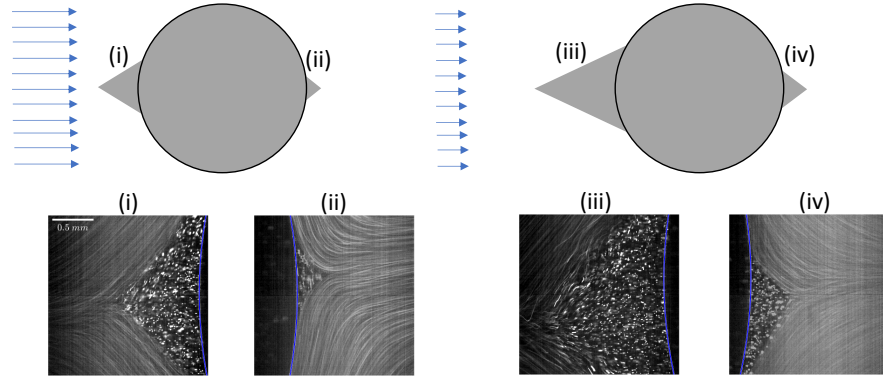


**Figure A.10:** Images of streaklines of the flow of 1.25% Laponite around two obstacles aligned with the flow direction. The images show the flow of tracing particles near (i) the leading edge and, (ii) trailing edge of the upstream obstacle, as well as (iii) the leading edge and (iv) trailing edge of the downstream obstacle. The images were obtained after running the test at  $Q = 1.2$  mL/min for 5 min followed by preshearing at  $Q = 4$  mL/min for 4 min.



## Appendix B

### Appendix to chapter 4

The wall-slip behaviour of viscoplastic fluids coupling to their yielding behaviour makes their flows in confined geometries more complex. In this section we present some experimental results that highlight the significance of the effect of wall slip on the flow of viscoplastic fluids in confined geometries.

In the third chapter of this thesis we studied the flow of a viscoplastic fluid in an obstructed Hele-Shaw cell. The obstructed Hele-Shaw cell can be considered as a simple geometry model to study a number of geophysical and industrial problems that concern the flow of a viscoplastic fluid in a non-uniform slot. The main feature of this type of flow is the appearance of stagnant or plugged regions which significantly influence the flow configuration and pressure drop along the slot. As described in [8], the flow ceases when the wall-shear stress is below a threshold, which is yield stress in the case of no-slip condition at the walls. With the presence of wall slip, the threshold for the flow is dependent not only on the rheology of fluid but also on the solid-fluid interactions on the shearing surfaces (see Fig. 4.5). The physical and chemical properties of the shearing surfaces influence the wall slip and consequently the sliding yield stress [22]. In real physical applications, the assumption of ideally uniform surface properties in terms of roughness or chemical composition seems to be unrealistic. It can be hypothesized that the non-uniformity of the surface properties leads to the variation of sliding threshold on the surface. The question raised here is how significant the effect of the non-uniform distribu-

tion of surface properties is on the flow configuration in the slot.

In order to answer this question, we visualized the flow of a viscoplastic fluid, 0.075% Carbopol, in a thin unobstructed channel with the depth of 1 mm, that was constructed from two acrylic sheets with dimensions of 100 mm×64 mm. A schematic image of the cell is shown in Fig. B.1(a). The inner surface of each plate except for a small area in its middle (shaded area in fig. B.1(a)) was chemically treated in order to minimize the wall slip, following the procedure introduced in [51]. A swept field confocal microscope equipped with a 4X-objective lens was used to visualize the flow of 3 $\mu$ m tracing particles dispersed in the Carbopol gel. The position of the observation plane was fixed on the central horizontal plane of the cell. A syringe pump is used to introduce working fluid at a constant flow rate  $Q = 0.16$  mL/min. Our objective is to determine the flow pattern over an area of 40mm×40mm in the middle of channel (see Fig. B.1(a)).

The speed contour of the flow, which was obtained from a PIV-analysis of the images taken by the confocal microscope, is presented in Fig. B.1(b). As indicated in this figure, the Carbopol gel sticks to the top and bottom sheets except in an area in the middle of channel where the surface of the sheets was left untreated. The significant channelization of the flow into a stream in the middle of channel can be attributed to the lower sliding threshold for the flow over the untreated area. Previous work on the channelized viscoplastic flow in a Hele-Shaw cell suggests that the heterogeneous structure of the slot or obstructions can be considered as candidates for creation of the stagnant regions [8]. The present work suggests that the wall slip coupling with non-uniformity of surface properties has the potential to cause formation of plugged regions, as well.

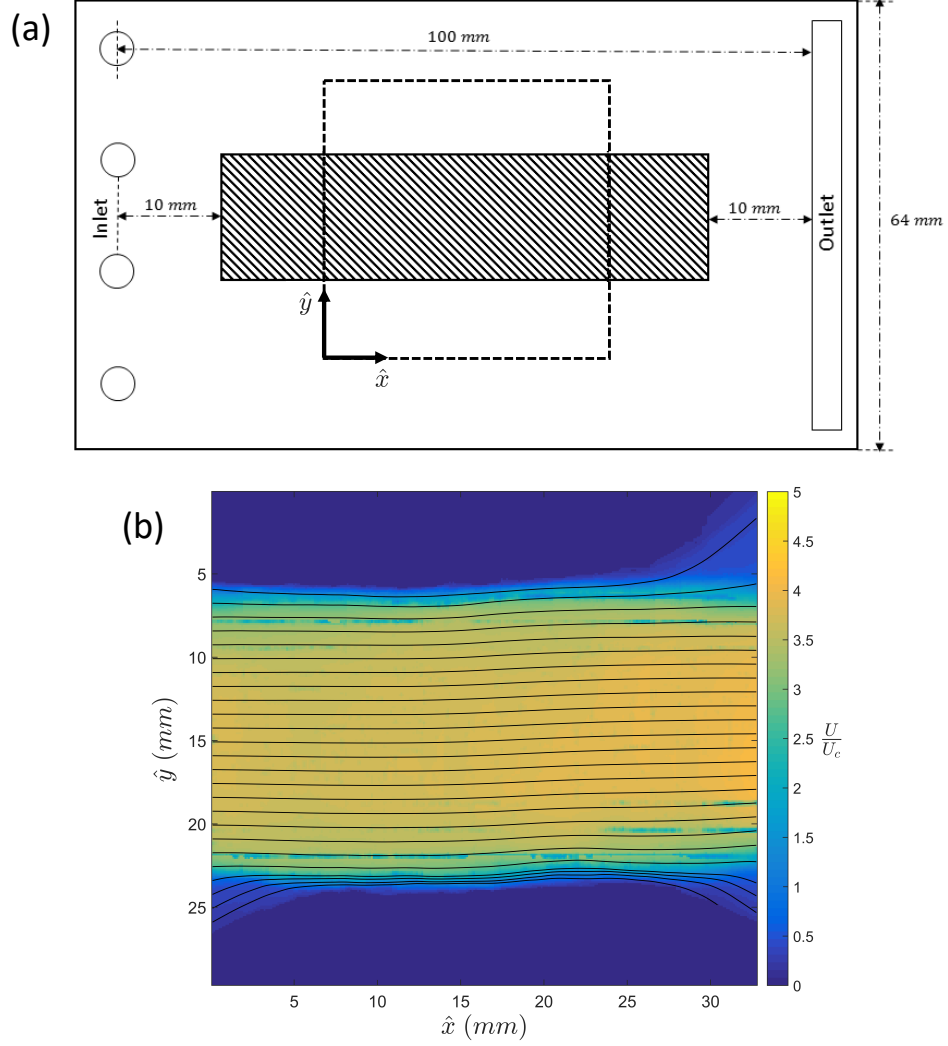


**Figure B.1:** Channelization of the flow of 0.075% Carbopol in an unobstructed Hele-Shaw cell caused by non-uniform treatment of the surface. Panel (a) represents a schematic image of the cell which was made of two acrylic plates separated by a thin gap (1 mm). The gray box represents the area on the plates which was left untreated, and the dashed box represents the observation window. Panel (b) illustrates the contour of velocity magnitude obtained for inlet flow rate of  $Q = 0.16$  mL/min.

## Appendix C

# Appendix to Chapter 5

To keep the forth chapter of this thesis short and concise, we have moved the descriptions regarding the mathematical formulation of the problem (Sec. C.1), and methodology to estimate the position of reacting front (Sec. C.3) to this chapter.

### C.1 Theoretical approach

Following on from Sec. 5.2, the mathematical formulation of the problem is detailed in the following section.<sup>1</sup> The problem can be modelled mathematically by considering several species in an aqueous solution that its properties change in space as a function of mass concentration of the species [108, 115, 116]. Under the assumption that all of the layered fluids are incompressible and in the dilute limit, the equations of motion read:

$$\frac{\partial c}{\partial t} + \nabla \cdot (cu) - \nabla \cdot (D(c)\nabla c) = r(c) \quad (\text{C.1})$$

$$\nabla \cdot u = 0 \quad (\text{C.2})$$

$$\rho(c)\left(\frac{\partial u}{\partial t} + \nabla \cdot (u \otimes u)\right) + \nabla p - \nabla \cdot \tau - \rho(c)ge_g = 0. \quad (\text{C.3})$$

where  $u$  is the velocity field;  $D$  is the diffusivity parameter;  $c$  is the mass concentration field;  $p$  is the pressure field;  $\tau$  is the deviatoric part of the (symmetric) Cauchy stress tensor;  $r$  is the rate of reaction for each species;  $\rho$  is the density,

---

<sup>1</sup>Note that we recall a number of equations and descriptions from Sec. 5.2, for convenience.

and  $g$  is the gravitational acceleration. For simplicity, the diffusion tensor  $D$  is assumed to be diagonal (and positive semidefinite). The system is closed with the Herschel-Bulkley constitutive model,

$$\begin{aligned} \tau &= \left[ K(c) \|\dot{\gamma}\|^{n(c)-1} + \frac{\tau_y(c)}{\|\dot{\gamma}\|} \right] \dot{\gamma} \quad \text{if } \dot{\gamma} \neq 0 \\ \|\tau\| &\leq \tau_y(c) \quad \text{if } \dot{\gamma} = 0, \end{aligned} \quad (\text{C.4})$$

with the strain rate  $\dot{\gamma} = (\nabla u + \nabla u^\top)$ , consistency index  $K(c)$ , flow index  $n(c)$  and yield stress  $\tau_y(c)$ . Note that  $\|\tau\| = \sqrt{\frac{1}{2} \sum_{i,j=1}^2 \tau_{ij}^2}$  denotes the Frobenius norm of a tensor field. The consistency index  $K(c)$ , flow index  $n(c)$ , yield stress  $\tau_y(c)$  and density  $\rho(c)$  are coupled to the concentration field since all of the fluids can exhibit different rheologies. The concentration dependent terms are calculated by a weighted average, shown for example as [116],

$$\mu_c^{-1} K(c) = 1 + \sum_{i=1}^N \frac{c_i K_i}{c_i} \quad (\text{C.5})$$

where  $K_i$  is the flow index of a dilute solution of  $c_i$  in water and  $N$  is the number of components in the system. We generalize the reaction scheme to a four component system ( $N = 4$ ) to compare against the experimental work and consider a chemical reaction between three species,  $c_{1-3}$  as described in Eq. (5.1),



From Eq. (5.1), the mass production rate of  $i$ -species due to the reaction,  $r_i$ , can be defined by elementary kinetics,

$$\begin{aligned} r_1 &= -k \frac{M_1}{M_1 M_2^a} c_1 c_2^a, \\ r_2 &= -ak \frac{M_2}{M_1 M_2^a} c_1 c_2^a, \\ r_3 &= bk \frac{M_3}{M_1 M_2^a} c_1 c_2^a \end{aligned} \quad (\text{C.6})$$

where,  $M_i$  is the molecular weight of  $i$ -species and  $k$  is the reaction rate, and the stoichiometric coefficients (a,b) can change depending on the type of reaction. Note that  $M_3 = (M_1 + aM_2)/b$ . The non-reactive component,  $c_4$ , introduces buoyancy into the system and hence only affects the density along the layering in Fig. 5.1. The system (C.1)-(C.5) is complemented with the following boundary conditions:

$$u = u_{\text{in}} \quad \text{on } \Gamma_{\text{in}} \quad (\text{inflow}) \quad (\text{C.7})$$

$$u = 0 \quad \text{on } \Gamma_{\text{wall}} \quad (\text{no slip}) \quad (\text{C.8})$$

$$-(\tau n) \cdot n + p = p_{\text{out}} \quad \text{on } \Gamma_{\text{out}} \quad (\text{fully developed}) \quad (\text{C.9})$$

$$u \times n = 0 \quad \text{on } \Gamma_{\text{out}} \quad (\text{fully developed}) \quad (\text{C.10})$$

$$c_i = c_{i,\text{in}} \quad \text{on } \Gamma_{\text{in}} \quad (\text{inflow}) \quad (\text{C.11})$$

$$(c_i u - D \nabla c_i) \cdot n = 0 \quad \text{on } \Gamma_{\text{wall}} \quad (\text{no flux}) \quad (\text{C.12})$$

$$\frac{\partial c_i}{\partial n} = 0 \quad \text{on } \Gamma_{\text{out}} \quad (\text{fully developed}) \quad (\text{C.13})$$

where the inflow velocity  $u_{\text{in}}$ , the outlet pressure  $p_{\text{out}}$ , and the inflow concentrations  $c_{i,\text{in}}$  were prescribed data. Note that the outlet pressure is obtained from  $\frac{dp_{\text{out}}}{dz} = -\rho(c)g$ . We set  $p_{\text{out}}(z = H/2) = p_{\text{atm}}$ , that  $p_{\text{atm}}$  denotes the atmospheric pressure.

With considering the depth of the channel,  $H$ , as the length scale of the problem, the density and viscosity of the water,  $\rho_c$ ,  $\mu_c$  as the reference density and viscosity, and the average velocity in the channel,  $U_c$  as the reference velocity, and by defining a reference value for the yield stress,  $\tau_{Y,c}$ , and a reference value for the concentration of each specie, the following scaled variables are obtained,

$$\begin{aligned} (\hat{x}, \hat{z}) &= \frac{(x, z)}{H}, \quad \hat{u} = \frac{u}{U_c}, \quad \hat{t} = \frac{t}{H/U_c}, \quad \hat{p} = \frac{p}{\mu_c U_c / H}, \quad \hat{c}_i = \frac{c_i}{c_{i,c}} \\ \hat{\tau} &= \frac{\tau}{\mu_c U_c / H}, \quad \phi_\mu = \frac{K(U_c/H)^{n-1}}{\mu_c}, \quad \phi_{\tau_Y} = \frac{\tau_Y}{\tau_{Y,c}}, \quad \phi_\rho = \frac{\rho}{\rho_c} \end{aligned} \quad (\text{C.14})$$

where  $c_{i,c}$  denotes the reference value for the concentration of  $i$ -species;  $c_{1,c}$ ,  $c_{2,c}$ , and  $c_{4,c}$  are assumed to be the inflow concentration of corresponding species. Besides, the characteristic concentration for the reacted product is assumed to be

$c_{3,c} = c_{1,c} \frac{1+aM_1/M_2}{1+a\Psi_2}$ , that  $\Psi_2 = \frac{c_{1,c}}{c_{2,c}} \frac{M_2}{M_1}$  as defined in Table C.1. Accordingly, the characteristic value for the yield stress,  $\tau_{Y,c}$ , is assumed to be the yield stress of a dilute solution of  $c_{3,c}$  in water.

Using the aforementioned scaled variables and after dropping the hat decoration, the non-dimensionalised systems of equations can be written as follows,

$$\frac{\partial c_1}{\partial t} + \nabla \cdot (c_1 u) - \frac{1}{Pe_1} \nabla \cdot \nabla c_1 = -Da c_1 c_2^a, \quad (C.15)$$

$$\frac{\partial c_2}{\partial t} + \nabla \cdot (c_2 u) - \frac{1}{Pe_2} \nabla \cdot \nabla c_2 = -aDa \Psi_2 c_1 c_2^a \quad (C.16)$$

$$\frac{\partial c_3}{\partial t} + \nabla \cdot (c_3 u) - \frac{1}{Pe_3} \nabla \cdot \nabla c_3 = bDa \Psi_3 c_1 c_2^a \quad (C.17)$$

$$\frac{\partial c_4}{\partial t} + \nabla \cdot (c_4 u) - \frac{1}{Pe_4} \nabla \cdot \nabla c_4 = 0 \quad (C.18)$$

$$\nabla \cdot u = 0 \quad (C.19)$$

$$Re \left( \frac{\partial \phi_\rho u}{\partial t} + \nabla \cdot (\phi_\rho u \otimes u) \right) + \nabla p = \nabla \cdot \tau + \phi_\rho Fe_g \quad (C.20)$$

$$\begin{aligned} \dot{\gamma} &= 0 & \|\tau\| &\leq BN\phi_{\tau_Y} \\ \tau &= \left[ \phi_\mu \|\dot{\gamma}\|^{n-1} + \frac{\phi_{\tau_Y} BN}{\|\dot{\gamma}\|} \right] \dot{\gamma} & \|\tau\| &> BN\phi_{\tau_Y} \end{aligned} \quad (C.21)$$

Regarding the above equations, the governing dimensionless parameters of the problem are listed in Table. C.1, where  $F$  represents the ratio of the gravitational force to the viscous force, the Reynolds-number,  $Re$ , indicates the ratio of inertia forces to the viscous forces, the (Newtonian) Bingham number,  $BN$ , describes the ratio of the yield stress of the fluid to the viscous stress developing in the lubricating fluids, the Damköhler number indicates the ratio of advection time scale over the reaction time scale, and the Péclet-number,  $Pe$ , represents the advective transfer rate of an specie to its diffusive transfer rate. It should be underlined that only the diffusion of reactive agent,  $c_1$ , is considered here. Hence, in this work

Symbol	Ratio	Description	Symbol	Ratio	Description
$Re$	$\frac{\rho_c U_c H}{\mu_c}$	Reynolds number	$Pe_i$	$\frac{H U_c}{D_i}$	Péclet number
$F$	$\frac{\rho_c g}{\mu_c U_c / H^2}$	Bouyancy number	$Da$	$\frac{k c_{2,c}^a H}{M_2^a U_c}$	Damköhler number
$BN$	$\frac{\tau_{Y,c}}{\mu_c U_c / H}$	Bingham number	$\Psi_i$	$\frac{c_{1,c}}{c_{i,c}} \frac{M_i}{M_1}$	Concentration ratio

**Table C.1:** Summary of the non-dimensional numbers.

we set  $Pe_{2,3,4} = \infty$ , highlighting the behaviour of a single component diffusing in a reacting system with slight density gradients. Hence, here  $Pe = Pe_1 > 0$ .

Different scenarios of three-layer flow in the Hele-Shaw cell, including the unreactive flow ( $Da = 0$ ,  $Bi = 0$ ,  $Pe \sim \infty$ ), fully reacted flow ( $Da = 0$ ,  $Bi > 0$ ,  $Pe \sim \infty$ ), and reactive flow ( $Da > 0$ ,  $Bi > 0$ ,  $Pe > 0$ ), are examined in the current study. We approached these problems theoretically and numerically, using the aforementioned governing equations. A numerical solution of Eqs. (C.15)-(C.20) is used to study the multilayered flow in these three cases. A brief description of the numerical method is given in [92]. Besides, a 1-D theoretical approach is used to predict the fully developed and stable flow regimes in the slot, for the fully reacted and unreactive cases. Moreover, a simplified analytical model is used to solve the convective–diffusion equations, Eq. (C.15)–(C.17), for a uniform velocity field, in order to provide an estimation of the growth of gel layer. The details of analytical approach are discussed in the following section.



## C.2 Analytical modelling

### Analytical model for unreactive and fully reacted cases

A one-dimensional analytical approach is exploited to determine the stable and fully-developed flow in the channel, for the fully reacted and uncreative cases. Under the assumption of negligible molecular diffusivity ( $Pe \sim \infty$ ), these two problems can be considered as the flow of three generalized non-Newtonian incompressible and miscible fluids, labelled  $j = 1, 2, 3$ , in an inclined Hele-Shaw cell. The analytical model has been developed based on the assumption of one dimensional low Reynolds number flow,  $Re \ll 1$ , and a very large  $Pe$ -number ( $Pe = \infty$ ). For slow flow down a Hele-Shaw cell, the shear stress across the slot dominates the stress tensor. Hence, the dimensionless momentum equations corresponding to the fully developed steady flow of each fluid layer in the Hele-Shaw cell can be written as follows,

$$\begin{aligned}\frac{\partial \tau_{1,x,z}}{z} &= -f \\ \frac{\partial \tau_{2,x,z}}{z} &= -f - \chi_2 \\ \frac{\partial \tau_{3,x,z}}{z} &= -f - \chi_3\end{aligned}\tag{C.22}$$

where  $\tau_{j,x,z}$  is the shear stress across the slot and in the  $j$ -th fluid layer, and  $f = -\nabla p^*$ , that  $p^* = \frac{\rho_1 g \sin \theta x + p}{\mu_c U_c / H}$ . In Eq. (C.22),  $\chi_j = \frac{Re}{Fr_j^2} \sin \theta$  that represents the ratio of buoyancy stresses caused by the density difference between the layers to the viscous stresses. Here,  $Fr_j = U_c / \sqrt{At_j g H}$  that represents the ratio of inertia stress to the stresses caused by density difference, and  $\theta$  is the inclination angle of the channel. The Atwood number,  $At_j = \frac{\rho_j - \rho_1}{\rho_c} \geq 0$ , indicates the dimensionless density differences between the fluids. Note that the viscosity and density of the lightest fluid are used as the reference values for viscosity and density, i.e.  $\mu_c = \mu_1$ , and  $\rho_c = \rho_1$ . Considering the above equations, the stress field can be assumed to change linearly in each layer across the channel. Therefore, the shear stress on the lower and upper walls of the slot,  $\tau_{1,w}$ , and  $\tau_{2,w}$ , and on the lower and upper interfaces of

the middle fluid stream,  $\tau_{1,i}$ , and  $\tau_{2,i}$ , are linked by,

$$\tau_{1,i} = \tau_{1,w} - fh_1 \quad (\text{C.23})$$

$$\tau_{2,i} = \tau_{1,w} - f(h_1 + h_2) - \chi_2 h_2 \quad (\text{C.24})$$

$$\tau_{2,w} = \tau_{1,w} - f - \chi_2 h_2 - \chi_3 h_3 \quad (\text{C.25})$$

where  $h_j$  denotes the thickness of  $j$ -th stream in the fully developed flow, scaled by the thickness of channel. By considering a Herschel-Bulkley model for the rheology of the fluids, the velocity gradient in each layer can be written as follows,

$$\dot{\gamma}_{j,x,z} = \text{sgn}(\tau_{j,x,z}) \left( \frac{\|\tau\| - BN_j}{m_j} \right)^{1/n} \quad (\text{C.26})$$

that  $m_j = \frac{\mu_j(U_c/H)^{n_j-1}}{\mu_c}$  is the viscosity ratio for  $j$ -th fluid. It should be noted that the upper and lower fluid streams are assumed to be Newtonian, i.e.  $BN_1 = BN_3 = 0$ ,  $n_1 = n_3 = 1$ . By integration of velocity gradients away from the side walls of the slot toward the flow interfaces and from lower interface to the upper one, and considering the no-slip conditions on the walls, two velocities are obtained for each interface, in terms of wall shear stresses and interfacial stresses, that should be the same,

$$\int_{z=0}^{z=h_1} \dot{\gamma}_{1,x,z}(z, \tau_{1,w}, \tau_{1,i}) = \int_{z=h_2}^{z=h_1} \dot{\gamma}_{2,x,z}(z, \tau_{1,i}, \tau_{2,i}) \quad (\text{C.27})$$

$$\int_{z=h_1}^{z=h_2} \dot{\gamma}_{2,x,z}(z, \tau_{1,i}, \tau_{2,i}) = \int_{z=1}^{z=h_2} \dot{\gamma}_{3,x,z}(z, \tau_{2,w}, \tau_{2,i}) \quad (\text{C.28})$$

Similarly by integrating the constitutive laws of the fluids, an analytical expression is obtained for the velocity profile in each layer,

$$\begin{aligned} u_1(z) &= -\frac{1}{2f}(\tau_{1,x,z}^2 - \tau_{1,w}^2) \\ u_2(z) &= U_{1,i} - \frac{n}{n+1} \frac{1}{m_2^{1/n}(f + \chi_2)} ([|\tau_{2,x,z}| - BN]_+^{1+1/n} - [|\tau_{1,i}| - BN]_+^{1+1/n}) \\ u_3(z) &= -\frac{1}{2m_3(f + \chi_3)}(\tau_{3,x,z}^2 - \tau_{2,w}^2) \end{aligned} \quad (\text{C.29})$$

we now integrate  $u_j(z)$  across each layer to give the dimensionless average velocity in each layer, which is thus determined as a function of  $f, \chi_2, \chi_3$ , as well as the wall shear stresses and the interfacial stresses,

$$\begin{aligned}
U_{1,c} &= \frac{1}{2f^2} \left( \frac{\tau_{1,i}^3}{3} - \tau_{1,w}^2 \tau_{1,i} + \frac{2}{3} \tau_{1,w}^3 \right) \\
U_{2,c} &= -\frac{U_{1,i}}{f + \chi_2} (\tau_{2,i} - \tau_{1,i}) + \frac{n^2}{(n+1)(2n+1)} \frac{1}{m_2^{1/n} (f + \chi_2)^2} (\text{sgn}(\tau_{2,i}) [|\tau_{2,i}| - BN]_+^{2+1/n} \\
&\quad - \text{sgn}(\tau_{1,i}) [|\tau_{1,i}| - BN]_+^{2+1/n}) - \frac{n}{n+1} \frac{1}{m_2^{1/n} (f + \chi_2)^2} [|\tau_{1,i}| - BN]_+^{1+1/n} (\tau_{2,i} - \tau_{1,i}) \\
U_{3,c} &= \frac{1}{2m_3 (f + \chi_3)^2} \left( \frac{2}{3} \tau_{2,w}^3 + \tau_{2,w}^2 - \frac{\tau_{2,i}^3}{3} \right)
\end{aligned} \tag{C.30}$$

For given values of  $Re, Q_{1,3}/Q_2, \chi_j, m_j, BN_j$ , there are five variables,  $f, \tau_{1,w}, h_1, h_2, U_{1,i}$ , and five constraints including constant flow rates for each fluid stream, Eq. (C.30), and equality of interfacial velocities, Eqs. (C.27)-(C.28). We use Newton's iterative method to solve the aforementioned non-linear system of equations. On physical grounds, we expect the value of  $f$  for the stratified flow to lie between the corresponding values required to pump the same flow rate of either pure fluid. This allows us to prescribe upper and lower bounds for  $f$  for the iteration. Having determined the aforementioned unknown parameters, the values of interfacial shear stresses and wall shear stresses are calculated by using the Eqs. (C.23)-(C.25). Substituting these values in Eq. (C.29), the velocity profile corresponding to each fluid stream across the channel is obtained.

### Simplified model for reactive case

We use the convective-diffusion equations, (C.15)-(C.17), for steady-state transport of the chemical species, in a uniform velocity field,  $U_c$ . Considering the thin-slot approximation,  $\frac{\partial}{\partial x} \ll \frac{\partial}{\partial z}$ , and under the assumption that the diffusive transport of the reactive specie,  $c_1$ , along the flow direction,  $x$ -axis, is negligible,

Eqs. (C.15)–(C.17) are reduced to,

$$\frac{\partial c_1}{\partial x} - \frac{1}{Pe} \frac{\partial^2 c_1}{\partial z^2} = -Da c_1 c_2^a \quad (\text{C.31})$$

$$\frac{\partial c_2}{\partial x} = -a Da \Psi_2 c_1 c_2^a \quad (\text{C.32})$$

$$\frac{\partial c_3}{\partial x} = b Da \Psi_3 c_1 c_2^a \quad (\text{C.33})$$

To determine the thickness of the gel layer at any given  $Pe$ , and  $Da$ , we implement an iterative numerical scheme to solve Eqs. (C.31)–(C.33), subject to the boundary conditions, Eqs. (C.11)–(C.13). At each iteration, Eq. (C.31) is solved for  $c_1$  using the Thomas algorithm implicitly, and then  $c_2$  and  $c_3$  are obtained from numerical integration of Eq. (C.32), and Eq. (C.33), respectively.

### C.3 Methodology to determine the position of reacting front

The difference between the degree of fluctuations of tracing beads with respect to the macroscopic flow in the unreacted and reacted layers, provides the means for measuring the interface between these two layers. In this study, we use a method which is based on the image difference technique to quantify these fluctuations and predict the position of reacting front. According to this method, the reacted region is calculated by a modified correlation coefficient,  $R_d$ , as follows,

$$R_d(x, z) = 1 - \frac{1}{T} \int_0^{T-\Delta t} |I_b(x, z, t) - I_b(x + \Delta t U_c, z, t + \Delta t)| dt \quad (\text{C.34})$$

where  $\Delta t$  is 0.2 sec,  $T$  is at least 2 min, and  $I_b(x, y, t)$  are binary images of the intensity field. Particles that are in the gelated region move at the same velocity with limited translation out of the imaging plane from Brownian motion or diffusion leading to a correlation coefficient  $R_d(x, y) \rightarrow 1$ . A correlation cut-off of  $R_d = 0.8$  is used to isolate the interface between the unreacted and reacted components in the flow.